THE MORPHOLOGY AND KINETICS CONTROL OF CALCIUM PHOSPHATE MINERALIZATION USING TINY ENZYMES IDENTIFIED THROUGH DEEP-DIRECTED EVOLUTION

A Thesis Submitted to
the Graduate School of
İzmir Institute of Technology
in Partial Fulfillment of the Requirement for the Degree of

MASTER OF SCIENCE

in Bioengineering

by
Nursevim ÇELİK

July 2024
İZMİR

We approve the thesis of **Nursevim ÇELİK**

Examining Committee Members:

_____

Asst. Prof. Deniz Tanıl YÜCESOY

Department of Bioengineering, İzmir Institute of Technology

_____

Asst. Prof. Hümeyra TAŞKENT SEZGİN

Department of Bioengineering, İzmir Institute of Technology

_____

Asst. Prof. Genta AGANİ SABAH

Department of Oral and Dental Health, Izmir Tınaztepe University

08 July 2024

_____

Asst. Prof. Deniz Tanıl YÜCESOY

Supervisor, Department of Bioengineering
İzmir Institute of Technology

_____

Assoc. Prof. Ceyda ÖKSEL KARAKUŞ
Head of the Bioengineering Graduate Program
İzmir Institute of Technology

_____

Prof. Mehtap EANES
Dean of the Graduate School
İzmir Institute of Technology

ACKNOWLEDGMENTS

I would like to express my deepest gratitude to everyone who supported me throughout the whole process of this thesis. First of all, I would like to thank my advisor Asst. Prof. Deniz Tanıl YÜCESOY, whose expertise made a significant contribution to my master's degree experience.

I would like to extend my special thanks to my colleagues Yücesoy Research Group, whose friendship, support, and collaboration made this journey more enjoyable and enriching.

I am also grateful to my family for their unconditional support both financially and emotionally throughout my studies despite all the difficulties. I would like to thank my parents Emine and Yıldırım Çelik and my sisters Yasemin, Rukiye, and Halenur for believing in me and encouraging me to pursue my goals.

Finally, I must express my deepest gratitude to my friend Yasin Özmen for providing me with unwavering support and constant encouragement throughout all these processes. Without him, this achievement would not have been possible.

Thank you all.

ABSTRACT

THE MORPHOLOGY AND KINETICS CONTROL OF CALCIUM PHOSPHATE MINERALIZATION USING TINY ENZYMES IDENTIFIED THROUGH DEEP-DIRECTED EVOLUTION

Biomineralization is a critical natural process through which organisms produce minerals to harden or stiffen tissues, forming structures such as bones, shells, and teeth. Controlling biomineralization is vital for addressing medical and dental disorders, which significantly impact healthcare costs and quality of life. Effective management of biomineralization can prevent undesirable occurrences, such as vascular calcification, and promote beneficial processes, like bone and dental remineralization. While the chemical mechanisms inducing demineralization are well understood, the ability to rebuild a molecularly integrated mineral layer at a useful rate remains elusive. A fundamental aspect of this process involves the precise control of the morphology and kinetics of mineral formation, which can yield materials with specific properties and functions. This thesis aims to control the morphology and kinetics of calcium phosphate mineralization using tiny enzymes identified through deep-directed evolution. A peptide-phage library was utilized to select short-sequence peptides (12 amino acids) from a physiological environment, significantly impacting the mineralization kinetics and morphology of calcium phosphate minerals. Through iterative experimentation, the optimal conditions for variables such as pH, temperature, and molarity were adjusted, acknowledging their dynamic influence on the mineralization process. Structural characterization using SEM, XRD, and FTIR analyses confirmed the formation of hydroxyapatite in the presence of these peptides. Kinetic measurements revealed that these peptides catalyze calcium phosphate mineralization approximately an order of magnitude faster under physiological conditions. These peptides hold the potential for developing clinical products, such as dental gels, toothpaste formulations, and treatments for bone regeneration.

ÖZET

KALSİYUM FOSFAT MİNERALİZASYONUNUN MORFOLOJİSİ VE KİNETİĞİNİN DERİN YÖNLENDİRİLMİŞ EVRİM YOLUYLA GELİŞTİRİLMİŞ KÜÇÜK ENZİMLER ARACILIĞIYLA KONTROLÜ

Biyomineralizasyon çeşitli organizmalarda inorganik iyonların organik protein molekülleri ile birlikte koordineli bir şekilde çökelmesine ve büyümesine rehberlik eden temel biyolojik olgudur. İnsanlar başta olmak üzere omurgalılarda kemik ve diş omurgasızlarda yumuşakçaların kabukları gibi sert dokularının oluşumu biyomineralizasyonun bir parçasıdır. Biyomineralizasyonun etkili yönetimi, vasküler kalsifikasyon gibi istenmeyen oluşumları önlemek ve kemik ve diş remineralizasyonu gibi faydalı süreçleri teşvik etmektir. Biyomineralizasyonunda yer alan moleküler mekanizmaların ve düzenleyici yolların anlaşılması, tıbbi ve dental araştırmaların, terapötik müdahalelerin ve biyomimetik materyal tasarımının ilerletilmesi için gereklidir. Bu sürecin temeli, belirli özelliklere ve işlevlere sahip mineral malzemelerin oluşumunun morfolojisinin ve kinetiğinin hassas bir şekilde kontrol edilmesini içerir. Bu tez, derin yönlendirmeli evrim yoluyla tanımlanan küçük enzimler kullanarak kalsiyum fosfat mineralizasyonunun morfolojisini ve kinetiğini kontrol etmeyi amaçlamaktadır. Kalsiyum fosfat minerallerinin mineralizasyon kinetiğini ve morfolojisini önemli ölçüde yönlendirerek kontrol eden kısa dizili peptitleri (12 amino asit) fizyolojik bir ortamdan seçmek için bir peptit-faj kütüphanesi kullanılmıştır. Mineralizasyon süreci üzerindeki dinamik etkileri bilinen, pH, sıcaklık ve molarite gibi değişkenlerin mineralizasyon için en uygun koşulları yinelemeli deneylerle ayarlanmıştır. Bu peptitlerin varlığında hidroksiapatit kristallerinin oluşumu yapısal karakterizasyon için kullanılan SEM, XRD ve FTIR analizleri ile kanıtlanmıştır. Kinetik ölçümler, bu peptitlerin fizyolojik koşullar altında kalsiyum fosfat mineralizasyonunu yaklaşık bir kat daha hızlı katalize ettiği kinetik ölçümler ile ortaya koymuştur. Mineral kristalleri üzerinde etkisi doğrulanan bu peptitler diş jelleri, diş macunu formülasyonları ve kemik rejenerasyonu tedavileri gibi klinik ürünlerin geliştirilmesi için potansiyel taşımaktadır.

TABLE OF CONTENTS

LIST OF FIGURES

Figure **Page**

Figure **Page**

LIST OF TABLES

Table **Page**

ABBREVIATIONS

CPP-ACP	Casein Phosphor Peptide-Amorphous Calcium Phosphate
HAp	Hydroxyapatite
DSPP	Dentin Sialophosphoprotein
BSP	Bone Sialoprotein
CNT	Classical Nucleation Theory
CPA	Crystallization by Particle Attachment
SBF	Simulated Body Fluid
OCP	Octalcium Phosphate
MCPM	Monocalcium Phosphate Monohydrate
TCP	Tricalcium Phosphate
β-TCP	β-Tricalcium Phosphate
α-TCP	α-Tricalcium Phosphate
DCP	Dicalcium Phosphate
BP	Biopanning
TBS	Ph.D.-12 Phage Display Peptide Library stock solution
XRD	X-ray Diffraction
FTIR	Fourier Transform Infrared Spectroscopy
SEM	Scanning Electron Microscope

CHAPTER 1

INTRODUCTION

1.1 Dentin Diseases and Etiology of Dental Diseases

Dental disease is the most common disease globally, affecting all segments of society. According to the World Health Organization, almost 3.5 billion people worldwide have oral disease. 3 out of 4 people have a dental disease. Also, 2 billion people and 621 million children worldwide have dental cavities. Dentin is the mineralized tissue component that makes up the majority of the tooth structure. it is the crucial mineralized tissue that provides structural support and integrity to maintain the integrity and strength of the tooth(Kassebaum et al, 2015). Various dentinal diseases can be caused by different etiologic factors such as genetic predisposition, trauma, inadequate oral hygiene, and microbial infections, or an intersection of such factors (Mathur, and Dhillon, 2018). Understanding the etiology of these dental diseases is essential for effective prevention, diagnosis, and management strategies for these conditions. The etiology of dental disease involves a multifactorial interaction of poor oral hygiene practices, dietary habits, genetic predisposition, systemic conditions, and environmental influences(Kim et al, 2006; Wright, 2006). Bacterial infections, caused by Streptococcus mutans and Lactobacillus species, are major contributing factors in the development of dental caries and periodontal disease. These pathogens use dietary sugars to produce acids that demineralize enamel and dentin, leading to cavity formation and gingivitis (Kim et al, 2006; Mira, Simon-Soro, and Curtis, 2017). A comprehensive understanding of the etiology and impact of dentin diseases, which pose various challenges in dental pathology, is imperative. By elucidating the factors that cause these conditions to occur and discovering and developing appropriate preventive and therapeutic strategies, researchers can effectively manage and reduce the impact of dentin diseases on patient oral health (Cummins, 2013; Kassebaum et al, 2015).

1.1.1 Dental Tissues

Dental tissues are specific types of hard and soft tissues composed of highly specialized structures that play critical roles in oral health and function (Goldberg et al, 2011). There are four main dental tissues: enamel, dentin, cementum, and pulp. The outermost layer, enamel, is the hardest and most mineralized tissue in the human body. Enamel is composed of minerals, mainly hydroxyapatite crystals. It covers the outer surface and crown of the tooth. It protects the tooth tissue by forming the first line of defense against wear and decay caused by mechanical forces and chemical erosion (Kinney, Marshall, and Marshall, 2003). Beneath the enamel is dentin, a less mineralized but more flexible tissue composed of microscopic tubules that transmit sensory signals to the pulp. Underneath the enamel is dentin, a tissue that makes up the majority of the tooth's structure. it contains microscopic tubules that transmit sensory signals to the pulp. less mineralized but more flexible, dentin tissue is not as hard as enamel but is still quite durable. The pulp is the soft tissue in the center of the tooth, below the dentin. the pulp is vital for the vitality of the tooth. It is made up of nerves, blood vessels, and connective tissue (Gronthos et al, 2000). The cementum is a hard tissue that covers the tooth root and connects it to the surrounding alveolar bone (jawbone) through the periodontal ligament. This tissue is less mineralized and less hard than enamel and dentin but plays a crucial role in maintaining tooth stability. These tissues work together to provide structure, support, and protection to the teeth and are essential for proper (Kinney, Marshall, and Marshall, 2003; Bosshardt, 2005).

1.1.2 Dental Demineralization: The Loss of Natural Minerals from the Tooth

Dental demineralization is the process of loss of essential minerals in teeth that triggers dental caries and other oral pathologies. Demineralization begins with the dissolution of hydroxyapatite crystals, which are sensitive to acidic dissolution, that make up tooth enamel and dentin (Featherstone, 2008). Demineralization occurs when the

intraoral pH drops below the critical values of pH 5.5 for enamel and pH 6.5 for dentin (Featherstone, 2008). With the onset of the demineralization mechanism, these dental tissues weaken and caries and other damages begin to occur (Chaffee, Feldens, and Vítolo, 2014). Etiological factors causing demineralization: Acidic environment, poor oral hygiene, reduced salivary flow, high carbohydrate diet, and orthodontic treatments. Frequent consumption of acidic foods and beverages causes a decrease in the pH of the oral environment. Thus, demineralization has been shown to occur significantly (Larsen, and Nyvad, 1999). Poor oral hygiene leads to insufficient removal of bacterial plaque in the oral environment. These bacteria metabolize dietary sugars to produce acid, leading to the accumulation of bacterial biofilms (García-Godoy, and Hicks, 2008). Saliva buffers acids and provides calcium and phosphate ions to maintain a healthy oral environment and acts as a protector against demineralization (Söderling, 2009; Slots, and Slots, 2011; Kleinberg, 2002). The use of orthodontic appliances interferes with oral hygiene practices, leading to increased plaque retention and subsequent enamel demineralization (Fleming et al, 2009). Signs and symptoms of dental demineralization are as follows: white spots on the teeth show the early stages of enamel erosion (Featherstone, 2008). Symptoms of tooth aching and pain in response to hot, cold, or sugary foods and drinks, and increased tooth sensitivity in these conditions (Kim et al, 2006). The appearance of visible pits or holes indicates advanced tooth decay. If there is yellowing or darkening of tooth color, these signs and symptoms indicate dental demineralization of tooth tissue (Wright, 2006; Paris, and Meyer-Lueckel, 2009).

1.2 Treatment Approaches and Issues

1.2.1 Clinical Treatments

Dental diseases are tried to be prevented with various treatment methods in clinics. The most common of these treatment elements are as follows: Fluoride therapy can help rebuild the weakened structure of enamel tissue with in-office fluoride applications and prescription fluoride toothpaste. This treatment modality is often used to create a temporary barrier against demineralization. However, it is only used in the absence of

cavitation (Gao et al, 2016). Another treatment method is techniques such as resin infiltration. These resins include binders and repair resin composites. The composites form a hybrid layer that effectively seals white spots and early caries lesions without the need for drilling or filling. This treatment method aims to prevent white spots and early caries (Doméjean et al, 2015). The last treatment is the laser. They provide treatment by coagulation of the proteins of the fluid in the dentinal tubules and partial melting and occlusion of the tubules. It also depresses the nerves inside the tubules and prevents their conduction function (Asnaashari, and Moeini, 2013). However, these treatments are short-lived and require repetition.

1.2.2 Commercial Products

Some dental products used in daily life also have principles of approach to the treatment of these diseases. The first example of these approaches is Potassium Nitrate. Potassium nitrate-based products are agents that disrupt the transmission of nerve impulses. Toothpaste containing potassium nitrate is used for desensitization (Benson et al, 2013). The second example of these approaches is bioglass. The main component of bioglass is silica, which acts as a nucleus for the precipitation of calcium and phosphate. Bioglass causes the formation of an apathy layer that leads to blockage of the dentinal tubules (Vollenweider et al, 2007). The use of products based on oxalates is a move towards the treatment of dental diseases. Oxalates can clog dentinal tubules and reduce the permeability of dentin. Findings have shown that the reduction in dentine hypersensitivity with oxalate remains for a short period of time. Potassium oxalate should not be used for long periods of time as it may cause some digestive disorders. Kinds of toothpaste-containing agents such as casein phosphor peptide-amorphous calcium phosphate (CPP-ACP) have been shown to promote remineralization of initial caries lesions in vitro studies. However, only partial remineralization has been clinically proven (Reynolds, 1998). All of these studies are temporary solutions. In these types of treatments, the tubules are not completely closed permanent treatments are not provided or the nerves are numbed and the pain is silenced with these types of treatments, they are not treated completely.

1.2.3 Biomimetic Study: Protein-Guided Remineralization and Their Limitation

Due to the inadequacy of dental products and clinical treatments we use in daily life, the protein-guided remineralization approach has been a promising approach in the field of biomimetic mineralization. Repair and regeneration of damaged tooth enamel tissue with the aim of restoring its structural integrity and function has been achieved by a protein-guided remineralization approach. The basic principle of this approach is the use of bioactive proteins to regulate the nucleation and growth of mineral crystals on damaged tooth surfaces. This biomineralization approach involves the use of dental tissue-specific proteins to control the highly organized formation of dental mineral structures in living organisms (Cochrane et al, 2010; Bertassoni et al, 2011). The amelogenin protein in enamel, which provides templates for mineral nucleation, influences the size, orientation, and organization of mineral crystals. Phosphoproteins, like casein phosphopeptides, bind to calcium ions and can prevent them from precipitating and thus promote their incorporation into mineral crystals, thus promoting the growth of mineral crystals (Bertassoni et al, 2011). The local concentrations of calcium and phosphate ions are regulated by proteins to create a suitable environment for mineral deposition. The surface properties of damaged tissues are altered by proteins to create an interface that enhances mineral adhesion and promotes remineralization (Young, Neel, and Chrzanowski, 2014; Deshpande et al, 2010).

Protein-guided remineralization can lead to the formation of irregular or amorphous mineral precipitates during the nucleation of mineral crystals. This can limit the mechanical strength and aesthetic quality of the repaired tooth tissue (Gower, 2008). When a protein-driven remineralization approach is used instead of traditional remineralization methods, the kinetics of remineralization are slower and the restoration of tissue functionality is delayed. Some proteins that nucleate mineral crystals on damaged tooth surfaces may have cytotoxic effects and pose a risk to surrounding tissues and cells in the remineralization process. The stability and long-term durability of mineral deposits nucleated by protein-driven remineralization pose a problem. There is concern that these mineral crystals may be susceptible to degradation or dissolution over time(Bertassoni et al, 2009; Walsh, 2009).

However, more research is needed to resolve the limitations of protein-driven remineralization and to increase its clinical applicability. In this context, the use of peptides directed from amelogenin protein, a protein specific for dental tissues, has been proposed to direct remineralization (Dogan et al, 2018). The main advantage of using short peptides is that they can easily escape components of the immune system. With peptide-driven remineralization, the formation of HAp mineral precipitates, a more regular and tooth tissue mineral phase, was observed during the nucleation of mineral crystals. Therefore, the problem of limiting the mechanical strength and aesthetic quality of the repaired tooth tissue was solved (Cao et al, 2015).

1.3 Biomineralization

Biomineralization is a fundamental biological phenomenon that guides the coordinated precipitation and growth of inorganic ions together with organic protein molecules in various organisms (Mann, 2001; Sharma et al, 2019). It is hypothesized that this process is driven by protein molecules and determines the hierarchical structure of the formed tissue (Mann, 2001; Weiner, and Lowenstam, 1986). The unique properties of hard mineral tissues produced by the biomineralization process in living organisms such as durability, hardness, and flexibility are regulated by this process. The formation of hard tissues such as bones and teeth (calcium phosphate) in vertebrates, especially humans, and shells (calcium carbonate) in invertebrate mollusks is a part of biomineralization. Hard tissue biomineralization (the process of bone and tooth mineralization) is the process of producing bioceramic materials with exceptional material properties composed of organic-inorganic composites (Li et al, 2004; Studart, Erb, and Libanori, 2015). The existing literature is full of studies on the application of nanotechnology in hard tissue research and dentistry to mimic the in vitro synthesis of such materials (Smith et al, 2018; Melo et al, 2013; Khurshid et al, 2015).

When a tooth is examined anatomically, the visible part consists of two parts, the crown and the root covered by the periodontium (McKee, Addison, and Kaartinen, 2006). The enamel, the outermost layer of the tooth, contains little or no protein. About 95% by weight of enamel is composed of tightly packed crystals of hydroxyapatite

($Ca_{10}(PO_4)_6(OH)_2$), an inorganic material, and <1% by weight of organic matrix (Bartlett, and Simmer, 1999; Simmer, and Fincham, 1995). Enamel tissue is formed by the secretion of enamel matrix proteins by ameloblasts. The key proteins amelogenin, ameloblastin, and enamelin regulate the nucleation and growth of hydroxyapatite crystals in enamel. After initial matrix formation by ameloblasts, ameloblasts increase mineral density by facilitating the removal of organic compounds and water (Beniash, Simmer, and Margolis, 2012). Immediately below the enamel is the dentin tissue, which forms the main component of teeth. Approximately 70% of the weight of dentin tissue is composed of hydroxyapatite crystals, which are inorganic material, 20% is composed of organic matrix, which is primarily type I collagen, and the remaining 10% is composed of water (Chen et al, 2003). Odontoblasts, specialized cells, form the dentin matrix or pre-dentin and thus synthesize mineralization in the biological process (Goldberg et al, 2006). In this phenomenon, dentin sialophosphoprotein (DSPP) and other non-collagenous proteins are important parameters without promoting hydroxyapatite deposition (George, and Veis, 2008). Cementum, another tissue of the tooth, is located just below the dentin tissue. The pulp, which is important for tooth function, is located in the innermost part of the tooth tissue. It is a connective tissue that contains nerves, blood vessels, and highly specialized cells for dental tissue (Sloan, 2015). In this tissue, bone sialoprotein (BSP) and cementum attachment protein (CAP) promote hydroxyapatite deposition, involving a similar but different mechanism facilitated by cement oblasts (George, and Veis, 2008).

The formation of specialized hard tissues containing calcium crystals such as hydroxyapatite, which occurs in the context of tooth formation, is called dentin biomineralization. Tooth biomineralization is a dynamic process that is essential for dental health, tooth development, and repair. A better understanding of Tooth biomineralization at the molecular level and new insights into the hierarchical mechanism have been provided by advances in molecular biology and materials science (Smith, 2003; MacDougall, and Javed, 2010). Regulated by a network of cells and proteins, the Tooth biomineralization process involves a series of complex steps (Cobourne, and Sharpe, 2014). Extracellular matrix vesicles derived from odontoblast cells serve dentin formation as nucleation sites for hydroxyapatite crystals (MacDougall, and Javed, 2010). Tooth biomineralization is also accomplished through this dentin formation pathway by a tightly regulated series of events (Smith, 2003). Advancing dental research, treatment strategies

and biomimetic material development is possible by understanding the complex process of dentin biomineralization.

1.4 Nucleation Theories of Mineralization

The process by which minerals are formed from ions in solution is called the mineralization process (Wu, 1996). These mineralization processes play an important role in a wide range of natural phenomena, from the formation of geological formations to the growth of biological structures such as shells and bones in living organisms (Oxtoby, 1998). The process of mineralization is a complex process involving a mechanism that is influenced combinatorial by many parameters such as temperature, pressure, chemical composition, and biological activity (Anisimov, 2003). The basis of mineralization is the nucleation process, the first step in which atoms or molecules become a stable nucleus (crystal). Three dominant theories of nucleation explain the mechanisms of this nucleation process. Studying the thermodynamics, kinetics, and molecular dynamics related to nucleation, the first step in the process of mineralization, and elucidating the underlying mechanisms of this process is essential for further advancement in both natural and synthetic systems (Vehkamäki, 2006).

1.4.1 Classical Nucleation Theory

Classical nucleation theory (CNT), the most well-established nucleation model proposed in the 1930s, clarifies how higher-order nucleation occurs in supersaturated solutions (De Yoreo et al, 2015). It provides a framework for how this stable nucleation is controlled by kinetic and thermo-dynamic parameters (De Yoreo et al, 2015; Wallace et al, 2013; Kalikmanov, 2013). Classical nucleation theory (CNT) suggests that nucleation is a stochastic process controlled by the interaction of thermodynamic variables such as temperature and interfacial tension between the nucleus and the surrounding medium under supersaturation conditions (Bostanov, Mladenova, and

Kashchiev, 2000). This stochastic process involves random thermal fluctuations forming small clusters of solutes in a supersaturated solution. Suppose these crystalline clusters are smaller than the critical radius and hence of insufficient size. In that case, they may redissolve in solution or, if they have a critical radius, they may grow to form a stable nucleus depending on their size (Oxtoby, 1998). In classical nucleation theory, the main parameters affecting the nucleation mechanism are the concepts of supersaturation, critical radius, and energy barrier. If a solution has a solute concentration higher than the solubility limit at a given temperature and pressure, it is a supersaturated solution and an ideal environment for classical nucleation theory. The nucleus cluster formed in this type of solution environment tends to dissolve clusters smaller than the critical radius, while larger ones tend to grow. The critical radius of these nucleus clusters determines the size at which they can reduce their free energy by growing instead of dissolving (Kashchiev, 2000).

In the mathematical framework of CNT, the Gibbs free energy concept, where the change in free energy (ΔG) is given, is the thermodynamic variable necessary for the formation of a nucleus. The activation energy for nucleation can be calculated as follows according to classical nucleation theory;

$$\Delta G = -\frac{4}{3}\pi r^3 \rho \Delta\mu + 4\pi r^2 \gamma \qquad (1.1)$$

Where r is the radius of the nucleus, ρ is the density of the core material, $\Delta\mu$ is the chemical potential difference and γ is the surface tension (Oxtoby, 1998).

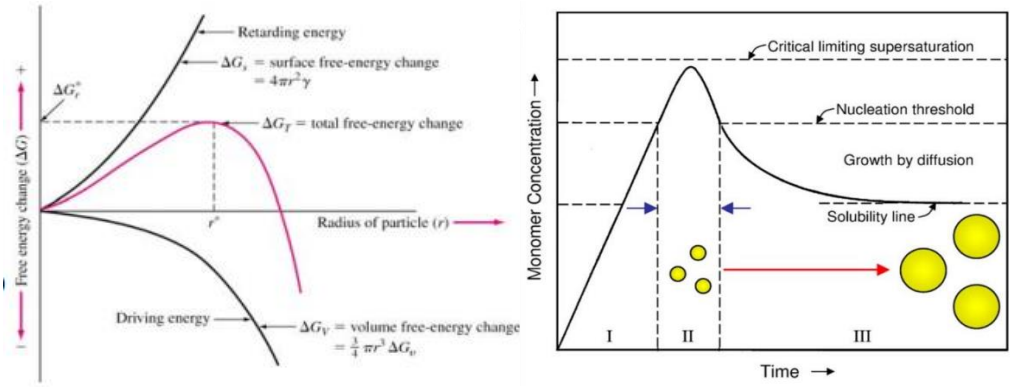

Figure 1.1. Free energy plot versus radius of nuclei in CNT. (Source: Flatken, 2022)

As seen in Figure 1.1., the bulk energy of a newly formed nucleus (ΔGv) drives nucleation, but the formation of a phase interface and hence interfacial tension (γ) hinders nucleus growth. It is clear from this indication that the free energy (which has a negative value) decreases with the third power of the radius. Figure 1.1 shows the growth curve of nuclei crystals when the sum of bulk energy and surface energy is greater than the critical size (rc). Due to the formation of a phase interface, the mass energy starts to offset the energy costs. The activation energy at the critical radius (rc) can be expressed as:

$$\Delta G^* = \frac{16\pi\gamma^3}{3(\Delta G\gamma)^2} = \frac{16\pi\gamma^3\,\vartheta^2}{3(kT\ln S)^2} \qquad (1.2)$$

By decreasing the interfacial tension (γ) and/or increasing the saturation (S) in solution, the activation energy can be reduced, which helps the clusters reach a critical size to form stable nuclei.

It is the most common theorem used to explain CNT homogeneous nucleation in organic and inorganic systems. The fact that this theorem assumes isotropic and homogeneous nucleation conditions limits its applicability to heterogeneous nucleation and complex biological environments. In biomineralization processes, this theorem is tightly regulated through protein molecules. In this process, protein molecules help in the

formation of appropriately structured initial nucleating ion clusters and lower the energy barrier (Sharma et al, 2021).

1.4.2 Non-Classical Theory

Challenging some of the implications of Classical Nucleation Theory (CNT), recent studies have developed non-classical nucleation theory (Gebauer, Völkel, and Cölfen, 2008; Rao et al, 2014). This non-classical nucleation theory generally emphasized the formation of pre-nucleation clusters early in nucleation and suggested that these precursor clusters assimilate to form amorphous mineral phases at later stages (Gebauer, Völkel, and Cölfen, 2008; Rao et al, 2014; Gebauer et al, 2010; Kellermeier, Cölfen, and Gebauer, 2013). Recent studies have developed new nucleation theories of non-classical nucleation theories. These theories include two-stage nucleation, cluster-based models, and Ostwald's rule of stages (Gebauer et al, 2010).

The two-stage theory of nucleation suggests that nucleation occurs through an intermediate metastable phase, in contrast to the direct phenomenon of forming a crystal nucleus in the classical theory of nucleation (Vekilov, 2010). In the first stage of the formation process of nucleation, a dense liquid or amorphous precursor phase is formed, followed by the transformation of this precursor phase into a crystalline nucleus in the second stage (Rao et al, 2014; Gebauer et al, 2010). In systems where the crystallization phase of ions is inhibited by kinetic or energetic barriers, it is argued that the mechanistic functioning of this theory takes place (Gebauer et al, 2010; Kellermeier, Cölfen, and Gebauer, 2013). This theory is particularly relevant in the processes of controlled mineralization and the formation of complex minerals in biological organisms. It is inferred that organic matrices mediate the formation of amorphous precursors in the biomineralization process. As a result of the studies, it was understood that the phases leading to nucleation are highly sensitive to pH in addition to protein molecules (Gebauer, Völkel, and Cölfen, 2008).

Cluster-based models argue that mineral nucleation begins with the formation of stable, pre-nucleation clusters that are structurally distinct from both the solute and the

final crystalline phase. These clusters can become more integrated over time, leading to nucleation and growth (Cölfen, and Mann, 2003).

Ostwald's Rule of Stages suggests that the emerging phase in a supersaturated solution is not necessarily the most stable phase, but proceeds to this stable phase through a series of metastable intermediate phases, each with the lowest free energy barrier (Navrotsky, 2003; Söhnel, and Mullin, 1988). According to Ostwald's Rule of Stages, in the process of successive transformations of different polymorphs of minerals, the least stable but kinetically preferred phase is formed as the precursor phase, which then evolves to the more stable phase through the transformation process (Söhnel, and Mullin, 1988). Mineralization processes have been rationalized by understanding the sequential nature of kinetic factors and phase transformations.

1.4.3 Crystallization by Particle Attachment

The third hypothesis of the nucleation theory, Crystallization by Particle Attachment (CPA), is a crucial mechanism for the mineralization process and has challenged conventional views on the phenomenon of crystal growth. In the conceptual approach, crystallization by particle attachment (CPA) emerges as a combination of classical and non-classical theories (Sharma et al. 2021). In the traditional crystallization process, the theories of crystal formation and growth from ions, atoms, or molecules in a supersaturated solution or vapor environment were primarily conceptualized (De Yoreo et al, 2015). However, what distinguishes and differentiates the particle bonding crystallization (CPA) theory from traditional approaches is that classical and non-classical theories cannot fully explain the various morphologies and sizes of natural and synthetic crystals formed as a result of the mineralization process (De Yoreo et al, 2015; Andreassen, and Lewis, 2017; Wang et al, 2019). A new perspective, the CPA hypothesis of crystallization by particle binding, is advocated as an alternative mechanism by which mineral particles (from clusters to nanoparticles) rearrange to form crystal structures by integrating and growing (De Yoreo et al, 2015). In the CPA hypothesis of crystallization by particle binding, interactions with ion clusters, gels, oligomers, and liquid phases form amorphous or crystalline mineral phases and ultimately promote the formation of larger

crystal structures (Wallace et al, 2013). In addition to the multiple pathways to the resulting structured crystals, energy kinetics, phase stabilities and the presence of additives such as gels, polymers, and small molecules are several factors that influence the organization of the crystal structure (De Yoreo et al, 2015). The researchers observed the crystal growth process in real-time using advanced imaging and spectroscopic techniques, thus experimentally validating the CPA hypothesis (Mirabello et al, 2019). Visualization of quartz growth in geochemical processes and observation of the formation of biomineral structures in marine organisms are important studies (Li et al, 2012). While the CPA hypothesis has proven strengths, it also has several challenges. The main ones are the precise control of particle properties and the scaling up of the hypothesized process for industrial applications (De Yoreo et al, 2015).

1.5 Biomimetic Synthesis of Calcium Phosphate (Ca/P) Minerals

Biomimetics of calcium phosphate (Ca/P) minerals for biomedical applications can be performed at different levels depending on the morphology, composition, structure, bulk, and surface chemical-physical properties of the synthetic mineral material. The interaction of synthetically produced mineral materials with living tissue should be optimized (Roveri, and Iafisco, 2010). This optimization is achieved by synthetic mineral biomaterials mimicking all the properties of biological tissues and biogenic materials in terms of functionality (Enax, and Epple, 2018). The high degree of complexity, miniaturization, hierarchical organization, hybridization, reliability, efficiency, resistance and adaptability characteristics of biogenic materials are quite astonishing for researchers working in this field (Roveri, and Iafisco, 2010). The inability of biomimetic materials to mimic 100% original natural biogenic materials in terms of their characteristics may cause limitations (Eliaz, and Metoki, 2017). Biomimetic studies are very important for the design and synthesis of innovative and progressive materials and structures (Meyer et al, 2018).

Specific strategies for the long-term chemical construction of well-engineered architectures from pre-formed nano- or microcrystalline inorganic-organic building blocks in biomineralization are related to the morphology of the biogenic material (Eliaz,

and Metoki, 2017). The nanometer-scale conformational variability of biological complex compact structures triggers biological macromolecules to promote the formation of specific junctions (Layrolle et al, 2001). Hydroxyapatite (HA), $Ca_{10}(PO_4)_6(OH)_2$, the major inorganic compound of mammalian bone and dental tissues, is one of the most stable forms of calcium phosphates. A better understanding of the crystallization mechanism of hydroxyapatite (HA) in its natural mineralization synthesis process and its applicability as an industrial material is being deeply investigated in numerous interdisciplinary fields.In synthetic HA crystals, morphology, biocompatibility, bioactivity, absorbability, osteoconductivity, and surface functionalization represent the physical and chemical properties required to optimize applicability as industrial materials (Limeback, Enax, and Meyer, 2021).

Specifically, biomineralization for dental applications aims to develop durable, functional, bioactive, and biocompatible dental restoration materials that closely mimic the natural properties of the hierarchical and complex structure of the tooth mineral (Meyer et al, 2018). Biomineralization for dental applications is a technology that could potentially revolutionize restorative dentistry. Moreover, these technologies not only replace damaged dental tissues but also actively contribute to the healing and regeneration of dental tissues (Enax, and Epple, 2018).

Enamel is the most robust mineralized tissue formed by vertebrates and is the most highly mineralized skeletal tissue found in the mammalian body (Robinson, Kirkham, and Shore, 2017). Approximately 95% by weight of enamel tissue is composed of tightly packed hydroxyapatite crystals, which are inorganic material, and <1% by weight contains organic matrices (Bartlett, and Simmer, 1999; Simmer, and Fincham, 1995). The high mineralization content of enamel tissue makes it a very impressive model for understanding both the basic mineralization processes in enamel tissue and the processes occurring in the extracellular matrix. The parameters that distinguish enamel from the mineral structure of bone tissue are the architecture, pathology, and biological mechanisms mediating the formation of enamel mineral tissue. In addition, mature enamel is essentially cell-free and does not self-renew or remodel. This structure is the main feature that distinguishes enamel from other biomineralized tissues such as bone and dentin. Mineralization of enamel tissue is a highly regulated process involving precise genetic control and protein-protein interactions, protein-mineral interactions, and cell membrane interactions (Tamerler, and Sarikaya, 2008). Dentin is the tissue located just below the enamel and forms the main component of the teeth. It absorbs stresses from

physical activities such as chewing and prevents the enamel tissue from breaking. The composition of dentin is similar to bone in terms of the structure of the mineral tissue. Cementum, another tissue of the tooth, is a tissue that surrounds the tooth root. However, it is the mineralized layer that covers the dentin layer and part of the enamel layer. Through the cementum, teeth are attached to the alveolar bone (jawbone) via the periodontal ligament (PDL). The pulp, another structure of the tooth, contains nerves, blood vessels, fibroblasts, and lymphocytes.

1.5.1 Synthesis Methods of Biomimetic Hydroxyapatite Nanocrystals

The synthesis of biomimetic hydroxyapatite nanocrystals from Ca/P minerals involves complex interactions between chemical, biological, and physical factors. Biomaterial synthetic hydroxyapatites synthesized from Ca/P minerals by mimicking natural biomineralization processes exhibit good properties such as direct binding to tissue, biocompatibility, bioactivity, osteoconductivity, etc., which is exciting for applications in restorative dental treatment fields (Dorozhkin, 2010). Biomimetic approaches have been proposed to prepare nanoscale or nanocrystalline structures through many different methodologies (Schmidt, 2000; Mao et al, 2007). Some of these methods include hydrothermal synthesis (Guo et al, 2007; Mao et al, 2007), mechanochemical synthesis (Yeong, Wang, and Ng, 2001), wet chemical precipitation (Wang, and Shaw, 2007; Zhang, and Lu, 2007), sol-gel synthesis (Sun et al, 2007), microwave processing (Liu et al, 2004), vapor diffusion (Iafisco et al, 2010), co-precipitation (Chai, and Ben-Nissan, 1999), silica gel template (Iafisco et al, 2009), emulsion-based synthesis (Phillips et al, 2003), and several other methods by which nanocrystals of various shapes and sizes can be obtained (Layrolle, and Lebugle, 1996).

Biological fluids become supersaturated concerning calcium phosphate salts, resulting in their deposition on surfaces in contact with hard tissues. The supersaturated simulated body fluid (SBF) method, which mimics this physiological process, is one of the most widely used methods for the biomimetic synthesis of dental tissues (Oyane et al, 2003).

I. Preparation of Simulated Body Fluid: Depending on the purpose, an aqueous solution that mimics the ionic composition of human saliva or plasma is a simulated body fluid. In vitro studies of the synthesis of biomimetic hydroxyapatite nanocrystals from Ca/P minerals can be performed in simulated body fluid (SBF) with ion concentration levels close to the chemical composition of human blood plasma or saliva (Kokubo et al. 1990).Saliva-like environments are the target point for dental applications. Ca/P minerals solutions contain calcium, phosphate, sodium, potassium, magnesium, chloride, and bicarbonate ions as standard (Spanos et al, 2006).

II. Supersaturation: The simulated body fluid is prepared by supersaturating it with calcium and phosphate ions. Supersaturation in terms of the ionic concentration of the solution is very important as it allows precipitation of Ca/P minerals (Nancollas, 1984).

III. Surface Immersion*:* The researchers noticed the problem of slow formation kinetics of Ca/P minerals precipitates. To overcome this problem, they used alternative liquid compositions defined as revised SBF (Dorozhkin, Dorozhkina, and Epple 2003). The inorganics tested in these alternative SBF compositions included various types of glass ((Bigi et al, 2000), SiO2, TiO2, ZrO2, Ta2O5, Nb2O5) gels (Kokubo et al, 2001), and NaOH-treated Ti (Fujibayashi et al, 2001), and Ta (Miyazaki et al, 2001), silylated HAP (Santos et al, 2001)) and organic (poly(L-lactic acid), arachidic acid monolayers with carboxyl groups (Sato et al, 2001), and polyethylene terephthalate (Kim et al, 2000) substrate groups. Besides these, various organic structures such as biodegradable polymers and even collagen matrices can be used. This mineralization kinetically accelerating substrates are immersed in SBF.

In addition, nucleating agents can be added to the SBF solution medium to control the morphology and size of Ca/P crystals more precisely. Biological molecules such as collagen and amelogenin can be used as nucleating agents. Amelogenin protein specifically regulates the growth of hydroxyapatite crystals during tooth development and plays a natural role in the formation of enamel tissue (Rapaport et a 2000). Artificial nucleating agent templates are synthetic polymers or nanomaterials. These artificial polymers and nanomaterials can act as templates to induce and direct mineralization in

desired patterns and directions (Rapaport et al, 2000). Scaffold integration agents are usually integrated directly into the scaffolds or coated onto them. These agents are then treated with mineralizing solutions. This method is ideal for achieving a more uniform and oriented crystal growth (Francis Suh, and Matthew, 2000).

The conditions under which biomimetic mineralization occurs are crucial for the morphology and formation kinetics of Ca/P minerals crystals. The pH of the mineralization solution is maintained at a neutral or slightly basic level (about 7.4), which is optimal for hydroxyapatite formation. It is possible to mimic the dynamic changes in a biological environment by pH fluctuations occurring in the solution. The pH control in SBF solution can be adjusted, maintained, and changed in the liquid phase by equilibration using a suitable buffer (Tas, 2000). Specific buffer matrices at different pH values are commercially available to researchers (McPherson, and Cudney, 2014).Considering the pH values of the intraoral environment, the most appropriate buffers can be selected. Mimicking body conditions is necessary to influence the rate of mineral deposition and crystal morphology. Here the solution is kept and maintained at physiological body temperature (37°C). Temperature is another parameter that facilitates the kinetics of precipitate formation. Mimicking body conditions is an important step in influencing the rate of mineral deposition and crystal morphology (Tas, 2000).

1.6 Effect of Ca/P Manipulation on The Formation of Mineral Phases (Component Phases of Calcium Phosphate Minerals)

In liquid calcium phosphate solutions, all minerals formed in the $Ca(OH)_2$-H_3PO_4-H_2O system can be precipitated at appropriate pH and temperature. Very few are stable under physiologically favorable conditions. The solubility of Calcium Phosphate minerals determines the stability of these components. The content of Calcium Phosphate minerals with variable stability in order of decreasing solubility is quite complex: Dicalcium Phosphate ($CaHPO_4$, DCP), Octacalcium Phosphate ($Ca_8H_2(PO_4)_6.5H_2O$, OCP), Tricalcium Phosphate (β-$Ca_3(PO_4)_2$, β-TCP) and Hydroxyapatite ($Ca_5(PO_4)_3OH$, HAP).

Table 1.1. Chemical composition, Ca/P molar ratio, solubility, pH, and temperature stability range of common calcium phosphate phases in aqueous solutions

Name	Abbreviation	Chemical composition	Ca:P ratio	Solubility -log (K_s)[a]	pH and temperature (°C) stability
Monocalcium phosphate Monohydrate	MCPM	$Ca(H_2PO_4)_{2.H2O}$	0,5	1,14	0.1–2.0 25°C
Dicalcium phosphate	DCP, DCPA	$CaHPO_4$	1	6,90	2.0–5.5 > 80°C
Octacalcium Phosphate	OCP	$Ca_8H_2(PO_4)_6.5H_2O$	1,33	96,60	5.5–7.0 25°–37°C
β-Tricalcium Phosphate	β-TCP	β-$Ca_3(PO_4)_2$	1,50	28,90	b
α-Tricalcium Phosphate	α-TCP	α-$Ca_3(PO_4)_2$	1,5	25,50	b
Hydroxyapatite	HA	$Ca_{10}(PO_4)_6(OH)_2$	1,67	116,80	9.5–12.0 > 80°C

[a] Solubility in water at 25°C is given as the logarithm of the ion product of the formulas given with concentrations in mol/l

[b] These compounds cannot be precipitated from aqueous solutions and are formed only at elevated temperatures b-TCP > 800°C, a-TCP> 1125°C

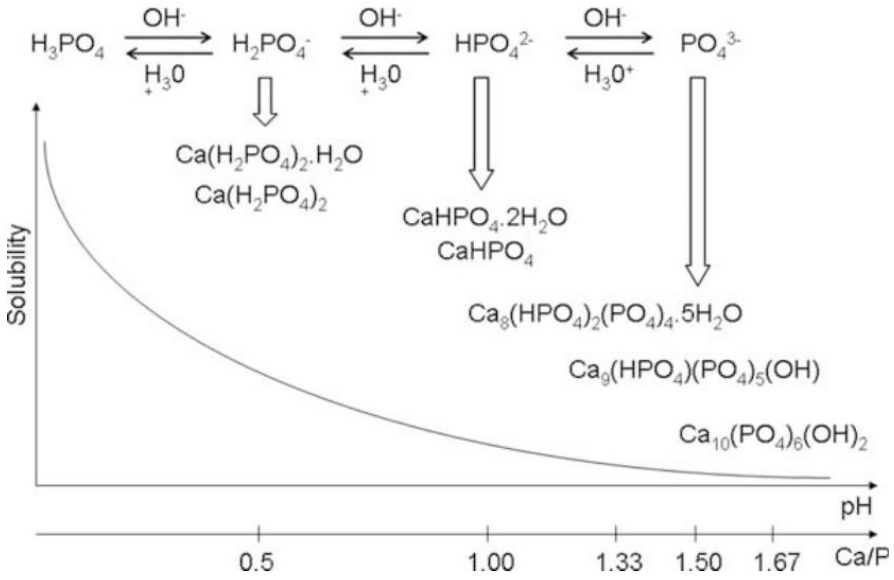

Figure 1.2. The inverse relationship between the increase in Ca/P ratio and solubility of calcium phosphates (Source: León and Jansen 2009).

The solubility and acidity of the component phases of calcium phosphate minerals are inversely proportional to the Ca/P ratio as shown in Figure 4. In short, solubility and acidity increase with decreasing Ca/P ratio (León, and Jansen, 2009). The properties of common calcium phosphate phases are listed in Table 1.1, along with some other common precursors (Leó, and Jansen, 2009). The in vivo behavior of calcium phosphate components is largely inferred and understood from their solubility. The in vivo degradation rate ranking of calcium phosphate components at pH 7.0 is as follows:

$$\text{MCPM} > \text{TTCP} = \alpha\text{-TCP} > \text{DCPD} > \text{DCP} > \text{OCP} > \beta\text{-TCP} > \text{HAP} \qquad (1.2)$$

The surface of a component of calcium phosphate with low stability in solution is reactive and can be coated with a more stable calcium phosphate component, thus increasing the stability of the component with low stability. Therefore, although all parameters except the calcium phosphate component are kept constant in the experimental environment, this order is not always observed experimentally (Bohner, 2000).

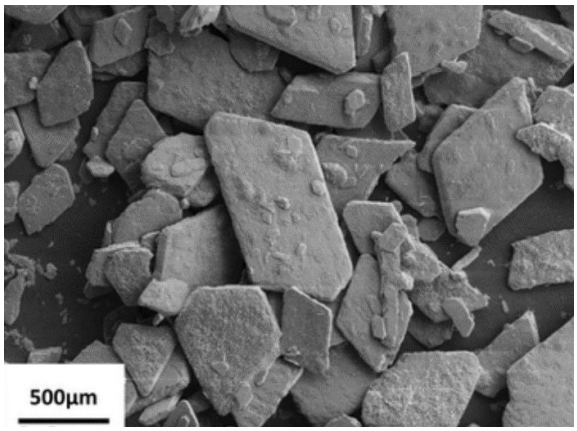

Figure 1.3. SEM image of the morphology of MCPM crystals. (Source: Unosson, 2014)

Monocalcium phosphate monohydrate (MCPM; $Ca(H_2PO_4)_2.H_2O$) is the least stable and most acidic calcium phosphate component phase. It has a monoclinic crystal structure with lattice parameters a) 5.812 b) 15.180 c) 6.239Å, β) 116.42°. Figure 1.2 shows the crystal morphology of MCPM and the morphology of this component phase resembles thin plates (Unosson, 2014). The precipitation conditions of the anhydrous form of the monocalcium phosphate phase are at temperatures above 100 °C and in highly acidic solution conditions. In terms of biocompatibility, MCPM alone is not sufficient for tissue substitution due to its acidic phase and low stability. However, it is suitable for tissue substitution in combination with basic calcium phosphate compounds (Bohner, 2000). An example of this situation is the transition of the MCPM component phase to the DCPM component phase by forming a compact structure with the basic CaO structure. The reaction formulation of this situation is as follows:

$$3Ca(H_2PO_4)_2H_2O + 3CaO + 6H_2O \rightarrow 6CaHPO_4.2(H_2O) \quad (1.3)$$

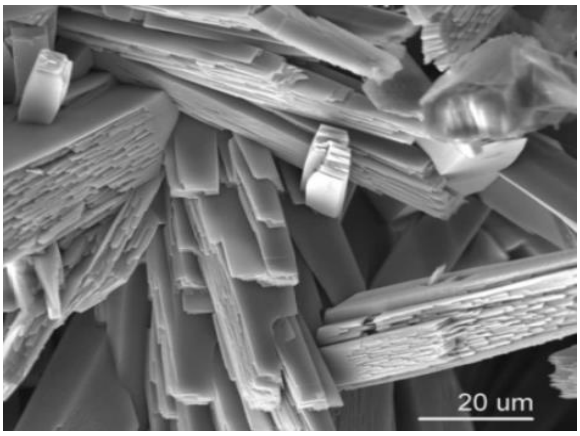

Figure 1.4. SEM image of the morphology of DCP crystals. (Source: Tas, and Bhaduri, 2004)

Dicalcium phosphate (DCP; $CaHPO_4$) is a calcium phosphate component phase with very good stability. This component phase is biocompatible and biodegradable. It has a triclinic crystal structure with lattice parameters a) 6.91, b) 6.627, c) 6.998Å, α) 96.34°, β) 103.82°, γ) 88.33°. Mohr hardness is 3.5 (Kodaka et al, 1999). The molecular structure of the DCP component phase consists of CaHPO4 chains linked by Ca-O bonds and three types of hydrogen bonds. Figure 1.3 shows the crystal morphology of DCP (Xu, Butler, and Gilson, 1999).

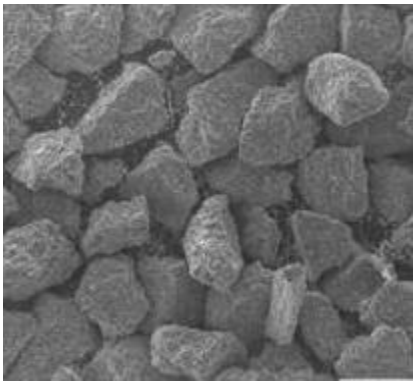

Figure 1.5. SEM image of the morphology of β-TCP crystals. (Source: Bohner 2000)

β-Tricalcium phosphate (β-TCP; β-$Ca_3(PO_4)_2$) has lattice parameters a=b) 10.4183, c) 37.3464 Å, γ) 120°. β-TCP has a rhombohedral crystal structure. It can be synthesized by heat treatment at 650°C and above. Figure 1.3 shows the crystal morphology of β-TCP. β-TCP phase components have degradable structures and are synthesized by osteoclastic activity. β-TCP is the main building block of brushite CPC (Bohner, 2000). The formulation of brushite is as follows:

$$\beta\text{-}Ca_3(PO_4)_2 + Ca(H_2PO_4)_2.H_2O + 7H_2O \rightarrow 4CaHPO_4.2H_2O \quad (1.4)$$

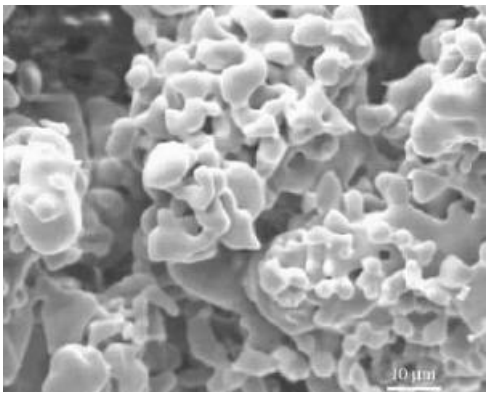

Figure 1.6. SEM image of the morphology of β-TCP crystals (Source: Bohner 2000).

α-Tricalcium phosphate (α-TCP; α-$Ca_3(PO_4)_2$) has the same chemical composition as β-TCP, but these two structures have a completely different crystallographic structure. α-TCP has a monoclinic structure with lattice parameters of a) 12.887, b) 27.280, c) 15.219Å, β) 126.20°. This difference makes the α-TCP component phase more soluble than β-TCP. α-TCP is a biocompatible component phase. The biodegradability of α-TCP is better than that of β-TCP (Bohner, 2000). The crystal morphology of α-TCP is shown in Figure 1.5. The α-TCP component phase is synthesized by heating the β-TCP component phase to a minimum of 1125°C and quenching it to prevent reverse transformation. α-TCP can easily transform into the HA component phase

thanks to a Ca/P molar ratio of 1.50 in an aqueous Ca/P solution used to make apatite CPC. The reactions of α-TCP with water are as follows:

$$\alpha\text{-}Ca_3(PO_4)_2 + 6H_2O \rightarrow 2CaHPO_4 \cdot 2H_2O + Ca(OH)_2 \quad \text{(in acidic region)} \qquad (1.5)$$

$$3\alpha\text{-}Ca_3(PO_4)_2 + 7H_2O \rightarrow Ca_8H_2(PO_4)_6 \cdot 5H_2O + Ca(OH)_2 \quad \text{(in neutral region)} \qquad (1.6)$$

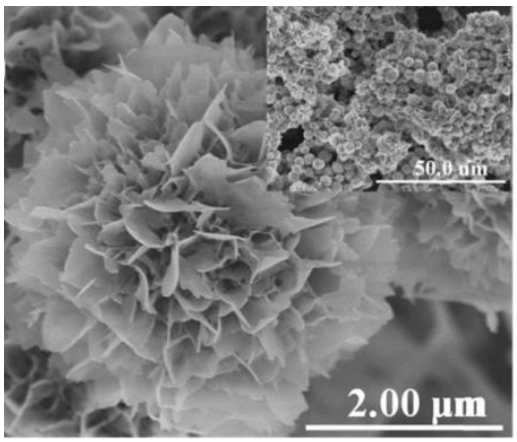

Figure 1.7. FESEM and TEM image of the morphology of β-TCP crystals (Source: Zhu et al. 2020).

Octacalcium phosphate (OCP; $Ca_8H_2(PO_4)_6.5H_2O$) has a leading role in the formation of apatite calcium phosphates, especially in teeth, bones, and other biominerals. It has a triclinic crystal structure with lattice parameters a) 19.692, b) 9.523, c) 6.835Å, α) 90.15°, β) 92.54°, γ) 108.65°. The crystal morphology of OCP is shown in Figure 1.5 and the morphology of this component phase has a needle-like crystal structure (Zhu et al, 2020; Gbureck et al, 2004). The OCP component phase is a highly biocompatible structure and can be biodegradable and osteoconductive. This component phase is difficult to obtain because OCP is a very slow crystallizing structure. The OCP component phase is a metastable structure. OCP usually occurs as a transient intermediate in the precipitation of HA, which is thermodynamically more stable (Bohner, 2000).

Hydrolysis of OCP to apatite phases can occur by dissolution of OCP followed by precipitation of HA or by direct solid-state transformation:

$$Ca_8H_2(PO_4)_6 \cdot 5H_2O + 2Ca_2+ \rightarrow Ca_{10}(PO_4)_6(OH)_2+4H^+ + 3H_2O \qquad (1.7)$$

OCP has a crystal structure similar to HA. These two component phases grow epitaxially on each other. OCP has an appetite structure. A layered structure of OCP includes hydrated layers (Johnsson, and Nancollas, 1992).

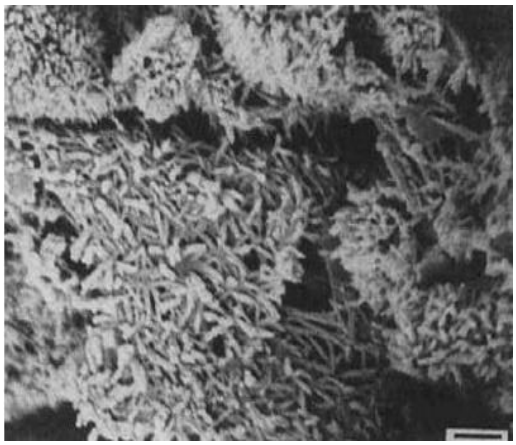

Figure 1.8. Morphology of HA crystals (Source: Ishikawa, Eanes, and Tung 1994).

The component phase of precipitated hydroxyapatite (PHA; $Ca_{10-x}(HPO_4)_x(PO_4)_x(PO_4)_{6-x}(OH)_{2-x}$) is a highly complex structure. The reason for this complex chemistry may be that precipitated hydroxyapatite is synthesized at a Ca/P molar ratio between 1.50 and 1.67. This difference in the Ca/P molar ratio causes differences in the chemistry of the component. For example, when the Ca/P molar ratio is 1.50, PHA components form the so-called calcium-deficient hydroxyapatite (CDHA) or tricalcium phosphate (TCP). a) 9.84214, b=2a, c) 6.8814Å, γ) 120° lattice parameters with a more stable monoclinic or hexagonal crystal structure. In the phase component structure of PHA, the phosphate ion rows are located along the a-axis, while calcium and hydroxide

ions are located between the phosphate groups (Wang, and Nancollas, 2008). The PHA phase component in biological apatite has the lattice parameters a=b) 9.4302, c) 6.8911Å, γ) 120° and has a structure close to hexagonal and monoclinic form. With decreasing Ca/P molar ratio, the crystallinity and crystal size decrease, increasing PHA solubility. PHA can transform into different phase forms when heated. For example, β-TCP (Ca/P = 1.50), a mixture of β-TCP and HA (1.67 > Ca/P > 1.50), or pure HA (Ca/P = 1.67) decomposes upon heating the PHA compound form (Bohner, 2000). When the solution medium is prepared at low supersaturations and low pH, the crystalline forms grow into needle-like structures in the c-axis direction, the length of which increases with the degree of reaction. Figure 1.6 shows the needle morphology of the PHA component form. This type of nucleation at low supersaturations is called primary nucleation. PHA precipitates faster at higher supersaturations. HA is the most stable phase for a wide pH range (Ishikawa, Eanes, and Tung, 1994).

1.7 Hypothesis and Objective of Thesis

The formation of hard tissues such as bones and teeth in vertebrates, especially humans, and shells in invertebrate mollusks is part of biomineralization. Biomineralization is a fundamental biological phenomenon that drives the coordinated deposition and growth of inorganic ions and organic protein molecules in various organisms. The unique properties of hard mineral tissues produced by the biomineralization process in living organisms, such as strength, hardness, and flexibility, are regulated by this process. Controlling biomineralization is vital for addressing medical and dental conditions significantly impacting healthcare costs and quality of life. Effective management of biomineralization can prevent undesirable occurrences such as vascular calcification and promote beneficial processes such as bone and tooth remineralization. Hydroxyapatite (HA), $Ca_{10}(PO_4)_6(OH)_2$, the major inorganic compound of mammalian bone and dental tissues, is one of the most stable forms of calcium phosphates. A better understanding of the crystallization mechanism of hydroxyapatite (HA) in the natural mineralization synthesis process and its applicability as an industrial material is being deeply investigated in numerous interdisciplinary fields. Morphology,

biocompatibility, bioactivity, bioactivity, bioabsorbability, osteoconductivity, and surface functionalization in biomimetic HAp crystals represent the physical and chemical properties required to optimize applicability as industrial materials. Synthetic hydroxyapatites synthesized from Ca/P minerals by mimicking natural biomineralization processes exhibit good properties such as direct binding to tissue, biocompatibility, bioactivity, osteoconductivity, etc., which is exciting for applications in restorative dental treatment fields. A fundamental aspect of this process involves precisely controlling the morphology and kinetics of mineral formation, which can produce materials with specific properties and functions.

This thesis aims to control the morphology and kinetics of calcium phosphate mineralization using small enzymes identified through deep-directed evolution. A peptide-phage library was used to select short-sequence peptides (12 amino acids) from a physiological environment that significantly influences the mineralization kinetics and morphology of calcium phosphate minerals. Through iterative experiments, the optimal conditions for variables such as pH, temperature, and molarity were set, recognizing their dynamic impact on the mineralization process. Structural characterization using XRD and FTIR analyses confirmed the formation of hydroxyapatite in the presence of these peptides. Kinetic measurements revealed that these peptides catalyze calcium phosphate mineralization approximately one order of magnitude faster under physiological conditions. These peptides have the potential for the development of clinical products such as dental gels, toothpaste formulations, and bone regeneration treatments.

CHAPTER 2

MATERIAL AND METHODS

2.1 Optimizing the Selective Pressure for Identifying Mineralizing Peptides

2.1.1 Optimization of Ca/P Precipitation in HEPES Buffer with pH, Temperature, and Ionic Concentration

50 mM HEPES, 9.6 mM $CaCl_2.2H_2O$, and 5.76 mM KH_2PO_4 buffers were prepared. Each solution was divided into 7 and these solutions were pH adjusted with 1M NaOH at 25 °C to pH 6.6, 6.8, 7.0, 7.2, 7.4, 7.6, 7.8. Then each solution was heated to 37 °C and pH changes were controlled. To test the mineralization kinetics of these solutions, 100 µl of $CaCl_2.2H_2O$ buffer (9.6 mM, pH 6.6- 7.8) and 100 µl of KH_2PO_4 buffer (5.76 mM, pH 6.6- 7.8) (total volume 200 µl; Ca^{2+}/PO_4^{3-}: 4.8/2.88(1x) mM) were mixed in well plates respectively and mineralization kinetics were measured with a spectrophotometer (Thermo Fisher Scientific, Multiscan go 1510, Spectrophotometer) at 820 nm at 25 °C for 1 hour. The experiment was repeated 3 times.

The solutions were heated to 37 °C in a water bath (Nuve, NB 20, Water Bath). 100 µl of $CaCl_2.2H_2O$ buffer (9.6 mM, pH 6.6- 7.8) and 100 µl of KH_2PO_4 buffer (5.76 mM, pH 6.6- 7.8) (total volume 200 µl; Ca^{2+}/PO_4^{3}: 4.8/2.88(1x) mM) were mixed in well plates respectively and mineralization kinetics were measured with a spectrophotometer at 820 nm at 37 °C for 1 hour. The experiment was repeated 3 times.

2.1.2 Optimization of Ca/P Precipitation in Tris Buffer with pH, Temperature, and Ionic Concentration

20 mm Tris, 9.6 mM $CaCl_2.2H_2O$, and 5.76 mM KH_2PO_4 buffers were prepared. Each solution was divided into 7 parts and these solutions were pH adjusted with 1M NaOH at 25°C to pH 6.6, 6.8, 7, 7.2, 7.4, 7.6, 7.8. Then each solution was heated to 37°C and pH changes were controlled. To test the effect of molarity on mineralization kinetics, 100 µl $CaCl_2.2H_2O$ solution (9.6 mM, pH 6.6- 7.8) and 100 µl KH_2PO_4 solution (5.76 mM, pH 6.6- 7.8) (total volume 200 µl; Ca^{2+}/PO_4^{3-}: 4.8/2.88(1x) mM, each sample was added to 3 wells) were mixed in well-plats respectively. Mineralization kinetics were measured with a spectrophotometer at 820 nm at 25°C for 1 hour. The experiment was repeated 3 times.

20 mm Tris, 9.6 mM $CaCl_2.2H_2O$, and 5.76 mM KH_2PO_4 buffers were prepared. The solutions were heated to 37°C in a water bath (Nuve, NB 20, Water Bath). Each solution was divided into 5 and the pH of each solution was adjusted with 1M NaOH to pH 6.6, 6.8, 7, 7.2, and 7.4 at 37°C. Then each solution was cooled to 25°C and pH changes were controlled. To test the effect of molarity on mineralization kinetics, 100 µl of $CaCl_2.2H_2O$ solution (9.6 mM, pH 6.6- 7.4) and 100 µl of KH_2PO_4 solution (5.76 mM, pH 6.6- 7.4) (total volume 200 µl; Ca^{2+}/PO_4^{3-}: 4.8/2.88(1x) mM, each sample was added to 3 wells) were mixed in well-plats respectively and mineralization kinetics were measured by spectrophotometer at 820 nm at 37°C for 1 hour. The experiment was repeated 3 times.

2.1.3 Optimization of Ca/P Precipitation by Ionic Concentration at Constant pH, Temperature, and HEPES Buffer

50 mM HEPES, 19.2 mM $CaCl_2.2H_2O$ and 11.52 mM KH_2PO_4 buffers were prepared at 25C, pH 7. To test the effect of molarity on mineralization kinetics, 66 µl $CaCl_2.2H_2O$ solution (19.2 mM, pH 7), 66 µl KH_2PO_4 solution (11.52 mM, pH 7), and 66 µl HEPES buffer (50 mM, pH 7) (total volume 200 µl; Ca^{2+}/PO_4^{3-} molarity = 1.32X (6.46/3.8 mM), each sample was added to 3 wells) were mixed in well plates respectively.

50µl $CaCl_2.2H_2O$ solution (19.2 mM, pH 7), 50µl KH_2PO_4 solution (11.52 mM, pH 7), and 100µl HEPES buffer (50 mM, pH 7) (total volume 200µl; Ca^{2+}/PO_4^{3-} molarity = 1X (4.8/2.88 mM), each sample added to 3 wells) were mixed in well-plats respectively. 37.5µl $CaCl_2.2H_2O$ solution (19.2 mM, pH 7), 37.5µl KH_2PO_4 solution (11.52 mM, pH 7), and 125µl HEPES buffer (50 mM, pH 7) (total volume 200µl; Ca^{2+}/PO_4^{3-} molarity = 0.75X (3.6/2.16 mM), each sample added to 3 wells) were mixed in well-plats. 33 µl $CaCl_2.2H_2O$ solution (19.2 mM, pH 7), 33 µl KH_2PO_4 solution (11.52 mM, pH 7), and 132 µl HEPES buffer (50 mM, pH 7) (total volume 200 µl; Ca^{2+}/PO_4^{3-}: molarity = 0.66X (3.17/1.9 mM), each sample was added to 3 wells) were mixed in well plates respectively. 25 µl $CaCl_2.2H_2O$ solution (19.2 mM, pH 7), 25 µl KH_2PO_4 solution (11.52 mM, pH 7), and 150 µl HEPES buffer (50 mM, pH 7) (total volume 200 µl; Ca^{2+}/PO_4^{3-} molarity = 0.5X (2.4/1.44 mM), each sample added to 3 wells) were mixed in well plates. Mineralization kinetics of all these mixtures were measured with a spectrophotometer (Thermo Fisher Scientific, Multiscan go 1510, Spectrophotometer) at 820 nm at 25°C for 2 hours.

50 mM Tris-HCl and 150 mM NaCl buffers were prepared at 25°C (total volume 15 ml pH 7.5). The buffer was mixed with 15 ml glycerol. 50µl $CaCl_2.2H_2O$ solution (19.2 mM, pH 7), 50µl KH_2PO_4 solution (11.52 mM, pH 7), 90µl HEPES buffer (50 mM, pH 7), and 10µl TBS buffer with glycerol (total volume 200µl; Ca^{2+}/PO_4^{3-} molarity = 1X (4.8/2.88 mM), each sample added to 3 wells) were mixed in well plates respectively. 37.5µl $CaCl_2.2H_2O$ solution (19.2 mM, pH 7), 37.5µl KH_2PO_4 solution (11.52 mM, pH 7), 115µl HEPES buffer (50 mM, pH 7), and 10µl TBS buffer with glycerol (total volume 200µl; Ca^{2+}/PO_4^{3-} molarity = 0.75X (3.6/2.16 mM), each sample added to 3 wells) were mixed in well-plates. 33 µl $CaCl_2.2H_2O$ solution (19.2 mM, pH 7), 33 µl KH_2PO_4 solution (11.52 mM, pH 7), 122 µl HEPES buffer (50 mM, pH 7), 10 µl TBS buffer with glycerol (total volume 200 µl; Ca^{2+}/PO_4^{3-} molarity = 0.66X (3.17/1.9 mM), each sample added to 3 wells) were mixed in wellplats respectively. 25 µl $CaCl_2.2H_2O$ solution (19.2 mM, pH 7), 25 µl KH_2PO_4 solution (11.52 mM, pH 7), 140 µl HEPES buffer (50 mM, pH 7), 10 µl TBS buffer with glycerol (total volume 200 µl; Ca^{2+}/PO_4^{3-} molarity = 0.5X (2.4/1.44 mM), each sample added to 3 wells) were mixed in well plates. Mineralization kinetics of all these mixtures were measured with a spectrophotometer (Thermo Fisher Scientific, Multiscan go 1510, Spectrophotometer) at 820 nm at 25°C for 2 hours.

To prepare the precipitate, 333µl HEPES solution (50 mM, pH 7.00), 333µl KH_2PO_4 buffer (11.52 mM, pH 7.00), and 333µl $CaCl_2.2H_2O$ buffer (19.2 mM, pH 7.00)

were mixed in a 2 ml centrifuge tube with a total volume of 1000 µl respectively. The centrifuge tube was shaken on an orbital shaker (Maxi Lab Biotechnology, MS3-Maxi Shake60R, Shaking Incubator) at 150 rpm at 25°C for 2 hours. The sample was then precipitated in a centrifuge at 14000 rpm for 10 min. The supernatant was carefully transferred to a new tube and left in the tube without damaging the pellet.

30 ml of 0.2 mM Glycine buffer was prepared and the pH of the buffer was adjusted to pH 2.2 at 25°C by adding 1M HCl solution. 1M Trima Base (pH 9.13) solution was prepared at 25°C. The pH of the glycine buffer solution was increased to 7.5 by adding 1M Trisma Base solution in certain ratios (1000 µl, 500 µl, and 50 µl) to 0.2 mM Glycine buffer (pH 2.2) and the pH change was monitored with a pH meter (Thermo Scientific, Orion Star A211, pH Meter). It was determined that 5.4 ml Trisma Base solution was needed to increase the pH of 30 ml Glycine buffer to 7.5, and it was calculated that 160 µl Trisma Base solution was needed to increase the pH of 1 ml Glycine buffer to 7.5. 1 ml of 0.2M Glycine buffer was added to the mineral pellet left in a 2 ml centrifuge tube. The centrifuge tube was shaken on an orbital shaker at 100 rpm for 15 minutes at 25°C. 160 µl Trisma Base was added to the centrifuge tube. 200 µl of the solution was added to 3 wells of the centrifuge tube and the mixtures were monitored for mineralization formation by spectrophotometer (Thermo Fisher Scientific, Multiscan go 1510, Spectrophotometer) at 820 nm at 25°C for 1 hour.

2.2 Selection of Mineralizing Peptides by Directed Evolution Method

2.1.1 Biopanning 1

While the precipitation is being prepared, 240 µl HEPES solution (50 mM, pH 7.00), 125 µl KH_2PO_4 buffer (11.52 mM, pH 7.00), 125µl $CaCl_2.2H_2O$ buffer (19.2 mM, pH 7.00), and 10 µl Phage ($2x10^{11}$ pfu/ml; Ph.D.-12 Phage Display Peptide Library) total volume of 500 µl respectively, 2 ml mixed in a centrifuge tube. The centrifuge tube was shaken for 17 hours at 150 rpm at 25°C on an orbital shaker. The samples were precipitated for 10 minutes in a centrifuge at 14000 rpm. The supernatant was transferred

to a fresh tube and kept at +4°C. 1 ml of Glycine solution (0.2 M pH: 2.17) was added to the pellet to dissolve the precipitate. The pellet was thawed by placing the centrifuge tube in an orbital shaker at 100 rpm for 15 minutes. Then, the solution was neutralized with 160 µl of Trisma Base solution (0.91 M pH: 9.1).

The neutralized phage was stored overnight at +4. LB agar previously prepared and stored at room temperature was melted with a microwave oven for about 20 minutes. Then the temperature of LB agar was adjusted to 55°C with a hot water bath. The LB agar brought to 55°C was taken into 3 centrifuge tubes of 50 ml. To each LB agar, 50 µl tetracycline (1:1000 ratio) and 50 µl X-gal/IPTG (1:1000 ratio) were added and the tubes were turned upside down and poured into small petri dishes. LB agar was refrozen in petri dishes and stored at +4°C. In a 50 ml centrifuge tube, 20 ml of LB broth prepared in advance and stored at room temperature was taken. 20 µl tetracycline (1:1000 ratio) and 100 µl inoculation (1:200 ratio) were added to LB broth. E. coli culture was grown overnight at 37°C with an orbital shaker at 250 rpm. Then 50 µl tetracycline (1:1000 ratio) was added to a new 50 ml LB broth medium in a 250 ml flask 20 ml O/N culture was inoculated into this LB medium and E. coli culture was grown. When the O/N inoculated E. coli culture reached the early log phase (OD600: 0.01-0.05) (within 1-2 hours), 800 µl Phage was transferred to a 250 ml shaking flask (E. coli culture) and 250 ml and incubated at 37°C with shaking at 250 rpm for 4 hours. After 4 hours of growth, 50 ml of E. coli/phage culture was transferred to 250 ml Nalgene sterile centrifuge tubes. Nalgene centrifuge tubes were spun at 8000 rpm for 20 min and E. coli was precipitated. The supernatant containing phage was transferred to a sterile 250 ml Nalgene centrifuge tube. 8.3 ml of PEG/NaCl solution was added to ~ 50 ml of supernatant (1:6; v/v), mixed thoroughly on the vortex and left at O/N at 4°C. The centrifuge temperature was adjusted to 4°C. E. coli/phage culture treated with PEG and stored o/n 4°C was spun at 8000 rpm for 20 min. the phage pellet was obtained at the bottom of a 250 ml Nalgene centrifuge tube. the supernatant containing E. coli was transferred to a 50 ml sterile centrifuge tube labeled BP1-S2 (amplified) and stored at 4°C. The phage pellet was resuspended with 5 ml TBS buffer, thawed by pipetting and vertexing, and transferred to a 50 ml sterile centrifuge tube, centrifuged at 8000 rpm for 10 min. The phage supernatant was transferred to a sterile 50 ml Nalgene centrifuge tube. 830 µl PEG/NaCl solution was added to ~ 5 ml supernatant (1:6; v/v), mixed thoroughly, and left on ice for 2 hours for phage precipitation. It was spun at 10000 rpm for 10 min to obtain precipitated phages. The supernatant containing E. coli was collected in a 15 ml sterile centrifuge tube labeled

BP1-S3 (amplified) and stored at 4°C. The phage pellet was resuspended in 1 ml TBS buffer and dissolved by shaking. The solution was transferred to a 1.5 ml sterile centrifuge tube and spun at 10000 rpm for 10 min. The phage-containing supernatant was transferred to a 1.5 ml sterile centrifuge tube and spun at 13200 rpm for 3 min. E. coli-containing supernatant was removed into a 1.5 ml sterile centrifuge tube labeled BP1-S4 (amplified) and stored at 4°C. The phage pellet was resuspended with 200 µl TBS buffer and the pellet was gently dissolved by pipetting. the solution was spun at 13200 rpm for 2 min. The phage supernatant was transferred to a 1.5 ml sterile centrifuge tube labeled BP1-M2 (amplified, purified) and stored at 4°C. BP1-M2 (Phage pellet) was kept in O/N at 4°C. 200 µl of glycerol (50% glycerol, total volume 400 µl) was added to 200 µl of BP1-M2 (amplified, purified) solution, the solution was mixed thoroughly with the help of a vortex and stored at -20 °C.

190 µl TBS buffer was added to the A1-B1 well of the 96-well plate. 180 µl TBS buffer was added to the A2-A9, B2-B12 wells of the 96-well plate. 10 µl BP1-M1 phage solution was added to well A1, 10 µl BP1-M2 solution was added to well B1 of 96-well plate. solutions were mixed by pipetting up and down for 10 seconds with sterile pipette tips. The 96-well plate was placed on an orbital shaker (lid closed) and shaken at 150 rpm for 2 min. 20 µl of solution mixture was transferred from A1 to A2; B1 to B2; C1 to C2; D1 to D2. solutions were mixed by pipetting up and down for 10 seconds with sterile pipette tips. The 96-well plate was placed on an orbital shaker (lid closed) (Hangzhou Miu, GS-20, Orbital Shaker) and shaken at 150 rpm for 2 min. These steps were repeated until a solution was transferred to wells A9-B9-C12-D12.

In a 50 ml centrifuge tube, 20 ml of LB broth prepared in advance and stored at room temperature was taken. 20 µl tetracycline (1:1000 ratio) and 100 µl inoculation (1.200 ratio) were added to LB broth. E. coli culture was grown overnight at 37°C at 250 rpm with an orbital shaker. Then, 50 µl tetracycline (1:1000 ratio) was added to the new 50 ml LB broth medium in the 250 ml flask and the E. coli culture was grown by inoculating this LB medium with 20 ml O/N culture. When the O/N inoculated E. coli culture reached the mid-log phase (OD600: 0.34) (in 3-4 hours). LB Agar/IPTG/X-gal plates were placed at 37°C for warming (not more than 1 hour). The top Agar medium (100 ml) was melted in the microwave and the flask was placed in a 55°C water bath. 50 ml of the melted Top Agar was aliquoted into a 50 ml sterile falcon tube. 50 µl tetracycline (1:1000) was added to the Top Agar. 3 ml of LB agar was divided into 15 ml falcon tubes (6 portions in total). Falcon tubes containing Top Agar were placed in a 45°C water bath

(Nuve, NB 20, Water Bath) to be kept in the molten state. 180 µl of E. coli culture was mixed with 20 µl of phage from selected wells (A5-7-9; B10-11-12) in a sterile 1.5 ml sterile centrifuge tube (6 plates in total). The E.coli and phage were mixed by pipetting and each mixture (200 µl E.coli/phage) was mixed into 3 ml of molten Top Agar. The E.coli and phage mixture was poured onto the LB Agar/X-gal/IPTG-tetracycline plates. The plates were kept at room temperature for 5 minutes until the ball agar solidified. The agar plate was inverted and incubated (Nuve, EN 500, Incubator) at 37°C overnight (not more than 18 hours). Blue colonies were counted and the amount of phage in each elution fraction was calculated. 6 µl BP1-M2 solutions were taken into ependorf tubes. Both samples were subjected to 2 technical repetitive nanodrops (Thermo Fisher Scientific, Nanodrop 8000, Spectrophotometer) measurements, and the amount of phage in each elution fraction was calculated.

To test the effect of BP1-M2 phage libraries on mineralization kinetics, 200µl HEPES buffer (50mM, pH 7, each sample was added to 2 wells) was added in well-plats. 40µl $CaCl_2.2H_2O$ solution (19.2 mM, pH 7), 40µl KH_2PO_4 solution (11.52 mM, pH 7), and 120µl HEPES buffer (50 mM, pH 7) (total volume 200µl; Ca^{2+}/PO_4^{3-} molarity = 0.8X (3.84/2.3mM), each sample was added to 3 wells) were mixed in well plates respectively. 50µl $CaCl_2.2H_2O$ solution (19.2 mM, pH 7), 50µl KH_2PO_4 solution (11.52 mM, pH 7), 100µl HEPES buffer (50 mM, pH 7) (total volume 200µl; Ca^{2+}/PO_4^{3-} molarity = 1X (4.8/2.88 mM), each sample added to 3 wells) were mixed in well plates respectively. 50 µl $CaCl_2.2H_2O$ solution (19.2 mM, pH 7), 50 µl KH_2PO_4 solution (11.52 mM, pH 7), 97.6 µl HEPES buffer (50 mM, pH 7) and 2.4 µl BP1-M2 phage library (8, 14E+12 pfu/ml, with glycerol) (total volume 200 µl; Ca^{2+}/PO_4^{3-} molarity = 1X (4.8/2.88 mM), each sample was added to 3 wells) were mixed in well plates respectively. 60 µl $CaCl_2.2H_2O$ solution (19.2 mM, pH 7), 60 µl KH_2PO_4 solution (11.52 mM, pH 7), and 80 µl HEPES buffer (50 mM, pH 7) (total volume 200 µl; Ca^{2+}/PO_4^{3-} molarity = 1.2X (5.76/3.46 mM), each sample added to 3 wells) were mixed in well plates respectively. 66 µl $CaCl_2.2H_2O$ solution (19.2 mM, pH 7), 66 µl KH_2PO_4 solution (11.52 mM, pH 7), and 66 µl HEPES buffer (50 mM, pH 7) (total volume 200 µl; Ca^{2+}/PO_4^{3-} molarity = 1.33X (6.46/3.84 mM), each sample added to 3 wells) were mixed in well plates respectively. Mineralization kinetics of all these mixtures were measured by spectrophotometer (Thermo Fisher Scientific, multiscan go) at 820 nm at 25°C for 17 hours.

2.1.2 Biopanning 2

While the precipitation is being prepared, 240 µl HEPES solution (50 mM, pH 7.00), 125 µl KH2PO4 buffer (11.52 mM, pH 7.00), 125µl $CaCl_2.2H_2O$ buffer (19.2 mM, pH 7.00), and 5 µl BP1-M2 Phage (Final Volume: 500 µl; $2x10^{11}$ pfu/ml), respectively, 2 ml mixed in a centrifuge tube. The centrifuge tube was shaken for 17 hours at 150 rpm at 25°C on an orbital shaker. Following that, the samples were precipitated for 10 minutes in a centrifuge at 14000 rpm. The supernatant was transferred to a fresh tube, labeled as BP2-S1, and kept at +4 °C. 500 µl of Wash Buffer I was added to the pellet and the pellet was thawed at 25°C for 5 minutes on an orbital shaker at 100 rpm. the samples were precipitated for 10 minutes in a centrifuge at 14000 rpm. The supernatant was transferred to a fresh tube, labeled as BP2-S2, and kept at +4 °C. 500 µl of Wash Buffer I was added to the pellet and the pellet was thawed at 25°C for 5 min on an orbital shaker at 100 rpm. the samples were precipitated for 10 minutes in a centrifuge at 14000 rpm. The supernatant was transferred to a fresh tube, labeled as BP2-S3, and kept at +4 °C. 1 ml of Glycine solution (0.2 M pH: 2.17) was added to the pellet to dissolve the precipitate. The pellet was dissolved by placing the centrifuge tube on an orbital shaker at 100 rpm for 15 min. The solution was then neutralized with 160 µl of Trizma Base solution (0.91 M pH: 9.1).

In a 50 ml centrifuge tube, 20 ml of LB broth prepared in advance and stored at room temperature was taken. 20 µl tetracycline (1:1000 ratio) and 100 µl inoculation (1.200 ratio) were added to LB broth. E.coli culture was grown overnight at 250 rpm at 37°C with an orbital shaker. Then, 50 µl tetracycline (1:1000 ratio) was added to the new 50 ml LB broth medium in the 250ml flask and the E. coli culture was grown by inoculating this Lb medium with 20 ml O/N culture. When the O/N inoculated E. coli culture reached the early log phase (OD600: 0.01-0.05) (in 1-2 hours), 800 µl Phage was transferred to a 250 ml shake flask (E. coli culture) and 250 ml. It was incubated for 4 hours with shaking at 250 rpm at 37°C. After 4 hours of growth, 50 ml of E. coli/phage culture was transferred to 250 ml Nalgene sterile centrifuge tubes. Nalgene centrifuge tubes were spun at 8000 rpm for 20 min and E. coli was precipitated. The supernatant containing phage was transferred to a sterile 250 ml Nalgene centrifuge tube. 8.3 ml of PEG/NaCl solution was added to ~ 50 ml of supernatant (1:6; v/v), mixed thoroughly on

the vortex and left at O/N at 4°C. The centrifuge temperature was adjusted to 4°C. PEG-treated e.coli/phage culture stored at O/N 4°C was spun at 8000 rpm for 20 min. The phage pellet was obtained at the bottom of a 250 ml Nalgene centrifuge tube. The supernatant containing the e.coli was transferred to a 50 ml sterile centrifuge tube labeled BP2-S4(amplified) and stored at 4°C. The phage pellet was resuspended with 5 ml TBS buffer, thawed by pipetting and vortexing, and transferred to a 50 ml sterile centrifuge tube, centrifuged at 8000 rpm for 10 min. The supernatant containing phage was transferred to a sterile 50 ml Nalgene centrifuge tube. 830 µl PEG/NaCl solution was added to ~ 5 ml supernatant (1:6; v/v), mixed thoroughly, and left on ice for 2 hours for phage precipitation. The precipitated phages were spun at 10000 rpm for 10 min to obtain the precipitated phages. The supernatant containing E. coli was collected in a 15 ml sterile centrifuge tube labeled BP2-S5 (amplified) and stored at 4°C. The phage pellet was resuspended in 1 ml TBS buffer and dissolved by shaking. The solution was transferred to a 1.5 ml sterile centrifuge tube and spun at 10000 rpm for 10 min. The phage-containing supernatant was transferred to a 1.5 ml sterile centrifuge tube and spun at 13200 rpm for 3 min. The supernatant containing E. coli was removed into a 1.5 ml sterile centrifuge tube labeled BP2-S6 (amplified) and stored at 4°C. The phage pellet was resuspended with 200 µl TBS buffer and the pellet was gently dissolved by pipetting. the solution was spun at 13200 rpm for 2 min. The supernatant containing phage was transferred to a 1.5 ml sterile centrifuge tube labeled BP2-M2 (amplified, purified) and stored at 4°C. Bp2-m2 (phage pellet) was kept in O/N at 4°C. 200 µl of glycerol (50% glycerol, total volume 400ul) was added to 200 µl of BP2-M2 (amplified, purified) solution, the solution was mixed thoroughly with the help of a vortex and stored at -20 °C.

190 µl TBS buffer was added to well A1-B1 of the 96-well plate. 180 µl TBS buffer was added to wells A2-A9, and B2-B12 of the 96-well plate.10 µl BP2-M1 solution was added to well A1, 10 µl BP2-M2 solution was added to well B1 of the 96-well plate. solutions were mixed by pipetting up and down for 10 seconds with sterile pipette tips. The 96-well plate was placed on an orbital shaker (lid closed) and shaken at 150 rpm for 2 minutes. 20 µl of the solution mixture was transferred from A1 to A2; and B1 to B2. solutions were mixed by pipetting up and down for 10 seconds with sterile pipette tips. The 96-well plate was placed on an orbital shaker (lid closed) and shaken at 150 rpm for 2 min. These steps were repeated until a solution was transferred to wells A9-B12.

In a 50 ml centrifuge tube, 20 ml of LB broth prepared in advance and stored at room temperature was taken. 20 µl tetracycline (1:1000 ratio) and 100 µl inoculation

(1:200 ratio) were added to LB broth. E. coli culture was grown overnight at 37°C at 250 rpm with an orbital shaker. Then, 50 µl tetracycline (1:1000 ratio) was added to the new 50 ml LB broth medium in the 250ml flask and the E. coli culture was grown by inoculating this Lb medium with 20 ml O/N culture. When the O/N inoculated E. coli culture reached the mid-log phase (OD600: 0.34) (in 3-4 hours). LB Agar/IPTG/X-gal plates were placed at 37°C for warming up (not more than 1 hour). The top Agar medium (100 ml) was melted in the microwave and the flask was placed in a 55°C water bath. 50 ml of the melted Top Agar was divided into a 50 ml sterile falcon tube. 50 µl tetracycline (1:1000) was added to the Top Agar. 3 ml of LB agar was divided into 15 ml falcon tubes (6 portions in total). Falcon tubes containing Top Agar were placed in a 45°C water bath to be kept in the molten state. 180 µl E. coli culture was mixed with 20 µl phage from selected wells (A5-7-9; B10-11-12) in a sterile 1.5 ml sterile centrifuge tube (6 plates in total). The E. coli and phage were mixed by pipetting and each mixture (200 µl E. coli/phage) was mixed into 3 ml molten Top Agar. The E. coli and phage mixture was poured onto the LB Agar/X-gal/IPTG-tetracycline plates. The plates were kept at room temperature for 5 minutes until the ball agar solidified. The agar plate was inverted and incubated overnight at 37°C (no longer than 18 hours). Blue colonies were counted and the amount of phage in each elution fraction was calculated. 6 µl of BP1-M2, and 6 µl of BP2-M2 phage solutions were added to Eppendorf tubes. Both samples were subjected to 2 technical repetitive nanodrop measurements and the amount of phage in each elution fraction was calculated.

2.1.3 Biopanning 3

While the precipitation is being prepared, 240 µl HEPES solution (50 mM, pH 7.00), 125 µl KH2PO4 buffer (11.52 mM, pH 7.00), 125µl $CaCl_2.2H_2O$ buffer (19.2 mM, pH 7.00), and 14 µl BP2-M2 Phage (Final Volume: 500 µl; $2x10^{11}$ pfu/ml), respectively, 2 ml mixed in a centrifuge tube. The centrifuge tube was shaken for 17 hours at 150 rpm at 25°C on an orbital shaker. Following that, the samples were precipitated for 10 minutes in a centrifuge at 14000 rpm. The supernatant was transferred to a fresh tube, labeled as BP3-S1, and kept at +4 °C. 500 µl of Wash Buffer I was added to the pellet and the pellet

was dissolved for 5 min at 25°C on an orbital shaker at 100 rpm. Samples were precipitated for 10 min in a centrifuge at 14000 rpm. The supernatant was transferred to a new tube, labeled BP3-S2, and kept at +4 °C. 500 µl of Wash Buffer II was added to the pellet and the pellet was thawed for 5 min at 25°C on an orbital shaker at 100 rpm. samples were precipitated for 10 min in a centrifuge at 14000 rpm. The supernatant was transferred to a new tube, labeled BP3-S3, and kept at +4 °C. 1 ml of Glycine solution (0.2 M pH: 2.17) was added to the pellet to dissolve the precipitate. The pellet was dissolved by placing the centrifuge tube on an orbital shaker at 100 rpm for 15 min. The solution was then neutralized with 160 µl of Trizma Base solution (0.91 M pH: 9.1).

In a 50 ml centrifuge tube, 20 ml of LB broth prepared in advance and stored at room temperature was taken. 20 µl tetracycline (1:1000 ratio) and 100 µl inoculation (1,200 ratio) were added to the LB broth. E. coli culture was grown overnight at 37C at 250 rpm with an orbital shaker. Then 50 µl tetracycline (1:1000 ratio) was added to a new 50 ml LB broth medium in a 250 ml flask 20 ml O/N culture was inoculated into this LB medium and E. coli culture was grown. When the O/N inoculated E. coli culture reached the early log phase (OD600: 0.01-0.05) (within 1-2 hours), 800 µl Phage was transferred to a 250 ml shaking flask (E. coli culture) and 250 ml. Incubated at 37°C with shaking at 250 rpm for 4 hours. After 4 hours of growth, 50 ml of E. coli/phage culture was transferred to 250 ml Nalgene sterile centrifuge tubes. Nalgene centrifuge tubes were spun at 8000 rpm for 20 minutes and E. coli was precipitated. The supernatant containing phage was transferred to a sterile 250 ml Nalgene centrifuge tube. 8.3 ml of PEG/NaCl solution was added to ~50 ml of supernatant (1:6; v/v), mixed thoroughly on the vortex and left at O/N at 4°C. The centrifuge temperature was adjusted to 4°C. E.coli/phage culture treated with PEG and stored o/n at 4°C was spun at 8000 rpm for 20 min. the phage pellet was obtained at the bottom of a 250 ml Nalgene centrifuge tube. The supernatant containing E. coli was transferred to a 50 ml sterile centrifuge tube labeled BP3-S4 (amplified) and stored at 4°C. The phage pellet was resuspended with 5 ml TBS buffer, thawed by pipetting and vortexing, and transferred to a 50 ml sterile centrifuge tube, centrifuged at 8000 rpm for 10 min. The supernatant containing phage was transferred to a sterile 50 ml Nalgene centrifuge tube. 830 µl of PEG/NaCl solution was added to ~ 5 ml of supernatant (1:6; v/v), mixed thoroughly, and left on ice for 2 hours for phage precipitation. The supernatant was spun at 10000 rpm for 10 minutes to obtain precipitated phages. The supernatant containing E. coli was collected in a 15 ml sterile centrifuge tube labeled BP3-S5 (amplified) and stored at 4°C. The phage pellet was

resuspended in 1 ml TBS buffer and dissolved by shaking. The solution was transferred to a 1.5 ml sterile centrifuge tube and spun at 10000 rpm for 10 min. The phage-containing Supernatant was transferred to a 1.5 ml sterile centrifuge tube and spun at 13200 rpm for 3 minutes. E. coli-containing Supernatant was removed into a 1.5 ml sterile centrifuge tube labeled BP3-S6 (amplified), and stored at 4°C. The phage pellet was resuspended with 200 µl TBS buffer and the pellet was gently dissolved by pipetting. the solution was spun at 13200 rpm for 2 min. The supernatant containing phage was transferred to a 1.5 ml sterile centrifuge tube labeled BP3-M2 (amplified, purified) and stored at 4°C. BP3-M2 (phage pellet) was kept in O/N at 4°C. 200 µl of glycerol (50% glycerol, total volume 400 µl) was added to 200 µl of BP3-M2 (amplified, purified) solution, the solution was thoroughly mixed using a vortex and stored at -20°C.

190 µl TBS buffer was added to well A1-B1-C1-D1-E1 of the 96-well plate. 180 µl TBS buffer was added to well A2-A9, B2-B9, C2-C12, D2-D12, E2-E12 of the 96-well plate. 10 µl BP3-M1 solution was added to well A1 and 10 µl BP3-M2 solution was added to well B1 of the 96-well plate. solutions were mixed by pipetting up and down for 10 seconds with sterile pipette tips. The 96-well plate was placed on an orbital shaker (lid closed) and shaken at 150 rpm for 2 minutes. 20 µl of the solution mixture was transferred from A1 to A2, and B1 to B2. solutions were mixed by pipetting up and down for 10 seconds with sterile pipette tips. The 96-well plate was placed on an orbital shaker (lid closed) and shaken at 150 rpm for 2 min. These steps were repeated until a solution was transferred to wells A9-B12.

In a 50 ml centrifuge tube, 20 ml of LB broth prepared in advance and stored at room temperature was taken. 20 µl tetracycline (1:1000 ratio) and 100 µl inoculation (1:200 ratio) were added to LB broth. E. coli culture was grown overnight at 37°C at 250 rpm with an orbital shaker. Then, 50 µl tetracycline (1:1000 ratio) was added to the new 50 ml LB broth medium in the 250 ml flask and the E. coli culture was grown by inoculating this Lb medium with 20 ml O/N culture. When the O/N inoculated E. coli culture reached the mid-log phase (OD600: 0.34) (in 3-4 hours). LB Agar/IPTG/X-gal plates were placed at 37°C to warm up (maximum 1 hour). The top Agar medium (100 ml) was melted in the microwave and the flask was placed in a 55°C water bath. 50 ml of the melted Top Agar was divided into a 50 ml sterile falcon tube. 50 µl tetracycline (1:1000) was added to the Top Agar. 3 ml of LB agar was divided into 15 ml falcon tubes (total 6 portions). Falcon tubes containing Top Agar were placed in a 45°C water bath and kept thawed. 180 µl of E. coli culture was mixed with 20 µl of phage from selected wells

(A5-7-9; B10-11-12) in a sterile 1.5 ml sterile centrifuge tube (total 6 plates). E. coli and phage were mixed by pipetting and each mixture (200 µl E. coli/phage) was mixed into 3 ml of molten Top Agar. E. coli and phage mixture was poured onto LB Agar/X-gal/IPTG-tetracycline plates. The plates were kept at room temperature for 5 minutes until the ball agar solidified. The agar plate was inverted and incubated overnight at 37°C (no longer than 18 hours). Blue colonies were counted and the amount of phage in each elution fraction was calculated. 6 µl BP3-M2 phage solutions were taken into Eppendorf tubes. Both samples were measured by nanodrop with 2 technical repetitions and the amount of phage in each elution fraction was calculated.

2.1.4 Biopanning 4

While the precipitation is being prepared, 240 µl HEPES solution (50 mM, pH 7.00), 125 µl KH2PO4 buffer (11.52 mM, pH 7.00), 125µl $CaCl_2.2H_2O$ buffer (19.2 mM, pH 7.00), and 50 µl BP3-M2 Phage (Final Volume: 500 µl; $2x10^{11}$ pfu/ml), respectively, 2 ml mixed in a centrifuge tube. The centrifuge tube was shaken on an orbital shaker for 17 hours at 150 rpm at 25°C. The samples were precipitated for 10 minutes in a centrifuge at 14000 rpm.

The supernatant was transferred to a fresh tube, labeled as BP4-S1, and kept at +4 °C. 500 µl of Wash Buffer I was added to the pellet and the pellet was thawed for 5 minutes at 25°C at 100 rpm on an orbital shaker. the samples were precipitated for 10 minutes in a centrifuge at 14000 rpm. The supernatant was transferred to a fresh tube, labeled as BP4-S2, and kept at +4 °C. 500 µl of Wash Buffer III was added to the pellet and the pellet was thawed at 25°C for 5 minutes on an orbital shaker at 100 rpm. the samples were precipitated for 10 minutes in a centrifuge at 14000 rpm. The supernatant was transferred to a fresh tube, labeled as BP4-S3, and kept at +4 °C.1 ml of Glycine solution (0.2 M pH: 2.17) was added to the pellet to dissolve the precipitate. The pellet was thawed by placing the centrifuge tube in an orbital shaker at 100 rpm for 15 minutes. Then, the solution was neutralized with 160 µl of Trizma Base solution (0.91 M pH: 9.1).

In a 50 ml centrifuge tube, 20 ml of LB broth prepared in advance and stored at room temperature was taken. 20 µl tetracycline (1:1000 ratio) and 100 µl inoculation

(1:200 ratio) were added to LB broth. E. coli culture was grown overnight at 37°C at 250 rpm with an orbital shaker. Then, 50 µl tetracycline (1:1000 ratio) was added to the new 50 ml LB broth medium in the 250 ml flask and the E. coli culture was grown by inoculating this Lb medium with 20 ml O/N culture. When the O/N inoculated E. coli culture reached the early log phase (OD600: 0.01-0.05) (in 1-2 hours), 800 µl Phage was transferred to a 250 ml shake flask (E. coli culture) and 250 ml. It was incubated for 4 hours with shaking at 250 rpm at 37°C. After 4 hours of growth, 50 ml of E. coli/phage culture was transferred to 250 ml Nalgene sterile centrifuge tubes. Nalgene centrifuge tubes were spun at 8000 rpm for 20 minutes and E. coli was precipitated. The supernatant containing phage was transferred to a sterile 250 ml Nalgene centrifuge tube. 8.3 ml of PEG/NaCl solution was added to ~50 ml of supernatant (1:6; v/v), mixed thoroughly on the vortex and left at O/N at 4°C. The centrifuge temperature was adjusted to 4°C. The PEG-treated E. coli/phage culture stored o/n 4°C was spun at 8000 rpm for 20 min. The phage pellet was obtained at the bottom of a 250 ml Nalgene centrifuge tube. The supernatant containing the E. coli was transferred to a 50 ml sterile centrifuge tube labeled BP4-S4(amplified) and stored at 4°C. The phage pellet was resuspended with 5 ml TBS buffer, thawed by pipetting and vortexing, and transferred to a 50 ml sterile centrifuge tube, centrifuged at 8000 rpm for 10 min. The supernatant containing phage was transferred to a sterile 50 ml Nalgene centrifuge tube. 830 µl of PEG/NaCl solution was added to ~ 5 ml of supernatant (1:6; v/v), mixed thoroughly, and left on ice for 2 hours for phage precipitation. It was spun at 10000 rpm for 10 min to obtain precipitated phages. The supernatant containing E. coli was collected in a 15 ml sterile centrifuge tube labeled BP4-S5 (amplified) and stored at 4°C. The phage pellet was resuspended in 1 ml TBS buffer and dissolved by shaking. The solution was transferred to a 1.5 ml sterile centrifuge tube and spun at 10000 rpm for 10 min. The phage-containing Supernatant was transferred to a 1.5 ml sterile centrifuge tube and spun at 13200 rpm for 3 minutes. The supernatant containing E. coli was removed into a 1.5 ml sterile centrifuge tube labeled BP4-S6 (amplified), and stored at 4°C. The phage pellet was resuspended with 200 µl TBS buffer and the pellet was gently dissolved by pipetting. the solution was spun at 13200 rpm for 2 min. The supernatant containing phage was transferred to a 1.5 ml sterile centrifuge tube labeled BP4-M2 (amplified, purified) and stored at 4°C. BP4-M2 (phage pellet) was kept in O/N at 4°C. 200 µl of glycerol (50% glycerol, total volume 400 µl) was added to 200 µl of BP4-M2 (amplified, purified) solution, the solution was mixed thoroughly with a vortex and stored at -20°C.

90 µl TBS buffer was added to well A1-B1-C1-D1-E1 of the 96-well plate. 180 µl TBS buffer was added to wells A2-A9, and B2-B12 of the 96-well plate. 10 µl BP4-M1 solution was added to well A1, 10 µl BP4-M2 solution was added to well B1 of the 96-well plate. solutions were mixed by pipetting up and down for 10 seconds with sterile pipette tips. The 96-well plate was placed on an orbital shaker (lid closed) and shaken at 150 rpm for 2 minutes. 20 µl of the solution mixture was transferred from A1 to A2, and B1 to B2. solutions were mixed by pipetting up and down for 10 seconds with sterile pipette tips. The 96-well plate was placed on an orbital shaker (lid closed) and shaken at 150 rpm for 2 min. These steps were repeated until a solution was transferred to wells A9-B12.

In a 50 ml centrifuge tube, 20 ml of LB broth prepared in advance and stored at room temperature was taken. 20 µl tetracycline (1:1000 ratio) and 100 µl inoculation (1:200 ratio) were added to LB broth. E. coli culture was grown overnight at 37C at 250 rpm with an orbital shaker. Then, 50 µl tetracycline (1:1000 ratio) was added to the new 50 ml LB broth medium in the 250ml flask and the E. coli culture was grown by inoculating this Lb medium with 20 ml O/N culture. When the O/N inoculated E. coli culture reached the mid-log phase (OD600: 0.34) (in 3-4 hours). LB Agar/IPTG/X-gal plates were placed at 37°C for warming up (not more than 1 hour). The top Agar medium (100 ml) was melted in the microwave and the flask was placed in a 55°C water bath. 50 ml of the melted Top Agar was divided into a 50 ml sterile falcon tube. 50 µl tetracycline (1:1000) was added to the Top Agar. 3 ml of LB agar was divided into 15 ml falcon tubes (total 6 portions). Falcon tubes containing Top Agar were placed in a 45°C water bath to be kept in the molten state. 180 µl of E. coli culture was mixed with 20 µl of phage from selected wells (A5-7-9, B10-11-12) in a sterile 1.5 ml sterile centrifuge tube (6 plates in total). E. coli and phage were mixed by pipetting and each mixture (200 µl E. coli/phage) was mixed into 3 ml of molten Top Agar. E. coli and phage mixture ball agar was poured onto LB Agar/X-gal/IPTG-tetracycline plates. The plates were kept at room temperature for 5 minutes until the ball agar solidified. The agar plate was inverted and incubated overnight at 37°C (no longer than 18 hours). Blue colonies were counted and the amount of phage in each elution fraction was calculated. 6 µl BP4-M2 phage solutions were taken into eppendorf tubes. Both samples were measured by nanodrop with 2 technical repetitions and the amount of phage in each elution fraction was calculated.

2.3 Selection of Functional Peptides Eliminated from BP4

2.3.1 Selection of Phage Colonies Carrying Functional Peptides

90 µl TBS buffer was added to well A1-B1-C1 of the 96-well plate. 180 µl TBS buffer was added to well A2-A9, B2-B9, C2-C9 of the 96-well plate. 5 µl BP1-M2 phage solution was added to well A1, 5 µl BP2-M2 solution was added to well B1, 5 µl BP4-M2 solution was added to well C1 of the 96-well plate. Solutions were mixed by pipetting up and down for 10 seconds with sterile pipette tips. The 96-well plate was placed on an orbital shaker (lid closed) and shaken at 150 rpm for 2 minutes. 20 µl of solution mixture was transferred from A1 to A2; B1 to B2; C1 to C2. solutions were mixed by pipetting up and down with sterile pipette tips for 10 seconds. The 96-well plate was placed on an orbital shaker (lid closed) and shaken at 150 rpm for 2 min. These steps were repeated until a solution was transferred to wells A9-B9-C9.

In a 50 ml centrifuge tube, 20 ml of LB broth prepared in advance and stored at room temperature was taken. 20 µl tetracycline (1:1000 ratio) and 100 µl inoculation (1:200 ratio) were added to LB broth. E. coli culture was grown overnight at 37C at 250 rpm with an orbital shaker. Then, 50 µl tetracycline (1:1000 ratio) was added to the new 50 ml LB broth medium in the 250ml flask and the E. coli culture was grown by inoculating this Lb medium with 20 ml O/N culture. When the O/N inoculated E. coli culture reached the mid-log phase (OD600: 0.34) (in 3-4 hours). Large LB Agar/IPTG/X-gal plates were placed at 37°C for warming (no more than 1 hour). The top Agar medium (100 ml) was melted in the microwave and the flask was placed in a 55°C water bath. 50 ml of the melted Top Agar was divided into a 50 ml sterile falcon tube. 50 µl tetracycline (1:1000) was added to the Top Agar. 6 ml of LB agar was divided into 15 ml falcon tubes (16 portions in total). Falcon tubes containing Top Agar were placed in a 45°C water bath to keep them in the molten state. 180 µl of E. coli culture was mixed with 20 µl of phage from selected wells (A9; B9, C9, D9) in a sterile 1.5 ml sterile centrifuge tube (total 15 plates, each biopanning). The E. coli and phage were mixed by pipetting and each mixture (200 µl E. coli/phage) was mixed into 6 ml of molten Top Agar. The E. coli and phage mixture was poured onto the LB Agar/X-gal/IPTG-tetracycline plates. The plates were

kept at room temperature for 10 minutes until the ball agar solidified. The agar plate was inverted and incubated overnight at 37°C (no longer than 18 hours).

150 µl of PC buffer containing 0.02% detergent was taken into 230 1.5ml pre-autoclaved sterile DNAse free Eppendorf tubes. From the inoculated Petri dishes, 80 blue colonies for BP4-M2 were scraped off with a sterile pipette tip and transferred into 150 µl of PC buffer containing 0.02% detergent. All eppendorf tubes were shaken for 15 min at room temperature on a shaker (Hangzhou Miu, GS-20, Orbital Shaker). Incubated in a hot water bath (Nuve, NB 20, Water Bath) preheated to 60°C for 45 min. They were stored overnight at +4°C. 230 new 1.5ml pre-autoclaved sterile DNAse free Eppendorf tubes were filled with 150 µl sterile glycerol. PC buffers containing the colony were added to the glycerol and mixed thoroughly with a vortex. The tubes were labeled with biopanning code and colony number. All glycerol colony stocks were stored at -20°C.

2.3.2 DNA Isolation and Sequencing of Functional Peptides

2.3.2.1 DNA Isolation

In a 50 ml centrifuge tube, 20 ml of LB broth prepared in advance and stored at room temperature was taken. 20 µl tetracycline (1:1000 ratio) and 100 µl inoculation (1:200 ratio) were added to LB broth. E. coli culture was grown overnight at 37C at 250 rpm with an orbital shaker. Then, 350 µl tetracycline (1:1000 ratio) was added to the new 50 ml LB broth medium in the 250ml flask and the E. coli culture was grown by inoculating this Lb medium with 20 ml O/N culture. When the O/N inoculated E. coli culture reached the early-log phase (OD600: 0.01-0.05) (in 1.45-2 hours). Early log phase LB broth was taken 3ml into 15 ml falcon tubes. To each 3ml of LB broth, 10 µl of glycerol clone phage stocks were added. The E. coli/phage culture was grown until it reached the mid-log phase (OD600: 0.34) (3-4 hours). 3ml of bacterial cultures were transferred into a 1.5ml pre-autoclaved sterile DNAse-free Eppendorf tube and spun at 5000 rpm for 15 minutes at room temperature (15-25°C). The 1.4ml supernatant containing M13 bacteriophage was carefully transferred to a new reaction tube without

missing the pellet. 14 µl of Buffer MP (1/100) was added for M13 precipitation. Vortexed, mixed, and incubated at room temperature for at least 2 minutes. 0.7 ml of sample was transferred to a QIAprep spin column placed in a 2 ml microcentrifuge tube. The loading and centrifugation (steps 6 and 7) were repeated until the entire sample was loaded onto the QIAprep spin column. 0.7 ml of Buffer PB was added to the QIAprep spin column and centrifuged at 8000 rpm for 15 seconds. 0.7 ml of Buffer PB was added to the QIAprep spin column and incubated at room temperature for 1 min. Centrifuged at 8000 rpm for 15 seconds. 0.7 ml of Buffer PE was added to the QIAprep spin column and centrifuged at 8000 rpm for 15 seconds. The QIAprep spin column was centrifuged blank at 8000 rpm for 15 seconds to remove the buffer PE from the collection tube. The QIAprep spin column was placed in a clean 1.5 ml microcentrifuge tube. To elute DNA, 100 µl of Buffer EB (10 mM Tris-Cl, pH 8.5) was added to the center of the column membrane, incubated at room temperature for 10 minutes, and centrifuged at 8000 rpm for 30 seconds. Tubes were labeled with biopanning code and colony number. All colony DNA stocks were stored at -20°C. For the calculation of the concentration of all colony DNA, 6 µl was taken into new eppendorf tubes. Both samples were subjected to 2 technical repetitive nanodrop measurements and the amount of DNA in each elution fraction, the 260/280 nm value, and the 260/230 nm values were calculated.

2.3.2.2 Spin Colon Prep and Cleaning for Sequencing

Weighed 1 g SephadexG50 and added Sephadex to the Falcon tube. 15 ml of autoclaved ultra-pure water was added to the Sephadex. The Falcon tube was shaken vigorously for 1-2 minutes and allowed to rest for 5-10 minutes at room temperature. Spin columns were labeled with sample names. 650 µl of sphadex mixture was added to each column. The tubes were allowed to stand for 10-30 min until phage dissociation appeared and centrifuged at 5400 rpm for 2 min. Water was removed from the collection tube and labeled. The top was replaced with a new eppendorf as a clean elution tube with the Sephadex column inside intact. PCR products (at least 10 µl) were pipetted onto the top of the sphadex column. Tubes were centrifuged at 5400 rpm for 2 min to collect clean PCR products

2.3.2.3 Polymerase Chain Reaction (PCR)

Eppendorf tubes were prepared for 37 isolated clone DNAs to be sequenced. 1ul BigDye 3.1 RRM, 1.5ul 5X buffer, 1.6 -96 gIII Primer (96 gIII sequencing primer 5′-HOCCC TCA TAG TTA GCG TAA CG –3′, 100 pmol, 1 pmol/µl) were added to each tube respectively. 5.9ul template DNA/water was added to the tube so that the total volume of the PCR mixture was 10ul. The templated DNA/water ratio was adjusted so that the final concentration of DNA samples whose concentration was predetermined by nono-drop was at least 20 ng. PCR steps are shown in Table 1.1. The PCR reaction was performed using Real-Time PCR (ROCHE LC480). After the end of the PCR program, the block was left at room temperature until these products were ready for purification. if the reaction clean-up was to be performed the next day, the samples would be stored at -20˚C.

Table 2.1. PCR steps of obtaining full-length DNA segment

	Temperature	Time	Cycles
Initial Denaturation	96 ˚C	1 min	1
Denaturation	96 ˚C	10 sec	25
Annealing	50 ˚C	5 sec	
Extension	60 ˚C	4 min	
Hold	4 ˚C	5 min	1

2.3.2.4 Cycle Sequencing Reaction Clean-Up Methods and DNA Sequencing

A premix solution was prepared with 66 µl NaOAc (3M, pH 5.6), 160 µl H_2O, and 1600 µl 100% EtOH. 10 µl of sequencing reaction was added to each well of the 96-well plate. 22 µl of premix solution was added to each 10 µl of sequencing reaction. The wells were carefully vortexed to prevent the contents of the wells from splashing each other. Allowed to stand at room temperature for 15 minutes. Samples were spun at 5760 x g for

20-30 min (CGC-SIGMA plate centrifuge). A folded paper towel was placed on the plate to drain the contents and the plate was inverted upside down. 125 µl of 70% EtOH was added to each well and the sealed plate was gently inverted and mixed. The sealing film from the loop sequence reaction was reused as a cover. The plate was rotated at full speed (right side up) for 10 min. 70% ethanol was poured and then the plate was inverted on a folded paper towel and rotated briefly. A hold setting was used for the spin time. The speed was allowed to reach 600 x g, and then the centrifugation was stopped. If reactions were not to be loaded into the sequencer immediately, the reactions were stored as dry pellets in the freezer. Samples were resuspended in formamide immediately before loading into the sequencer. Sequencing Instrument (Applied Biosystems 3130xl Genetic Analyzer) was used for sequencing of DNA sequences. The sequences were analyzed using FinchTV, Justbio, and Expasy software for fragment analysis and sequence comparison. From these analyzed DNA sequences, error-free, and different sequences were selected for purification. Table 2.2 shows the purity and concentration of DNA sequences isolated from the clones.

Table 2.2 The purified DNA sequences

Sample ID	260/280	260/230	Concentration (ng/ µl)
BP4-M2-Clone 1	2,04	1,93	35,74
BP4-M2-Clone 3	1,95	1,92	38,97
BP4-M2-Clone 4	1,99	2,11	22,62
BP4-M2-Clone 5	1,95	1,95	31,08
BP4-M2-Clone 6	2,03	2,36	33,16
BP4-M2-Clone 7	2,12	2,48	29,95
BP4-M2-Clone 8	1,99	2,09	29,71
BP4-M2-Clone 9	1,95	1,95	26,95
BP4-M2-Clone 10	2,02	2,42	25,46
BP4-M2-Clone 11	1,96	2,12	39,06
BP4-M2-Clone 12	1,72	2,42	31,43
BP4-M2-Clone 13	2,11	0,37	17,3
BP4-M2-Clone 14	1,97	0,59	37,82
BP4-M2-Clone 15	1,97	0,42	23,97
BP4-M2-Clone 16	1,85	0,79	27,42
BP4-M2-Clone 17	1,84	0,54	21,22
BP4-M2-Clone 18	1,93	0,72	25,42
BP4-M2-Clone 19	1,84	2,95	23
BP4-M2-Clone 20	2,02	2,33	13,32
BP4-M2-Clone 21	1,97	3,12	19,63

2.3.3 Purification of Single Colony Selected via Biopanning Rounds

In a 50 ml flask, 20 ml of LB broth prepared in advance and stored at room temperature was taken. 20 µl tetracycline (1:1000 ratio) and 100 µl inoculation (1:200 ratio) were added to LB broth. E. coli culture was grown overnight at 37°C at 250 rpm with an orbital shaker. Then 20 µl tetracycline (1:1000 ratio) and 100 µl O/N E. coli culture (1:200 ratio) were added to a new 20 ml LB broth medium in a 250- or 50-ml flask. E. coli culture was inoculated and grown. When the O/N inoculated E. coli culture reached the early log phase (OD600: 0.01-0.05) (within 1-2 hours), 5 µl Phage was transferred to 20 ml E. coli culture and incubated at 37°C for 4 hours with shaking at 250 rpm. After 4 hours of growth, 20 ml of E. coli/phage culture was transferred to 50 ml Nalgene sterile centrifuge tubes. Nalgene centrifuge tubes were spun at 8000 rpm for 20 minutes and E. coli was precipitated. The supernatant containing phage was transferred to a sterile 50 ml Nalgene centrifuge tube. 3.33 ml of PEG/NaCl solution was added to ~20 ml of supernatant (1:6; v/v), mixed thoroughly on the vortex and left at O/N at 4°C. The centrifuge temperature was adjusted to 4°C. The PEG-treated E. coli/phage culture stored o/n 4°C was spun at 8000 rpm for 20 min. The phage pellet was obtained at the bottom of a 50 ml Nalgene centrifuge tube. The supernatant containing the E. coli was transferred to a 50 ml sterile centrifuge tube labeled BP4-Clone Code-S1 (amplified) and stored at 4°C. The phage pellet was resuspended with 5 ml TBS buffer, thawed by pipetting and vortexing, and transferred to a 50 ml sterile centrifuge tube, centrifuged at 8000 rpm for 10 min. The supernatant containing phage was transferred to a sterile 50 ml Nalgene centrifuge tube. 833 µl of PEG/NaCl solution was added to ~ 5 ml of supernatant (1:6; v/v), mixed thoroughly, and left on ice for 2 hours for phage precipitation. It was spun at 10000 rpm for 10 min to obtain precipitated phages. The supernatant containing E. coli was collected in a 15 ml sterile centrifuge tube labeled BP4-Clone Code-S2 (amplified) and stored at 4°C. The phage pellet was resuspended in 1 ml TBS buffer and dissolved by shaking. The solution was transferred to a 1.5 ml sterile centrifuge tube and spun at 10000 rpm for 10 min. The phage-containing Supernatant was transferred to a 1.5 ml sterile centrifuge tube and 166 µl of PEG/NaCl solution was added to ~ 1 ml of supernatant (1:6; v/v), vortex 5 seconds, and left on ice for 10 minutes for phage precipitation. It was spun at 13200 rpm for 3 minutes. The supernatant containing E. coli

was removed into a 1.5 ml sterile centrifuge tube labeled BP4-Clone Code-S3 (amplified), and stored at 4°C. The phage pellet was resuspended with 200 µl TBS buffer and the pellet was gently dissolved by pipetting. The solution was spun at 13200 rpm for 2 min. The supernatant containing phage was transferred to a 1.5 ml sterile centrifuge tube labeled BP4-Clone Code_Purified and stored at 4°C. BP4-Clone Code_Purified (phage pellet) was kept in O/N at 4°C. 200 µl of glycerol (50% glycerol, total volume 400 µl) was added to 200 µl of BP4-Clone Code_Purified solution, the solution was mixed thoroughly with a vortex and stored at -20°C.

95 µl TBS buffer was added to well A1 of the 96-well plate. 180 µl TBS buffer was added to well A2-A12 of the 96-well plate. 5 µl BP4-Clone Code-Purified phage solution was added to well A1 of the 96-well plate. solutions were mixed by pipetting up and down for 10 seconds with sterile pipette tips. The 96-well plate was placed on an orbital shaker (lid closed) and shaken at 150 rpm for 2 minutes. 20 µl of the solution mixture was transferred from A1 to A2. solutions were mixed by pipetting up and down for 10 seconds with sterile pipette tips. The 96-well plate was placed on an orbital shaker (lid closed) and shaken at 150 rpm for 2 min. These steps were repeated until a solution was transferred to wells A12.

In a 50 ml centrifuge tube, 20 ml of LB broth prepared in advance and stored at room temperature was taken. 20 µl tetracycline (1:1000 ratio) and 100 µl inoculation (1:200 ratio) were added to LB broth. E. coli culture was grown overnight at 37C at 250 rpm with an orbital shaker. Then 20 µl tetracycline (1:1000 ratio) and 100 µl O/N E. coli culture (1:200 ratio) were added to a new 20 ml LB broth medium in a 250- or 50-ml flask. When the O/N inoculated E. coli culture reached the mid-log phase (OD600: 0.34) (in 3-4 hours). LB Agar/IPTG/X-gal plates were placed at 37°C for warming up (not more than 1 hour). 50 ml of the melted Top Agar was divided into a falcon tube. 50 µl tetracycline (1:1000) was added to the Top Agar. 3 ml of LB agar was divided into falcon tubes. Falcon tubes containing Top Agar were placed in a 45°C water bath to be kept in the molten state. 180 µl of E. coli culture was mixed with 20 µl of phage from selected wells (A10 -11-12) in a sterile centrifuge tube. E. coli and phage were mixed by pipetting and each mixture was mixed into 3 ml of molten Top Agar. E. coli and phage mixture ball agar was poured onto LB Agar/X-gal/IPTG-tetracycline plates. The plates were kept at room temperature for 5 minutes until the ball agar solidified. The agar plate was inverted and incubated overnight at 37°C (no longer than 18 hours). Blue colonies were counted and the amount of phage in each elution fraction was calculated. Both samples were

measured by nanodrop and the amount of phage in each elution fraction was calculated. Purification steps were repeated for all selected clones.

$$of\ plagues\ x\ dilution\ x\ volume\ x\ \mu l\ conversion = \frac{pfu}{ml} \qquad (2.1)$$

2.4 Mineralization Kinetics of Mineralizing Peptides

For each colony (#1-31), mineralization reactions (pH 7.0 at 25°C) are initiated with a concentration of 10^{11} pfu. These reactions include 55 µl CaCl2.2H2O buffer (19.2 mM, pH 7.00), 55 µl KH2PO4 buffer (11.52 mM, pH 7.00), and 90 µl HEPES solution (50 mM, pH 7.00 (Final Volume and Concentration: 200 µl; 1x1011 pfu/ml; Ca/P: 5.28/3.17 (1.1X) mM). The results of the colony mineralization reactions were initiated together with positive (Ca/P: 6.4/3.84 (1.33X) Mm; Ca/P: 5.76/3.46 (1.2X) Mm) control group reactions and negative (Ca/P: 4.8/2.88 (1X) Mm; Ca/P: 3.84/2.3 (0.8X) Mm) control group reactions to support. The amount of each colony used for the mineralization reaction is listed in Table. Mineralization reaction solutions were mixed in well plates respectively. Mineralization kinetics were measured by spectrophotometer at 820 nm at 25°C for 7 hours. The experiment was repeated 3 times.

2.5 Characterization of Mineralizing Peptides

2.5.1 SEM Analysis

For SEM analysis, mineralization reactions (pH 7.0 at 25°C) for each peptide (1-14-21-30) were initiated with 10^{11} pfu in 500 µl (Final Concentration: $1x10^{11}$ pfu/ml; Ca^{2+}/PO_4^{3-}: 5.28/3.17 mM) utilizing positive (Ca^{2+}/PO_4^{3-}: 6.4/3.84 mM (1.33X);

Ca^{2+}/PO_4^{3-}: 5.76/3.46 mM (1.2X)) control group reactions and negative (Ca^{2+}/PO_4^{3-}: 4.8/2.88 mM (1X); Ca^{2+}/PO_4^{3-}: 3.84/2.3 mM (0.8X)) control group reactions. The amount of each colony used for the mineralization reaction is listed in Table 3.2. The reaction tubes were placed in a shaking incubator for 1-6 hours at a speed of 150 rpm at 25°C. Mineralization was checked hourly. Mineralized colony tubes were removed from the incubator and stored at +4 until centrifugation. After the reaction, the samples were collected in 2ml tubes and centrifuged at 14,000 rpm for 5 min. Supernatants were taken into new 2ml tubes. The mineral pellet formed by the colonies was stored at -80 C overnight. The frozen samples were then dried in a lyophilized (FreeZone Freeze Dry Systems) at 0.04mbar vacuum and -51ºC for 24 hours. Before imaging, the samples were fractured to reveal the cross-section of the mineral layer and coated with Au to ensure electron conductivity. A scanning electron microscope (SEM; FEI QuantaTM 250 FEG SEM) was used for surface topography and cross-sectional structure characterization using secondary electron imaging mode. The SEM was operated at an accelerating voltage of 10 kV to reduce possible e-beam radiation damage.

2.5.2 XRD Analysis

For XRD analysis, mineralization reactions (pH 7.0 at 25°C) for each colony (#1-23) were initiated with 10^{11} pfu in 500 µl (Final Concentration: $1x10^{11}$ pfu/ml; Ca/P: Ca/P: 5.28/3.17 mM) utilizing positive (Ca^{2+}/PO_4^{3-}: 6.4/3.84 mM (1.33X); Ca^{2+}/PO_4^{3-}: 5.76/3.46 mM (1.2X)) control group reactions and negative (Ca^{2+}/PO_4^{3-}: 4.8/2.88 mM (1X); Ca^{2+}/PO_4^{3-}: 3.84/2.3 mM (0.8X)) control group reactions. Mineralization reactions for each colony were initiated in 7 tube sets (total volume 3.5 ml). The amount of each colony used for the mineralization reaction is listed in Table 3.2. The reaction tubes were placed in a shaking incubator for 1-6 hours at a speed of 150 rpm at 25°C. Mineralization was checked hourly. Mineralized colony tubes were removed from the incubator and stored at +4 until centrifugation. After the reaction, the samples were collected in an eppendorf tube and centrifuged at 14,000 rpm for 5 min. Supernatants were taken into new eppendorf tubes. The mineral pellet formed by the colonies was stored at -80 C overnight. The frozen samples were then dried in a lyophilized (FreeZone Freeze Dry

Systems) at 0.04mbar vacuum and -51ºC for 24 hours. Detailed information about the crystallographic structure, chemical composition, and physical properties of the material was obtained by X-ray diffraction (XRD; Philips X'Pert Pro) analysis. XRD patterns were recorded at 25 °C in the range from 10 to 80˚ 2Θ with a resolution of 0.1˚. The patterns obtained were compared with International Centre for Diffraction Data (ICDD, formerly JCPDS) files.

2.5.3 FTIR Analysis

For FT-IR analysis, mineralization reactions (pH 7.0 at 25°C) for each colony (#1-30) were initiated with 10^{11} pfu in 500 µl (Final Concentration: $1x10^{11}$ pfu/ml; Ca/P: Ca/P: 5.28/3.17 mM) utilizing positive (Ca^{2+}/PO_4^{3-}: 6.4/3.84 mM (1.33X); Ca^{2+}/PO_4^{3-}: 5.76/3.46 mM (1.2X)) control group reactions and negative (Ca^{2+}/PO_4^{3-}: 4.8/2.88 mM (1X); Ca^{2+}/PO_4^{3-}: 3.84/2.3 mM (0.8X)) control group reactions. Mineralization reactions for each colony were initiated in 4 tube sets (total volume 2 ml). The amount of each colony used for the mineralization reaction is listed in Table 3.2. The reaction tubes were placed in a shaking incubator for 1-6 hours at a speed of 150 rpm at 25°C. Mineralization was checked hourly. Mineralized colony tubes were removed from the incubator and stored at +4 until centrifugation. After the reaction, the samples were collected in a 2ml tube and centrifuged at 14,000 rpm for 5 min. Supernatants were taken into new 2ml tubes. The mineral pellet formed by the colonies was stored at -80 C overnight. The frozen samples were then dried in a lyophilized (FreeZone Freeze Dry Systems) at 0.04mbar vacuum and -51ºC for 24 hours. FT-IR analysis was performed using a PerkinElmer UATR Two-FT-IR Spectrometer. The frequency range was computed between 4000-400 cm-1 and spectra were collected at 1 cm-1 resolution over 20 scans.

CHAPTER 3

RESULTS AND DISCUSSION

3.1 Optimizing the Selective Pressure for Identifying Mineralizing Peptides

The Ca^{2+}/ $P0_4^{3-}$ precipitation reactions in HEPES and Tris buffers were monitored by measuring absorbance values at 820 nm in a 96-well plate format; here the effects of physicochemical properties pH, temperature, and molarity parameters on Ca^{2+} and PO_4^{3-} mineralization precipitate formation were tested.

Table 3.1. Optimization parameters of selective pressure for the determination of mineralizing peptides

	25°C		37°C	
BUFFER	Ca^{2+}/ PO_4^{3-}	pH	Ca^{2+}/ PO_4^{3-}	pH
HEPES	4.8/2.88 mM	6.6-7.8	4.8/2.88 mM	6.6-7.4
	3.16/1.9 mM	6.6-7.8	3.16/1.9 mM	6.6-7.6
	2.4/1.44 mM	6.6-7.8	2.4/1.44 mM	6.6-7.8
TRIS	4.8/2.88 mM	6.6-7.8	4.8/2.88 mM	6.6-7.4
	3.16/1.9 mM	6.6-	3.16/1.9 mM	6.6-7.4
	2.4/1.44 mM	6.6-	2.4/1.44 mM	6.6-7.6

The main conditions affecting the precipitation, chemical composition, and crystal structure of calcium phosphate are physicochemical: pH, temperature, phosphate and calcium concentrations, and ionic strength (Mekmene, et al, 2009). Optimization is to consider the effects of these parameters on calcium phosphate precipitation and select the optimum condition, but it is complicated to select the optimum condition because the parameters are interrelated.

In the first experiment, Ca^{2+}/PO_4^{3-} ratios were kept constant at 1.66 for all test sets. Ca/P=1.66 is the stoichiometric HAP $Ca_{10}(PO_4)_6(OH)_2$ value (Raynaud, et al. 2002). In previous studies, mineralization nucleation performance was proven when the Ca^{2+}/PO_4^{3-} ratio was kept at 4.8/2.88 mM (1X) (Dogan et al. 2018). The first conclusion from the results of this experiment is that, at a constant Ca^{2+}/PO_4^{3-} ratio, mineral analysis shows that changing pH (final pH values were between 6.6 and 7.8) has a significant effect on the amounts of precipitated calcium and phosphate. (Fig 3.1). One of the most powerful and effective ways to trigger Ca^{2+}/PO_4^{3-}crystallization is pH Without any precipitants, only small changes in pH can be highly effective on mineralization (McPherson, 1995). In the process of precipitation and crystal growth, pH affects both the solution and the mineral surface (Mekmene et al, 2009).

A healthy intraoral pH is physiologically maintained in the range of pH 6.8-7.8. (Loke, et al. 2016). For this reason, mineralization kinetics were studied with $CaCl_2.2H_2O$ and KH_2PO_4 solutions prepared in the pH 6.6 - pH 7.8 range. Using a suitable buffer, the pH of the solution can be adjusted, maintained, and changed in the liquid phase by equilibration. Specific buffer matrices at different pH values are commercially available to researchers (Slice pH; Hampton Research, Aliso Viejo, California, USA) (McPherson, and Cudney, 2014). The buffers included in this array are presented in Table 3.2. Considering the pH values of the intraoral environment, it was decided that the most appropriate buffers were HEPES and Tris buffers. These 2 buffers were preferred for preparing $CaCl_2.2H_2O$ and KH_2PO_4 solutions.

Table 3.2. Specific buffer matrices - Slice buffer matrix

Buffer	pH Range	Buffer	pH Range
Citric acid	pH 3.5–4.4	HEPES sodium	pH 6.6–7.5
Sodium citrate tribasic dehydrate	pH 3.6–4.5	HEPES	pH 6.8–7.7
Sodium acetate trihydrate	pH 3.7–4.9	Tris hydrochloride	pH 7.2–8.1
Dl-Mali	pH 4.7–5.9	Tris	pH 7.3–8.5
Succinic acid	pH 4.8–6.0	Tricine	pH 7.4–8.6
Sodium cacodylate trihydrate	pH 5.2 – 6.4	Bicine	pH 7.5–8.7
MES monohydrate	pH 5.3–6.5	Glycine	pH 8.6–9.5
MOPS	pH 6.5–7.7	AMPS	pH 8.7–9.6

3.1.1 Optimization of Ca/P Precipitation in HEPES Buffer with pH, Temperature, and Ionic Concentration

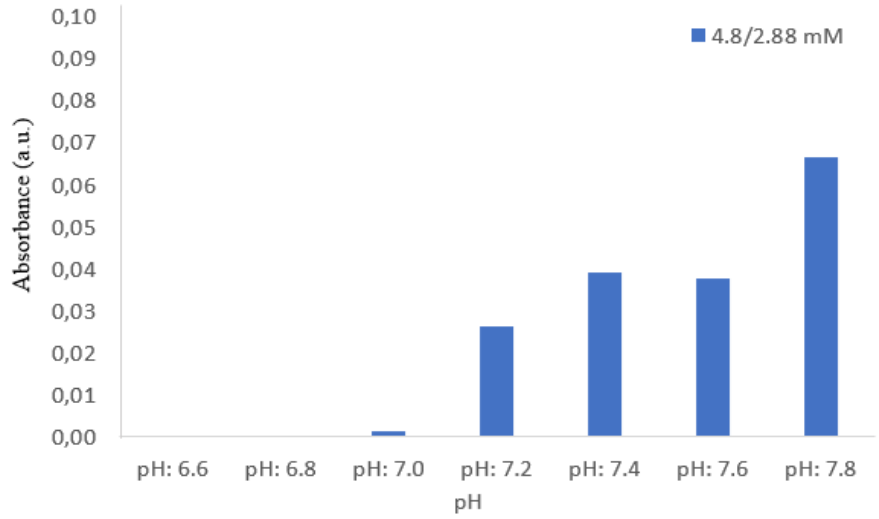

Figure 3.1. Ca^{2+}/PO_4^{3-} nucleation kinetics spectrum at different pH values (pH values between 6.6 and 7.8) and 25 °C in HEPES buffer (Ca^{2+}/PO_4^{3-} ratios: 4.8/2.88 Mm)

The solutions were repeated without changing the parameters (pH: 6.6 to 7.8 and Ca^{2+}/ PO_4^{3-} molarity ratios: 4.18/2.88 mM), and the study was repeated only by increasing the temperature to 37 °C. In this study, the solutions prepared at 25 °C were heated to 37 °C, and the effect of temperature change on the HEPES buffer was controlled. The pH changes in all solutions decreased by 0.13(+_0.01) on average. Therefore, the pH values in the study were assumed to be about 0.13 less with this treatment and evaluated accordingly. Figure 3.2 shows the absorbance values of Ca^{2+}/ PO_4^{3-} precipitates realized under these conditions. It seems that Ca^{2+}/ PO_4^{3-} precipitates are formed at pH 7.2 and 7.4 when the amounts of Ca^{2+} and PO_4^{3-} in the total solution are 50%. When Figure 3.1 and Figure 3.2 are compared with each other, it is concluded that the temperature increase does not change the jump pH values, which is the formation point of Ca^{2+}/ PO_4^{3-} precipitate, while the amount of Ca^{2+}/ PO_4^{3-} precipitate decreases in the reference of absorbance values.

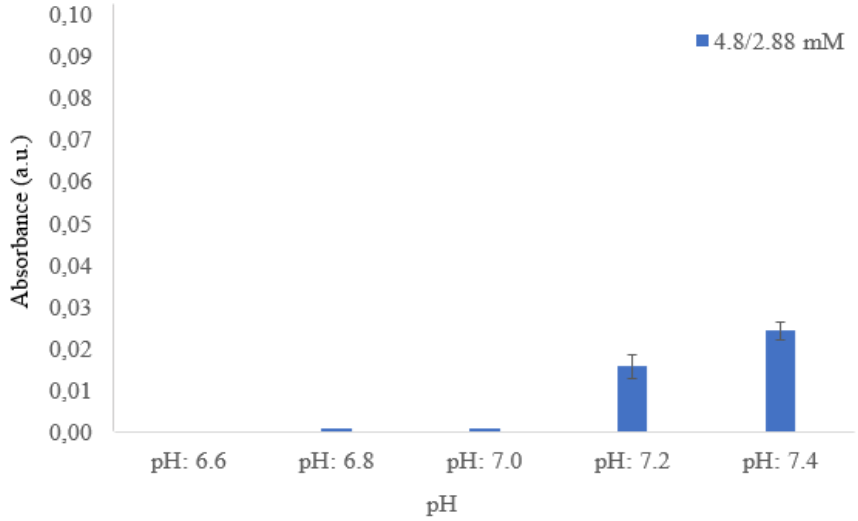

Figure 3.2. Ca^{2+}/PO_4^{3-} nucleation kinetics spectrum at different pH values (pH values between 6.6 and 7.8) and 37 °C in HEPES buffer (Ca^{2+}/PO_4^{3-} ratios: 4.8/2.88 mM)

These results show that Ca^{2+} and PO_4^{3-} solutions prepared in HEPES buffer have a positive effect on Ca^{2+}/ PO_4^{3-} mineralization with increasing pH values. In addition, an increase in temperature has a negative effect on these results, but this effect is only on the amount of Ca^{2+}/ PO_4^{3-} precipitate and this effect is negligible. This is evidenced by the fact that there is no change in the pH value of the cratering point Ca^{2+}/ PO_4^{3-} precipitate formation (Figure 3.5 shows this result). Therefore, the result of the positive effect on the formation of Ca^{2+}/ PO_4^{3-} mineralization with increasing pH values gives meaning to the conclusion that the decrease in pH value with increasing temperature reduces the amount of Ca^{2+}/ PO_4^{3-} precipitate. Detailed absorbance graphs of these graphs (Figure 3.1., and Figure 3.2.) are available in APPENDIX A.

3.1.2 Optimization of Ca/P Precipitation in Tris Buffer with pH, Temperature, and Ionic Concentration

When Figure 3.4 and Figure 3.5 are analyzed in themselves, it is seen that the absorbance values of Ca^{2+}/ PO_4^{3-} precipitates increase continuously as the pH values

increase. This leads to the conclusion that pH increase has a positive effect on Ca^{2+}/ PO_4^{3-} mineralization. Again, when Figure 3.4 and Figure 3.5 5 are analyzed, it is seen that when 50% of the solution consists of Ca^{2+} ions and 50% of PO_4^{3-} ions, the Ca^{2+}/ PO_4^{3-} precipitate formed is quite high at an acceptable rate.

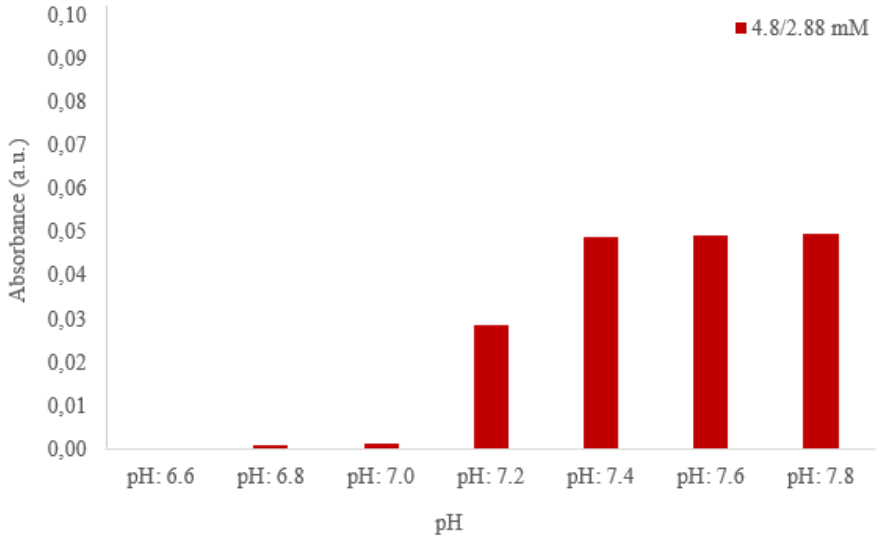

Figure 3.3. Ca^{2+}/PO_4^{3-}nucleation kinetics spectrum at different pH values (pH values between 6.6 and 7.8) and 25 °C in Tris buffer (Ca^{2+}/PO_4^{3-} ratios: 4.8/2.88 mM)

The study was repeated without changing the solution parameters (pH: 6.6 to 7.8 and Ca^{2+}/ PO_4^{3-} molarity ratios: 4.18/2.88 Mm), only increasing the temperature to 37 °C. In this study, solutions prepared at 25 °C were heated to 37 °C to check the effect of temperature change on Tris buffer. The pH change in all solutions decreased by 0.32(+_0.01) on average. Therefore, it is not appropriate to use the same solutions by heating as the rate of change of the pH values in the study would change the pH range of the study. Therefore, the solutions were prepared again by adjusting the pH at 37°C and these solutions were used for the 37°C experiments.

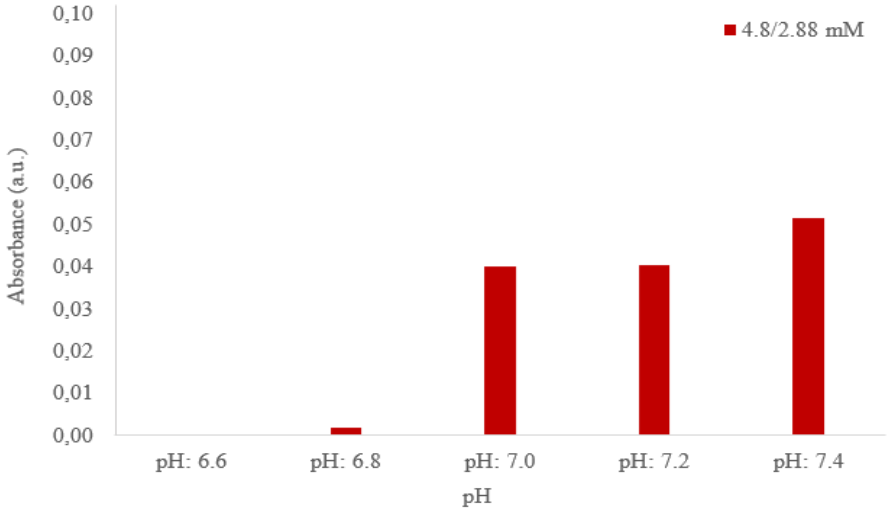

Figure 3.4. Ca^{2+}/PO_4^{3-} nucleation kinetics spectrum at different pH values (pH values between 6.6 and 7.8) and 37 °C in Tris buffer (Ca^{2+}/PO_4^{3-} ratios: 4.8/2.88 mM)

Figure 3.4. shows the absorbance values of Ca^{2+}/ PO_4^{3-} precipitates made under these conditions. It is seen that Ca^{2+}/ PO_4^{3-} precipitates are formed at pH 7.0, 7.2, and 7.4 when the amounts of Ca^{2+} and PO_4^{3-} in the total solution are 50%. Comparing Figure 3.3 and Figure 3.4., it can be concluded that the temperature increase is not consistent at the jump pH values, which is the point of formation of Ca^{2+}/ PO_4^{3-} precipitate, while the absorbance values indicate that the amount of Ca^{2+}/ PO_4^{3-} precipitate decreases (Figure 3.5 shows this result).

These results show that Ca^{2+} and PO_4^{3-} solutions prepared in Tris buffer have a positive effect on Ca^{2+}/ PO_4^{3-} mineralization with increasing pH values. Furthermore, an increase in temperature has a negative effect on these results, but only on the amount of Ca^{2+}/ PO_4^{3-} precipitate formed, and this effect is negligible. Therefore, the result that increasing pH values have a positive effect on the formation of Ca^{2+}/ PO_4^{3-} mineralization gives meaning to the conclusion that a decrease in pH value with increasing temperature decreases the amount of Ca^{2+}/ PO_4^{3-} precipitate. Detailed absorbance graphs of these graphs (Figure 3.3., and Figure 3.4.) are available in APPENDIX A.

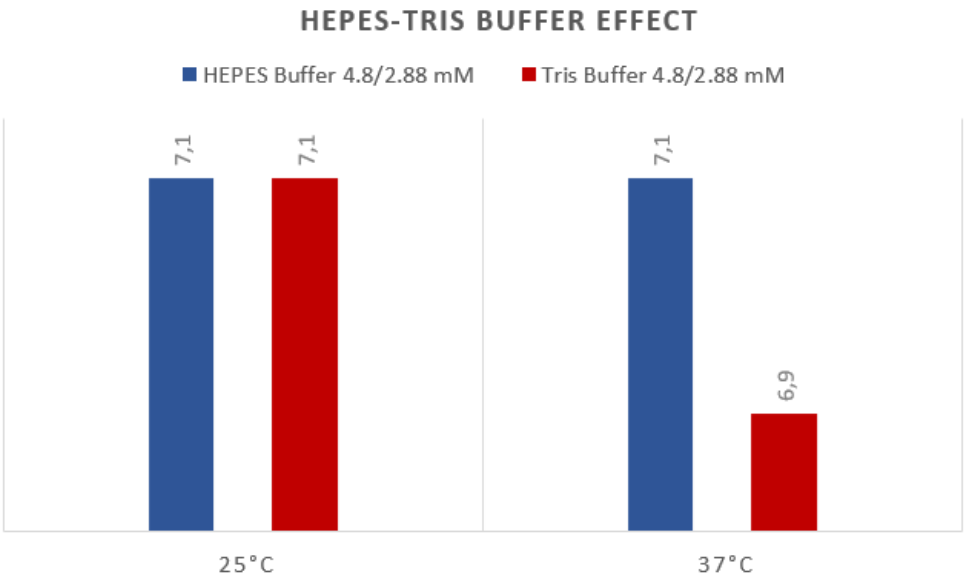

Figure 3.5. pH jumps at constant Ca^{2+}/PO_4^{3-} ratios (4.8/2.88 mM) in HEPES and TRIS buffers and at different temperatures (25°-37 °C)

3.1.3 Optimization of Ca/P Precipitation by Ionic Concentration at Constant pH, Temperature, and HEPES Buffer

In the 2nd set of experiments, the solutions were prepared in HEPES buffer. This is due to the consistent results exhibited in the first experiment in the formation and amount of Ca^{2+}/PO_4^{3-} precipitates under the temperature variation of both pH and molarity parameters. In this study, the HAp cytometer Ca^{2+}/ PO_4^{3-} ratio was kept constant at 1.66. The pH 7.0 value was kept constant after the first experiment showed no Ca^{2+}/PO_4^{3-} sediments were formed. All studies were performed at 25°C. However, the molarity values of the $CaCl_2.2H_2O$ (19.2 Mm) and KH_2PO_4 (11.5 Mm) solutions prepared for this set of experiments were doubled and absorbance measurements of mineralization kinetics were performed by molarity scanning.

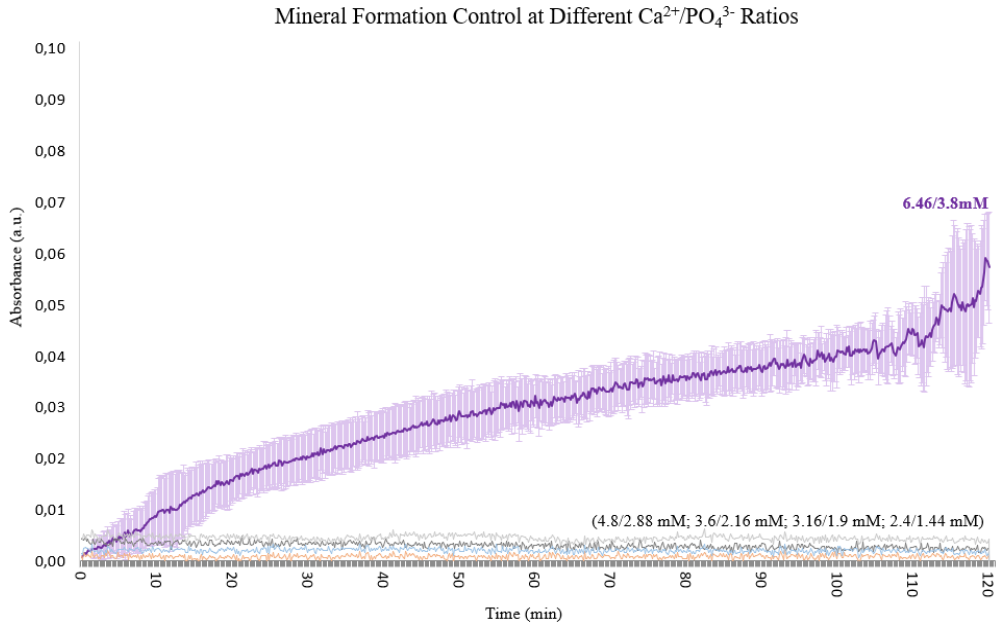

Figure 3.6. Ca^{2+}/PO_4^{3-} nucleation kinetics spectrum at different ionic concentrations, pH: 7.0 and 25°C in HEPES buffer

Figure 3.6 shows that Ca^{2+}/ PO_4^{3-} precipitates were formed when Ca^{2+}/PO_4^{3-} molarity ratios of 6.46/3.8 mM (1.33X) in the total solution were mixed. At the same time, it was observed that Ca^{2+}/PO_4^{3-} precipitates were not formed when Ca^{2+}/PO_4^{3-} molarity ratios of 4.8/2.88 mM (1X), 3.6/1.9 mM (0.75X), 3.16/1.9 mM (0.66X) and 2.4/1.44 mM (0.5X) were mixed in the solution.

The amount of Ca^{2+}/ PO_4^{3-} mineral precipitates formed at which molarity was determined by the studies. Here, it was determined that the amount of HAp mineral precipitation at 1.66 Ca^{2+}/PO_4^{3-} molarity ratio, 2.4/1.44 mM (0.5X), 3.16/1.9 mM (0.66X), 3.6/1.9 mM (0.75X), and 4.8/2.88 mM (1X) concentrations, respectively, was limited and insufficient. The next step is to incubate the phage display library with the solutions at these concentrations and examine the effect on mineralization. However, it was checked that this expected mineralization phenomenon was only an effect of the phages in the phage display library.

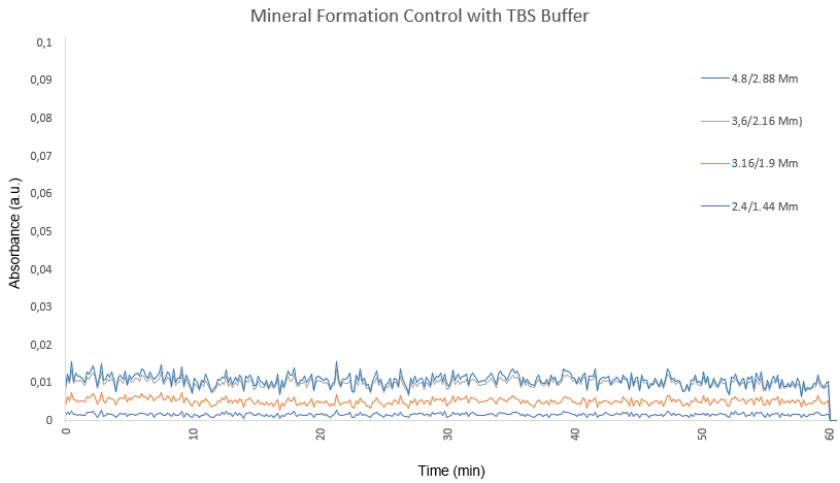

Figure 3.7. The spectrum of the effect on Ca^{2+}/PO_4^{3-} nucleation kinetics at different ionic concentrations in HEPES buffer, pH: 7.0 and 25°C, 50% TBS, and 50% glycerol buffer on Ca^{2+}/PO_4^{3-} nucleation kinetics

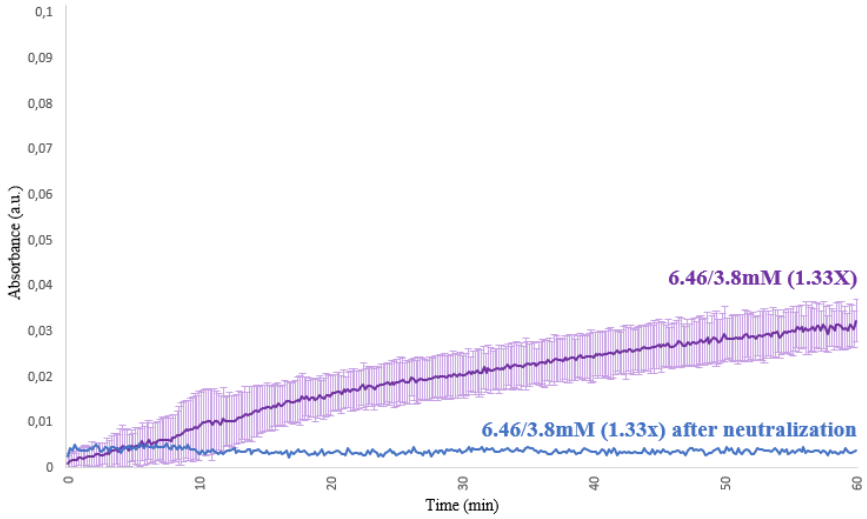

Figure 3.8. The spectrum of mineralization kinetics after neutralization of Ca^{2+}/PO_4^{3-} nucleation

The phage display library is 100 µl, has a concentration of ~ 1 x 10^{13} pfu/ml, and is in TBS solution with 50% glycerol. Mineralization solutions of 0.5X, 0.66X, 0.75X, and 1X concentration were prepared respectively, containing 5% TBS (50% glycerol, pH7.5) in total volume. Figure 3.7 shows the absorbance values of these samples after 1

hour of mineralization kinetics. According to this result, it was observed that the phage-free 50% glycerol TBS solution did not affect the formation of Ca^{2+}/PO_4^{3-} mineral precipitates.

Glycine buffer is a Zwitterionic compound and has pKa values of 2.3-2.4 and 9.6-9.8. The buffering pH range of glycine-HCl combined with hydrochloric acid is 2.2 to 3.6. The pH of the glycine buffer was adjusted to 2.2. It has been proven by previous studies that the solubility of the component phases of calcium phosphate minerals is directly proportional to acidity (León and Jansen 2009). The purpose of using the acidic glycine-HCl buffer prepared in this direction is to dissolve the calcium phosphate minerals phase formed. In this way, it is aimed to obtain mineralizing peptides by dissolving the compact mineral structure formed around the phages carrying mineralizing peptides. The pH value of the phage display library stocking solution is 7.5. In this neutral-basic environment, the stability of phages is ensured. For this reason, the acidic environment will negatively affect the petit-phage library by stressing it. After providing an acidic environment to dissolve the minerals formed by the petit-phage library, this library must be quickly neutralized to prevent damage. For this purpose, firstly, it was calculated how much glycine should be added to reduce the pH of the phage library stock solution of Trima Base buffer, which has a pH of 9.13, to pH 7.5. Then, according to these calculations, 1 ml of 0.2M Glycine buffer was added to the previously prepared mineral pellet formed by the positive control group and separated by precipitation and redissolved. In order to lower the pH of the dissolved pellet to pH 7.5, 160 µl of Trisma Base solution was added. After this neutralization process, was followed by a 1-hour spectrophotometric measurement of whether the calcium phosphates dissolved at pH 7.5 formed minerals again. As can be seen in Figure 3.8, no mineral formation was observed in all control groups after neutralization.

3.2 Selection of Mineralizing Peptides by Directed Evolution Method

Phage display libraries consist of a structure in which the genetic material encoding the various variants is located inside and a library of peptide variants is expressed outside the phage variant (Sidhu, 2000; Croxen, et al. 2013). This phage display

system is based on a simple M13 phage vector modified for the pentavalent display of 12 amino acid peptides via N-terminal fusions to the minor coat protein pIII(Scott, and Smith, 1990; Devlin, Panganiban, and Devlin, 1990). This creates a physical link between each variant peptide sequence and the DNA encoding it, which is based on its affinity for the target molecule through an in vitro selection process called panning (Parmley, and Smith, 1988). This panning is accomplished by incubating a library of phage-displayed peptides in the target, washing out unbound phage, and panning for phage that specifically exhibits the sought-after function. At each biopanning step, an initial concentration of $2x10^{11}$ pfu/ml of the phage library was added to $Ca^{2+/}PO_4^{3-}$ mineral solution with a concentration of 4.8/2.88 Mm, where mineralization could not occur on its own, and left in the mineralization process for approximately 17 hours. The resulting $Ca^{2+/}PO_4^{3-}$ precipitate pellets were amplified by several washing steps. The eluted phage was then amplified and passed through additional mineralization/amplification cycles (Biopanning 2, Biopanning 3, and Biopanning 4) to enrich the pool in favor of mineralizing sequences.

The concentrations of the peptide-phage library obtained after each biopanning step were measured both in plating and nanodrop measurements. In this way, a 2-step concentration control was ensured. Table 3.3 shows the concentration of the peptide-phage libraries found as a result of nanodrop.

Table 3.3. Concentrations of peptide-phage libraries obtained from biopanning rounds as a result of nanodrop measurements and plating calculations

Biopanning Round	Concentration
	Nanodrop (pfu/ml)
BP1-M2	$8,14x10^{12}$
BP2-M2	$5,16x10^{12}$
BP3-M2	$2,61x10^{12}$
BP4-M2	$3,50x10^{12}$

After 1 round of biopanning, the new peptide-phage libraries obtained were diluted in multiples of 10. The peptide-phage libraries from the selected dilution ratios (10^{10}, 10^{11}, and 10^{12}) are seeded on petri dishes and the number of colonies formed at

these dilution ratios is counted and the concentration is calculated with the formula below. As a result of this calculation, the concentration of the peptide-phage library obtained from the biopanning round is learned, and at the same time, with this concentration information, it is calculated how many µl of this library will be added to the new biopanning round and mineralization will start.

To calculate the concentration of the plating result:

$$\text{f plagues x dilution x volume x µl conversion= pfu/ml} \qquad (3.1)$$

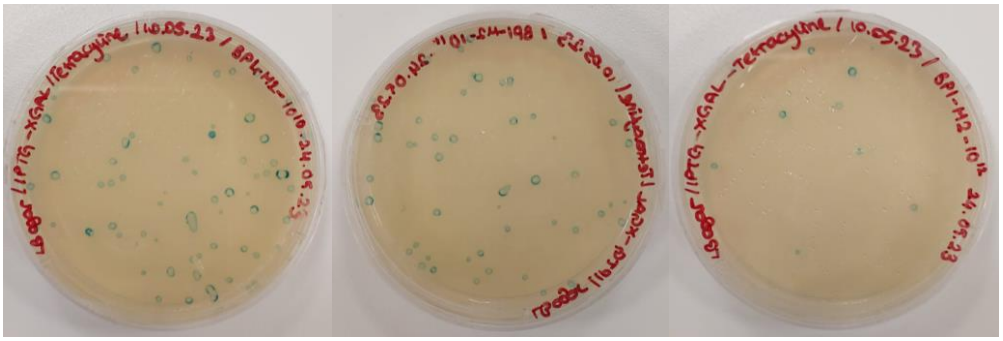

Figure 3.9. Plating results of biopanning round 4 at dilution ratios 10^{10}, 10^{11}, and 10^{12}

For calculating the amount to start mineralization with concentration:

$$\left(\frac{\text{pfu/ml concentrations}}{2} \times \text{Library Volume}(\mu l)\right) \div 1000 = \text{pfu concentrations} \quad (3.2)$$

$$(\text{Library Volume}(\mu l) \times 10^{11}) \div \text{pfu concentrations} = \text{Initial amount}(\mu L) \quad (3.3)$$

Nanodrop measurements and plating calculations showed that the concentration values were consistent. For this reason, the initial amount determined by the separations to be made in all steps was calculated with the concentrations obtained as a result of nanodrop measurements. In fact, the decrease in concentration as the step progresses in biopanning rounds and the increase in the initial amount added to the mineralization medium for the start of mineralization at each step indicates that this peptide-phage library is undergoing a selection and the library is shrinking.

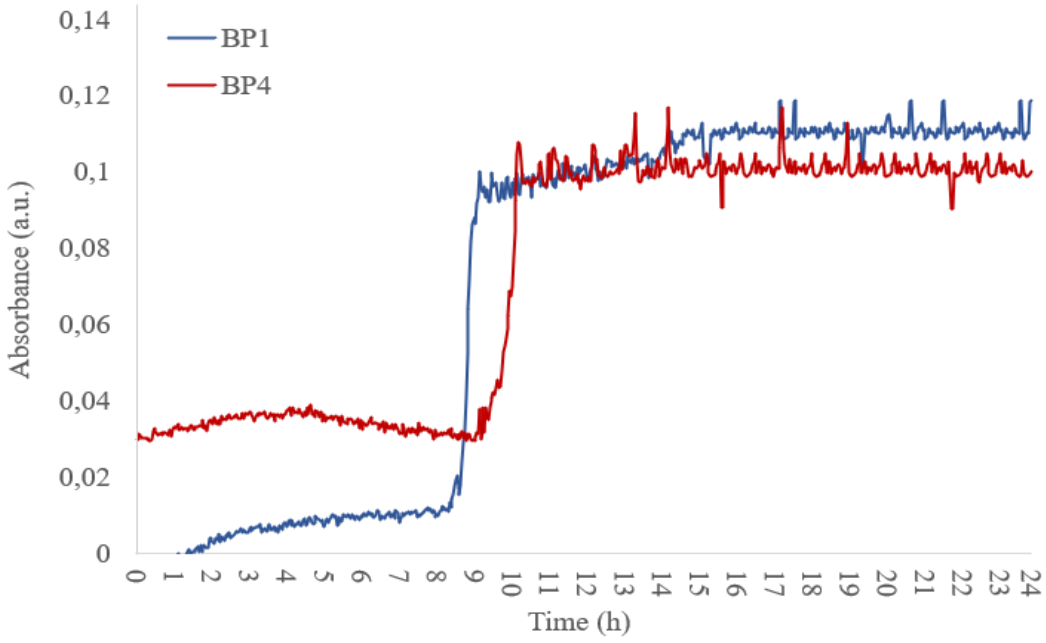

Figure 3.10. 24-hour mineralization kinetics spectrum of Ca^{2+}/PO_4^{3-} nucleation of all biopanning libraries (BP1, and BP4)

A 24-hour spectrophotometric measurement was taken with the libraries (BP1, BP2, BP3, and BP4) obtained at the end of all biopanning. Figure 3.10 shows the absorbance results of the amount of minerals formed as a result of this spectrophotometry. According to this graph, it firstly shows that the synthesis of mineralization has a sudden peak at a certain hour and then the amount of minerals remains stable. From this result, it can be inferred that the mineral crystallizations nucleate and grow at once. Then, again, this graph shows that there are delays in the time of nucleation and growth of mineralization as the selection cascade progresses, although not exactly in a sequential manner.

3.3 Selection of Functional Peptides Eliminated from BP4

3.3.1 DNA Isolation and Sequencing of Functional Peptides

As a result of the selection steps, the BP4-M2 library of the biopanning 4 round, which includes phage libraries that are assumed to carry peptides specific for mineralization function, was determined as the plot group for mineralization kinetics and morphology studies.

For mineralization kinetics and calcium phosphate component phase morphology studies, the BP4-M2 library was first seeded on a large petri dish and 80 colonies were selected. Each of these colonies consists of phages with different peptide sequences. Of course, all these colonies may not be unique from each other. For this reason, the peptide sequences carried by the phages in these colonies should be obtained first. For this purpose, the peptides carried by 37 clones were isolated one by one. In parallel experiments conducted in the Yücesoy research laboratory, 37 clones were isolated. Table 2.2 gives information about the purity and concentration of the DNA sequences isolated from some of the clones. Using the absorbance ratio at 260 nm and 280 nm, the purity of the isolated DNA and RNA is assessed. The values required for DNA and RNA to be pure are as follows;

A ratio of ~1.8 for DNA and ~2.0 for RNA is generally considered "pure". If these purity ratios are significantly lower, it indicates that there may be strongly absorbing proteins, phenols, or other contaminants in the DNA and RNA media. Another purity ratio of 260/230 nm is also an indicator for nucleic acids. Expected 260/230 values for pure nucleic acid isolation are usually in the range 2.0-2.2. Again, if this ratio is significantly lower, it may indicate the presence of contaminants that absorb at 230 nm.

The remaining clones were identified as suitable samples for mineralization kinetics and morphology studies of mineral component phases. These isolated clones were then sequenced individually. The sequences were analyzed by FinchTV, Justbio, and Expasy software for fragment analysis and sequence comparison. From these analyzed DNA sequences, sequences that were error-free and different from each other were selected for purification. Table 3.4 shows the peptide number, molecular weights, Pl and G.R.A.V.Y. values, and charges of the peptides that were error-free and different from each other from the DNA sequences from some of the DNA sequences.

Table 3.4. Sequence information of purified peptides

Peptide Number	MW	pI	G.R.A.V.Y.	Charge
1	4695.06	5.24	0.196	-1
4	1286.49	8.60	0.333	1
5	1268.43	5.52	0.833	0
7	1507.74	6.07	-1.083	0
8	1100.21	9.76	-0.455	1
9	1298.51	5.58	0.183	0
10	1218.38	8.80	0.025	1
12	1396.51	4.09	-0.775	-3
13	1452.64	8.80	-1.158	1
14	1054.71	9.61	-0.792	1
17	1380.48	5.84	-0.817	0
18	1065.11	4.20	-0.582	-2
19	1349.53	8.52	-0.467	1
21	1280.57	5.97	1.342	0

3.4 Mineralization Kinetics of Mineralizing Peptides

Mineralization reactions for each peptide (#1-31) were initiated under standard conditions. Each peptide was added to a solution medium with a final concentration of $1x10^{11}$ pfu/ml and a Ca/P ratio of 5.28/3.17 (1.1X) mM (the amount of HEPES in the solution is different according to the concentration of each peptide). Here, the nucleation potential of the peptides is added to the concentration at the limit to understand the mineralization kinetics.

The results of the peptide mineralization reactions were run for support together with the reactions of the positive (Ca/P: 6.4/3.84 (1.33X) Mm) control group reactions and the negative (Ca/P: 5.28/3.17 (1.1X) Mm) control group reactions. As a result, each peptide exhibited almost different mineralization kinetics. mineral nucleation occurred as soon as Ca^{2+}/PO_4^{3-} ions were placed together in the tube at 1.33X from the positive control groups. Within 1 hour, the absorbance of this nucleation reached approximately 0.07. The negative control group 1.1X (5.28/3.17 mM) nucleation started at 3 h and reached a maximum nucleation absorbance of approximately 0.025. When the peptide was added to the mineralization solution prepared at 1.1X (5.28/3.17 mM) concentration, the nucleation absorbance value either exceeded or almost caught up with the nucleation absorbance values of the positive control groups for all peptide samples. What makes the peptides different from each other here is the time of mineralization kinetics and the absorbance value of nucleation.

In this context, some peptides perform fast mineral nucleation and reach the standard nucleation absorbance value or there are peptides that perform slower mineral nucleation and reach more standard nucleation absorbance values. It follows that neither the speed of mineralization kinetics nor the nucleation absorbance value alone can lead to the conclusion that the ideal Hap mineral crystal is formed. It needs to be supported by morphology analysis of the mineral crystals formed by these peptides by directing and controlling them.

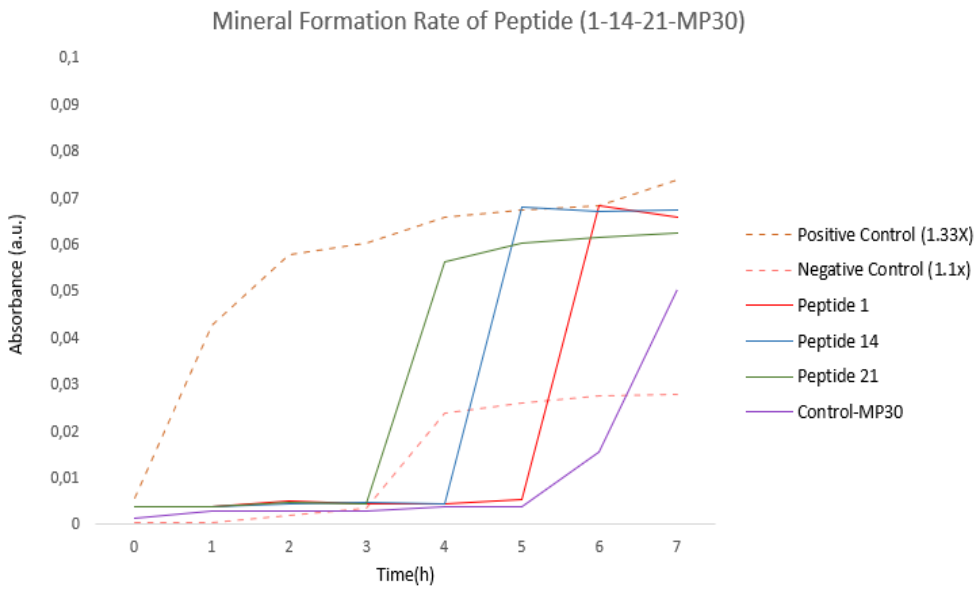

Figure 3.11. Ca^{2+}/PO_4^{3-} nucleation kinetics spectrum of peptides (1-14-21), Control-MP30, negative control (4.8/2.88 mM (1X)) and positive control group (6.46/3.8 mM (1.33X) (total time: 7 hours; at 25°C; pH: 7.0)

Table 3.5. Sequence information of selected purified peptides with parameters of mineralization kinetics and nucleation absorbance values

Peptide Number	MW	pI	G.R.A.V.Y.	Charge
1	4695.06	5.24	0.196	-1
14	1054.71	9.61	-0.792	1
21	1280.57	5.97	1.342	0
30	1220.35	8.76	-0.808	1

For the morphology analysis of the mineral crystals formed by these peptides by directing and controlling them, 4 peptides were selected which started to nucleate at every hour interval in terms of the rate parameter of mineralization kinetics and whose nucleation absorbance values were almost identical to the absorbance value of the positive control group 1.33X. These peptides are peptide 1, peptide 14, peptide 21, and for a positive control a previously identified sequence known as Control-MP30 (courtesy of Yucesoy Research Group). Table 3.5 shows the amino acid sequences of these peptides,

their molecular weights Pl and G.R.A.V.Y. values, and their charges. Figure 3.11 shows the performance of nucleation absorbance value and mineralization kinetics under the guidance and control of these selected peptides.

3.5 Characterization of Mineralizing Peptides

When the peptide was added to the prepared mineralization solution, the nucleation absorbance values either exceeded or almost reached the nucleation absorbance values of the positive control groups for all peptide samples. For the morphology analyses of the mineral crystals formed by these peptides, 4 peptides were selected which started to nucleate at every hour interval in terms of the rate parameter of mineralization kinetics and whose nucleation absorbance values were almost the same as the absorbance value of the positive control group 1.33X. These peptides are peptide 1, peptide 14, peptide 21, and Control-MP30. The crystallinity and morphology of the mineral produced in the presence of these peptides were studied by SEM, XRD, and FTIR analyses.

3.5.1 SEM Analysis

Scanning electron microscopy (SEM) provides information about the structure of synthesized and manufactured products in characterization studies thanks to its micro and nanoscale analysis. For morphology analysis, SEM analysis was performed first. Figure 3.13 shows the same sizes from top to bottom. A is the positive control group, b is Control-MP30, c is peptide 14, d is peptide 21 and e is peptide 1. The points marked in all 5 and 2 μm images show the morphological structure of the mineral phases. These spots show flakes on Control-MP30 and 14. These flakes indicate that a crystalline structure was obtained. However, flakes are not seen on peptide 21 and peptide 1, indicating that these structures are slightly more amorphous. Although SEM is a semi-quantitative analysis, this analysis shows that the structures with fast kinetics are amorphous and those with

slow kinetics form a crystalline structure. However, not all structures with slow kinetics form a crystalline structure, peptide 1 being an example.

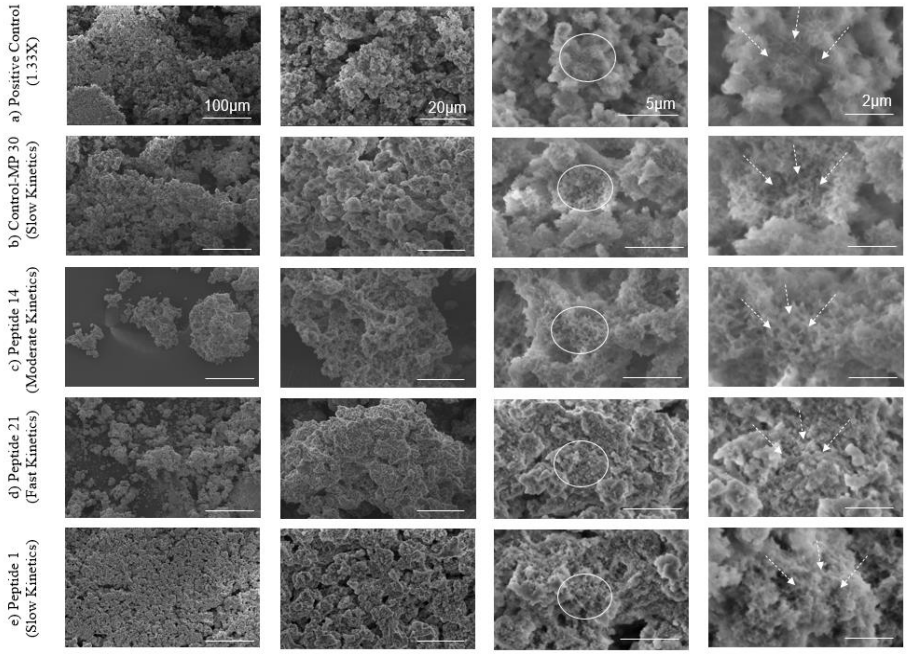

Figure 3.12. SEM image of (a) positive control (6.46/3.8 mM (1.33X)), (b) Control-MP30 (c) peptide 14 (d) peptide 21, and (e) peptide 1. Size bars indicate 100 µm, 20 µm, 5 µm, and 2 µm from left to right, respectively.

3.5.2 XRD Analysis

XRD analysis was performed to evaluate the mineral crystal structures produced in the presence of peptide1, peptide14, peptide21, and MP30. The XRD graph of these peptides is shown in Figure 3.13 The data obtained were compared with the International Centre for Diffraction Data (ICDD, formerly Joint Committee on Powder Diffraction Standards) database (JCPDS no. 09-0432 and 09-0905 for HAp). The XRD patterns of the mineral crystal samples produced via peptides are presented in Figure 3.13 (Thunsiri et al, 2020).

Table 3.6. Diffraction peak positions of pure crystalline HAp at 2θ

2Θ Hap (JCPDS 009-0432)	Plane		
	h	k	l
25.354	2	0	1
25.879	0	0	2
28127	1	0	2
28.967	2	1	0
31.774	2	1	1
32.197	1	1	2
32.902	3	0	0
34.049	2	0	2
35.481	3	0	1
39.205	2	1	2
39.819	3	1	0
42.03	3	1	1
43.805	1	1	3
45.306	2	0	3
46.713	2	2	2
48.104	3	1	2
48.624	3	2	0
49.469	2	1	3

The peaks at angles from 25° to 60° in the 2θ value range are presented in Figure 3. 13. The sharp diffraction peak positions of pure crystalline HA in the 2θ range from 21° to 50° are presented in Table 3.6. Some observed 2θ values of the sharp diffraction peak positions of pure crystalline HAp: 25.86°, 28.12, 28.96, 31.77°, 32.2° and 32.90° correspond to the diffraction planes (h k l values) at (0 0 2), (1 0 2), (2 1 0), (2 1 1) ,(3 0 0), (1 1 2), and (3 1 0), respectively (Thunsiri, et al. 2020). These main characteristic peaks of the mineral crystal samples produced by peptides are similar to the Joint Committee on Powder Diffraction Standards (JCPDS) reference standard file number 09-0905. The XRD patterns of the mineral crystal samples synthesized via peptide 14 and peptide 30 show that some 2θ values of the diffraction peak positions are very similar to those of reference standard 09-0905.

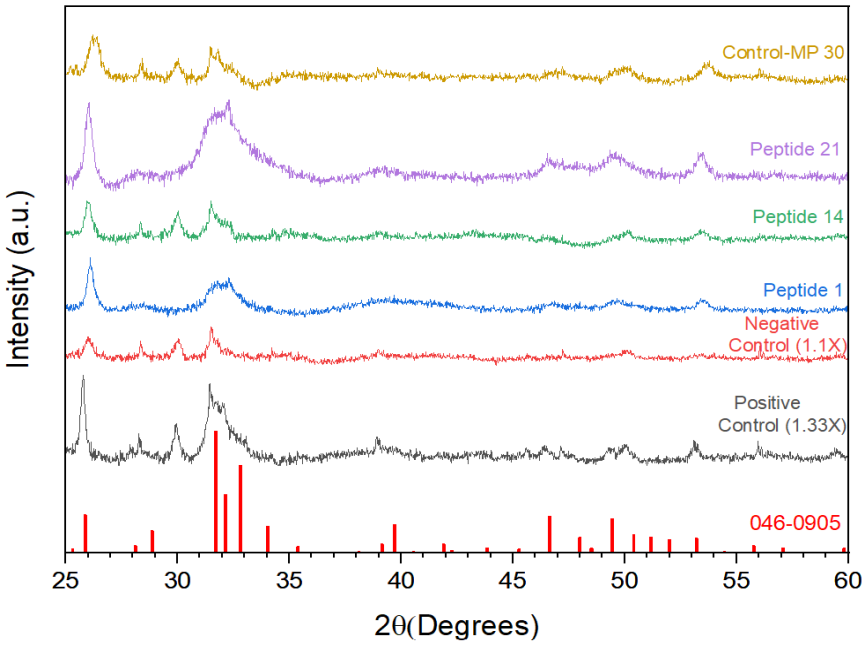

Figure 3.13. XRD spectra of peptides (1-14-21), Control-MP30, and negative control (5.28/3.17 mM (1.1X))

This result indicates that peptide 14 and Control-MP30 control calcium phosphate ions towards the formation of the Hap phase mineral. The fact that the XRD diffraction peak positions of peptide 1 and peptide 21 do not form 28.12°, 28.96° 2θ values and the heights of the peak peaks at 32.2°, 32.90° 2θ values are different from the pure Hap crystal shows that these mineral structures are not completely directed to the Hap phase.

3.5.3 FTIR Analysis

FTIR spectroscopy analyses were used to evaluate the bond formation of nanomaterials to determine the functional groups present in the mineral crystals and to compare the transmission peaks obtained with the mineral phase groups in the literature. The band classification in some mineral phase groups in the existing literature is as follows:

The bands formed at 567 cm^{-1}, 601 cm^{-1}, and 631 cm^{-1} in HAp crystal form indicate phosphate *v*4 vibrations. The 876 cm^{-1} band shows carbonate *v*2 vibration and the 962 cm^{-1} band shows phosphate ν1 symmetric stretching vibration. Strong bands at 1025 cm^{-1} and 1086 cm^{-1} indicate phosphate *v*3 vibration, while bands at 1417 cm^{-1} and 1456 cm^{-1} indicate *v*3 vibrations of surface carbonate groups (Rehman, and Bonfield, 1997). TCP in its crystalline form had similar characteristic peaks, referring to the same functional groups as HAp for the given band range, except for the bands occurring in the 1400-1460 cm^{-1} spectrum. It is difficult to distinguish between both crystal phases of TCP by fluorescence analysis. This is because both α- and β-TCP exhibit bands with similar wave numbers (Fowler, Moreno, and Brown, 1966).

In the crystalline form of OCP, these bands are as follows; the broad peak at 3448 cm^{-1} is produced by the crystalline water in OCP and 1651 cm^{-1} by the hydroxyl group in the crystalline water of OCP. The peak at 2364 cm^{-1} should be attributed to CO_2 in the air, i.e. the COC stretch oscillation absorption peak. The spectral bands of 601 cm^{-1}, and 1031 cm^{-1} region show vibrations of PO_4 (*v*3). The spectral bands at 570 cm^{-1} (*v*4 PO_3^{4-}), 866 cm^{-1} (*v*2 CO_2^{3-}), 1045 cm^{-1} (*v*3 PO_4^{3-}), 1415 and 1505 cm^{-1} (*v*3 CO_2^{3-}), 1670 and 3000-3500 cm^{-1} (water bands) of the ACP crystal form. The absorption bands of the amorphous phase are rounded and do not show sharp vibration peaks (Rehman, and Bonfield, 1997).

In this study, FTIR spectroscopy analyses of the negative control group (5.28/3.17 mM Ca/P ratio) have passed into the mixed phase of the mineral. 3448 cm^{-1} indicates the presence of OCP (crystal water of OCP). 1456 and 1417 cm^{-1} showed the presence of Hap but these bands are weak signals.

Figure 3.14. shows that, FTIR spectroscopy analyses of the crystal and morphology of the mineral produced in the presence of, peptide14, and Control-MP30 show phosphate vibration bands formed at 567 cm^{-1}, 601 cm^{-1}, and 631 cm^{-1} of the crystal form. The carbonate ν2 vibration bands at 876 cm^{-1} and the phosphate *v*1 symmetrical stretching vibration bands at 962 cm^{-1} are shown. Phosphate *v*3 vibration bands at 1025 cm^{-1} and 1086 cm^{-1} are shown and *v*3 vibration bands of surface carbonate groups at 1417 and 1456 cm^{-1} are shown. As a result, all peptides were shown to direct the mineral crystal and morphology in the direction of the Hap phase.

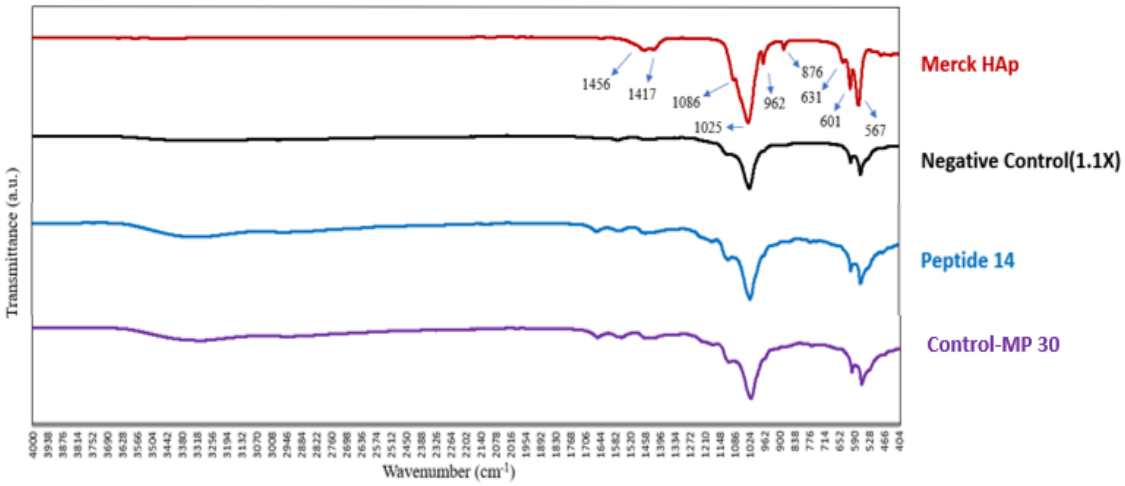

Figure 3.14. FTIR spectra of peptides14, Control-MP30, and negative control (5.28/3.17 mM (1.1X))

FTIR analyses also showed the formation of HAp bands in these two phases, which is consistent with the XRD analysis. These peptides hold the potential for developing clinical products, such as dental gels, toothpaste formulations, and treatments for bone regeneration.

The inclusion of different types of anions in the HAp unit cell, which affects the vibration of PO_4 and causes local structural distortions around these ions, may cause an expansion in this region. Therefore, the phosphate substitution site area can give information about the crystal structure of HAp. In order to obtain information about the crystal structure, the calculation of the 567 cm-1 and 601 cm-1 bands of the FTIR peaks representing the O-P-O bending of phosphate in HA divided by the height of the peak maximum valley shows the crystallinity index of the mineral phase structure (Shlaferman et al, 2019; Weiner, and Bar-Yosef, 1990). The crystallinity index values of the standard HAP phase vary between 5 and 13 (Shlaferman et al, 2019; Choi et al, 2015). According to these results, the crystallinity of none of the peptide-orientated mineral phases is as crystalline as the pure HAp phase. However, it is shown that none of these mineral phases are amorphous.

FTIR analysis can only be analyzed in the range of 4000-400cm^{-1}. Since these results are not as specific as desired, they cannot be used as a reference study for morphology alone. These results are supported by XRD and SEM analysis.

CHAPTER 4

CONCLUSION

Biomineralization is a fundamental biological phenomenon that drives the coordinated precipitation and growth of inorganic ions together with organic protein molecules in various organisms. It is assumed that this process is driven by protein molecules and determines the hierarchical structure of the formed tissue. The unique properties of hard mineral tissues produced by the biomineralization process in living organisms, such as durability, hardness, and flexibility, are regulated by this process. The formation of hard tissues such as bones and teeth in vertebrates, especially humans, and shells in invertebrate mollusks is part of biomineralization. The current literature is replete with studies on the application of nanotechnology in hard tissue research and dentistry to mimic the in vitro synthesis of such biomimetic materials. The interaction of synthetically produced mineral materials with living tissue must be optimized. This optimization is achieved by synthetic mineral biomaterials that mimic all the properties of biological tissues and biogenic materials in terms of functionality. The high degree of complexity, hierarchical organization, hybridization, reliability, efficiency, resilience, and adaptability of natural materials obtained by certain structural principles selected by evolution can be partially achieved in biogenic materials synthesized by man-made synthetic processes. Biomimetic studies are crucial for the design and synthesis of innovative and progressive materials and structures.

The nanometer-scale conformational variability of biological complex compact structures triggers biological macromolecules to promote the formation of specific linkages. Hydroxyapatite (HA), $Ca_{10}(PO_4)_6(OH)_2$, the major inorganic compound of mammalian bone and dental tissues, is one of the most stable forms of calcium phosphates. A better understanding of the crystallization mechanism of hydroxyapatite (HA) in the natural mineralization synthesis process and its applicability as an industrial material is being deeply investigated in numerous interdisciplinary fields. Morphology, biocompatibility, bioactivity, bioabsorbability, osteoconductivity, and surface functionalization in synthetic HA crystals represent the physical and chemical properties

required to optimize applicability as industrial materials. Synthetic hydroxyapatites synthesized from Ca/P minerals by mimicking natural biomineralization processes exhibit good properties such as direct binding to tissue, biocompatibility, bioactivity, osteoconductivity, etc., which is exciting for applications in restorative dental treatment fields.

The ambient conditions under which biomimetic mineralization occurs are crucial for the morphology and formation kinetics of Ca/P mineral crystals. Through iterative experiments, the optimal conditions for variables such as pH, temperature and molarity were set, recognizing their dynamic influence on the mineralization process. The control of pH, one of the dynamic variables in a biological environment, can be set, maintained, and modified in the liquid phase through equilibration using an appropriate buffer. Considering the pH values of the intraoral environment, HEPES and Tris buffers were decided to be the most suitable buffers, and the mineralization solution medium was prepared using these two buffers. In order to trigger the mineral deposition rate and crystal morphology, it is necessary to mimic body conditions. Here the solution is kept and maintained at physiological body temperature (37°C). Temperature is another parameter that facilitates the kinetics of precipitate formation. Mimicking body conditions is an important step in influencing the rate of mineral deposition and crystal morphology. The molarity variable, whose dynamic effect on the mineralization process is recognized, is another parameter that facilitates the kinetics of the formation of biomimetic hydroxyapatite nanocrystals from Ca/P minerals. Supersaturation in terms of the ionic concentration of the solution is very important as it triggers the precipitation of Ca/P minerals. Considering the effects of pH, temperature, and molarity parameters on calcium phosphate precipitation, the optimal condition was optimized. However, choosing the optimum condition is complicated because the parameters are interrelated.

Ca/P molarity ratios were kept constant at 1.66 for all test sets. Ca/P=1.66 is the stoichiometric HAP value. A healthy intraoral pH is physiologically maintained in the pH 6.8-7.8 range. Therefore, mineralization kinetics were studied in this pH range. One of the most powerful and effective ways to trigger Ca/P crystallization is pH. Without any precipitant, only small changes in pH can be highly effective on mineralization. The first result of these optimization studies showed that at a constant Ca/P ratio, mineral analysis showed that increasing pH (within the specified pH range) had a positive effect on the amounts of precipitated calcium and phosphate.

Ca/P molarity ratios were kept constant for all test sets, the Ca^{2+} and PO_4^{3-} molarities in the total solution were 4.8/2.88 mM. In previous studies, mineralization nucleation performance was proven when the Ca^{2+}/PO_4^{3-} ratio was kept at 4.8/2.88 mM (1X). These optimization studies were first carried out at a standard room temperature of 25 °C. The study was repeated by increasing only the temperature to 37 °C without changing the molarity and pH parameters. The effect of temperature change on the HEPES buffer was checked. The pH change in all solutions decreased by 0.13 (+_0.01) on average. Therefore, the pH values in the study were assumed to be approximately 0.13 less with this treatment and evaluated accordingly. To check the effect of temperature change on Tris buffer, the solutions were heated to 37 °C. The pH change in all solutions decreased by an average of 0.32 (+_0.01). Therefore, it is not appropriate to use the same solutions by heating as the rate of change of pH values in the study would change the pH range of the study. Therefore, the solutions were prepared again by adjusting the pH at 37°C and these solutions were used for the 37°C experiments. In the studies of mineralization solutions prepared with HEPES buffer solution, a negative effect of temperature increase on the mineralization results was observed, but this effect was only on the amount of Ca/P precipitate and this effect was negligible. This is evidenced by the fact that there is no change in the pH value of the Ca/P precipitation formation jump points. Therefore, the result of the positive effect on the formation of Ca/P mineralization with increasing pH values gives meaning to the conclusion that the decrease in pH value with increasing temperature decreases the amount of Ca/P precipitate. It is seen that the absorbance values of Ca/P precipitates increase continuously with increasing pH values. This leads to the conclusion that pH increase has a positive effect on Ca/P mineralization. It shows that Ca^{2+} and PO_4^{3-} solutions prepared in Tris buffer have a positive effect on Ca/P mineralization with increasing pH values, while the change in molarity has a linear effect on the amount of Ca/P precipitate formed. Furthermore, an increase in temperature has a negative effect on these results, but only on the amount of Ca/P precipitate formed, and this effect is negligible. Therefore, the conclusion that increasing pH values have a positive effect on the formation of Ca/P mineralization gives meaning to the conclusion that a decrease in pH value with increasing temperature reduces the amount of Ca^{2+}/PO_4^{3-} precipitate. The consistent behavior of both pH and molarity parameters on the formation and amount of Ca/P precipitates under temperature variation in solutions prepared in HEPES buffer proved that it is the ideal buffer for optimization conditions.

The HAP cytometer Ca/P ratio was kept constant at 1.66. The molarity values of the solutions were doubled and molarity scanning and mineralization kinetics were performed by absorbance measurements. Since the mineralization kinetics of HEPES buffer is not affected by temperature variation, it was sufficient to perform all studies only at 25°C. As a result of the first experiment, one pH value below the pH value, which is the mineralization jump point of the HEPES Buffer, was taken as the reference point. Ca/P precipitates were formed in solutions containing Ca/P molarity ratios of 6.46/3.8 mM (1.33X), while 4.8/2. 88 mM (1X), 3.6/1.9 mM (0.75X), 3.16/1.9 mM (0.66X) and 2.4/1.44 mM (0.5X) Ca^{2+}/PO_4^{3-} molarity ratios.

Here, the Ca/P molarity ratio was determined to be limited and insufficient for HAp mineral precipitation at concentrations of 2.4/1.44 mM (0.5X), 3.16/1.9 mM (0.66X), 3.6/1.9 mM (0.75X) and 4.8/2.88 mM (1X), respectively. The next step was to incubate the phage display library with solutions at these concentrations and study the effect on mineralization. However, it was checked that this expected mineralization phenomenon was only an effect of the phages in the phage display library.

Mineralization solutions with concentrations of 0.5X, 0.66X, 0.75X, and 1X, respectively, containing TBS solution, the stock solution of the peptide-phage library, were prepared and it was shown that the phage-free TBS solution did not affect the formation of Ca/P mineral precipitates. It was aimed to obtain mineralized peptides by dissolving the compact mineral structure formed around the phages carrying mineralized peptides. The purpose of using the acidic glycine-HCl buffer prepared accordingly is to dissolve the calcium phosphate minerals phase. The pH of the phage display library stocking solution was 7.5. In this neutral-basic environment, the stability of the phages is ensured. Therefore, an acidic environment will stress and negatively affect the petit-phage library. Once an acidic environment is provided to dissolve the minerals formed by the petit-phage library, this library needs to be neutralized quickly to avoid damage. For this purpose, we first calculated how much glycine should be added to lower the pH of the phage library stock solution of Trizma Base buffer to pH 7.5. Then, according to these calculations, the acidic solution was added to the pre-prepared mineral pellet formed by the positive control group, which was separated by precipitation and redissolved. The basic solution was added to reduce the pH of the dissolved pellet to pH 7.5. After this neutralization process, it was determined whether the calcium phosphates dissolved at pH 7.5 formed minerals again.

Phage display libraries consist of a construct in which a library of peptide variants is expressed outside of the constituent phage variant. This phage display system creates a physical link between the sequence of the 12 amino acid peptide and the DNA encoding it, based on its affinity for the target molecule through an in vitro selection process called sliding. This swiping is accomplished by incubating a library of phage-displayed peptides at the target, washing out unbound phage, and swiping specifically for phage that exhibit the sought-after function. In each biopanning step, the inability of mineral precipitation to occur on its own was demonstrated by adding the phage library to a Ca/P mineral solution with a concentration of 4.8/2.88 Mm. Kinetic measurements revealed that these peptides catalyze calcium phosphate mineralization about one order of magnitude faster than under physiological conditions. The decrease in concentration as the step progressed in the biopanning rounds and the increase in the initial amount added to the mineralization medium to initiate mineralization at each step indicated that this peptide-phage library underwent a selection and the library became smaller.

For mineralization kinetics and morphology studies, the BP4-M2 library of the biopanning 4 round, which contains phage libraries that are assumed to carry peptides specific for mineralization function, was selected as the plot group. For mineralization kinetics and calcium phosphate component phase morphology studies, peptides carried by 37 unique clones were isolated one by one in colonies selected from the BP4-M2 library. The selected clones were identified as suitable samples for mineralization kinetics and morphology studies of mineral component phases.

Mineralization reactions for the peptides carried by these clones were initiated by adding them to a solution medium with a Ca/P ratio of 5.28 / 3.17 Mm (1.1X). The nucleation potential of the peptides was added to the limiting concentration to understand the mineralization kinetics. The results of the peptide mineralization reactions were supported by positive control group reactions and negative control group reactions. As a result, each peptide exhibited almost different mineralization kinetics. When the peptide was added to the mineralization solution prepared at a concentration of 1.1X (5.28/3.17 mM), the nucleation absorbance value either exceeded or almost caught up with the nucleation absorbance values of the positive control groups for all peptide samples. Here, it was the time course of the mineralization kinetics and the absorbance value of nucleation that differentiated the peptides from each other. In this context, there are some peptides that perform fast mineral nucleation and reach the standard nucleation value or there are peptides that perform slower mineral nucleation and reach more standard

nucleation absorbance values. It follows that neither the rate of mineralization kinetics nor the nucleation absorbance value alone can lead to the conclusion that an ideal Hap mineral crystal is formed. The mineral crystals formed by these peptides had to be guided, controlled, and supported by morphology analysis.

For the directed and controlled morphology analysis of the mineral crystals formed by these peptides, 4 peptides were selected, which started to nucleate at every hour interval in terms of the rate parameter of mineralization kinetics and whose nucleation absorbance values were almost the same as the absorbance value 1.33X of the positive control group. These peptides are peptide 1, peptide 14, peptide 21, and MP30. The crystallinity and morphology of the mineral produced in the presence of these peptides were studied by SEM, XRD, and FTIR analyses. The minerals synthesized by catalyzing the 4 peptides selected for morphology analysis were firstly SEM analyzed. It shows flakes in the mineral structure formed by MP30 and peptide14. These flakes show that a crystalline structure was obtained. However, flakes are not seen in the mineral structure formed by peptide 21 and peptide 1, indicating that these structures are slightly more amorphous. Although SEM is a semi-quantitative analysis, this analysis shows that the structures with fast kinetics are amorphous, while those with slow kinetics form a crystalline structure. However, not all structures with slow kinetics form a crystalline structure, peptide 1 being an example. XRD patterns of the mineral crystal samples synthesized via peptide 14 and Control-MP30 show that some 2θ values of the diffraction peak positions are quite similar to the reference standard 09-0905. This result shows that peptide 14 and Control-MP30 control calcium phosphate ions towards the formation of Hap phase mineral. FTIR analysis results of these peptides support this result. The fact that the XRD diffraction peak positions of peptide 1 and peptide 21 do not form 28.12°, 28.96° 2θ values and the heights of the peak peaks at 32.2°, 32.90° 2θ values are different from the pure Hap crystal shows that these mineral structures are not completely directed to the Hap phase. These peptides show phosphate vibration bands formed at 567 cm^{-1}, 601 cm^{-1}, and 631 cm^{-1} of the crystal form. The carbonate ν2 vibration bands at 876 cm^{-1} and the phosphate $\nu 1$ symmetrical stretching vibration bands at 962 cm^{-1} are shown. Phosphate $\nu 3$ vibration bands at 1025 cm^{-1} and 1086 cm^{-1} are shown and $\nu 3$ vibration bands of surface carbonate groups at 1417 and 1456 cm^{-1} are shown. As a result, all peptides were shown to direct the mineral crystal and morphology in the direction of the Hap phase. These peptides hold the potential for developing clinical products, such as dental gels, toothpaste formulations, and treatments for bone regeneration.

REFERENCES

Andreassen, J.P., & Lewis, A.E. (2017). Classical and Nonclassical Theories of Crystal Growth. In *New Perspectives on Mineral Nucleation and Growth*, 1st ed.; Springer, Cham; pp 137-154. DOI: 10.1007/978-3-319-45669-0_7

Anisimov, M. P. (2003). Nucleation: Theory and Experiment. *Russian Chemical Reviews,* 72 (7): 591–628.

Asnaashari, M., & Moeini. M. (2013). Effectiveness of Lasers in the Treatment of Dentin Hypersensitivity. *Journal of Lasers in Medical Sciences,* 4 (1): 1-7

Beniash, E., Simmer, J. P., & Margolis, H. C. (2012). Structural Changes in Amelogenin upon Self-Assembly and Mineral Interactions. *Journal of Dental Research,* 91 (10): 967–972.

Benson, P. E., Parkin, N., Dyer, F., Millett, D.T., Furness, S., & Germain, P. (2013). Fluorides for the Prevention of Early Tooth Decay (Demineralised White Lesions) during Fixed Brace Treatment. *Cochrane Database of Systematic Reviews,* (12):1-32.

Bertassoni, L. E., Habelitz, S., Kinney, J. H., Marshall, S. J., & Marshall Jr, G. W. (2009). Biomechanical Perspective on the Remineralization of Dentin. *Caries Research,* 43 (1): 70–77.

Bertassoni, L. E., Habelitz, S., Marshall, S. J., & Marshall, G. W. (2011). Mechanical Recovery of Dentin Following Remineralization in Vitro — An Indentation Study. *Journal of Biomechanics,* 44 (1): 176–181.

Bigi, A., Boanini, E., Panzavolta, S., & Roveri, N. (2000). Biomimetic Growth of Hydroxyapatite on Gelatin Films Doped with Sodium Polyacrylate. *Biomacromolecules,* 1 (4): 752–756.

Bohner, M. (2000). Calcium Orthophosphates in Medicine: From Ceramics to Calcium Phosphate Cements. *Injury,* 31 (4): D37–47.

Bartlett, J. D., and Simmer, J. P. (1999). Proteinases in Developing Dental Enamel. *Critical Reviews in Oral Biology & Medicine,* 10 (4): 425–441.

Bosshardt, D. D. (2005). Are Cementoblasts a Subpopulation of Osteoblasts or a Unique Phenotype? *Journal of Dental Research,* 84(5):390–406.

Bostanov, V., Mladenova, E. & Kashchiev, D. (2000). Nucleation Rate in Electrocrystallization of Cadmium on the Cd (0001) Crystal Face. *Journal of Electroanalytical Chemistry,* 481 (1): 7–12.

Cao, C. Y., Mei, M. L., Li, Q. L., Lo, E. C. M., & Chu, C. H. (2015). Methods for Biomimetic Remineralization of Human Dentine: A Systematic Review. *International Journal of Molecular Sciences,* 16 (3): 4615–4627.

Chaffee, B.W., Feldens, C. A., & Vítolo, M. R. (2014). Association of Long-Duration Breastfeeding and Dental Caries Estimated with Marginal Structural Models. *Annals of Epidemiology,* 24 (6): 448–454.

Chai, C. S., & Ben-Nissan, B. (1999). Bioactive Nanocrystalline Sol-Gel Hydroxyapatite Coatings. *Journal of Materials Science: Materials in Medicine,* 10 (8): 465–69.

Chen, R.S., Liu, C.C., Tseng, W.Y., Jeng, J.H., & Lin, C.P. (2003). Cytotoxicity of Three Dentin Bonding Agents on Human Dental Pulp Cells. *Journal of Dentistry*, 31(3): 223–229.

Choi, S., Coonrod, S., Estroff, L., & Fischbach, C. (2015). Chemical and Physical Properties of Carbonated Hydroxyapatite Affect Breast Cancer Cell Behavior. *Acta Biomaterialia,* 24 (September): 333–342.

Cobourne, M. T., & Sharpe, P. T. (2014). Tooth Development. In *Fundamentals of Oral Histology and Physiology,* 1st ed.; John Wiley & Sons; pp 44-58.

Cochrane, N. J., Cai, F., Huq, N. L., Burrow, M. F., & Reynolds, E. C. (2010). Critical Review in Oral Biology & Medicine: New Approaches to Enhanced Remineralization of Tooth Enamel. *Journal of Dental Research,* 89 (11): 1187–97.

Cölfen, H., & Mann, S. (2003). Higher-Order Organization by Mesoscale Self-Assembly and Transformation of Hybrid Nanostructures. *Angewandte Chemie International Edition,* 42 (21): 2350–65.

Croxen, M.A., Law, R. J., Scholz, R., Keeney, K. M., Wlodarska, M., & Finlay, B. B. (2013). Recent Advances in Understanding Enteric Pathogenic Escherichia Coli. *Clinical Microbiology Reviews,* 26 (4): 822-880.

Cummins, D. (2013). Dental Caries: A Disease Which Remains a Public Health Concern in the 21st Century–the Exploration of a Breakthrough Technology for Caries Prevention. *Journal of Clinical Dentistry,* 24(Spec Iss A): A1–A14.

Deshpande, A.S., Fang, P. A., Simmer, J.P., Margolis, H. C., & Beniash, E. (2010). Amelogenin-Collagen Interactions Regulate Calcium Phosphate Mineralization in Vitro. *Journal of Biological Chemistry,* 285 (25): 19277–19287.

Devlin, J. J., Panganiban, L. C., & Devlin, P. E. (1990). Random Peptide Libraries: A Source of Specific Protein Binding Molecules. *Science,* 249 (4967): 404–406.

De Yoreo, J. J., Gilbert, P. U., Sommerdijk, N. A., Penn, R. L., Whitelam, S., Joester, D., Zhang, H., et al. (2015). Crystallization by Particle Attachment in Synthetic, Biogenic, and Geologic Environments. *Science,* 349(6247), aaa6760-1– aaa6760-9.

Dogan, S., Fong, H., Yucesoy, D. T., Cousin, T., Gresswell, C., Dag, S., Huang, G., & Sarikaya, M. (2018). Biomimetic Tooth Repair: Amelogenin-Derived Peptide Enables In Vitro Remineralization of Human Enamel. *ACS Biomaterials Science and Engineering,* 4 (5): 1788–1796.

Doméjean, S., Ducamp, R., Léger, S., & Holmgren, C. (2015). Resin Infiltration of Non-Cavitated Caries Lesions: A Systematic Review. *Medical Principles and Practice,* 24 (3): 216–221.

Dorozhkin, S. V. (2010). Nanosized and Nanocrystalline Calcium Orthophosphates. *Acta Biomaterialia,* 6 (3): 715–734.

Dorozhkin, S.V., Dorozhkina, E.I., & Epple, M. (2003). Precipitation of Carbonate Apatite from a Revised Simulated Body Fluid in the Presence of Glucose. *Journal of Applied Biomaterials and Biomechanics*, 1(3):200-207

Eliaz, N., & Metoki, N. (2017). Calcium Phosphate Bioceramics: A Review of Their History, Structure, Properties, Coating Technologies and Biomedical Applications. *Materials,* 10 (4): 1-104

Enax, J., & Epple, M. (2018). Synthetic Hydroxyapatite as a Biomimetic Oral Care Agent. *Oral Health & Preventive Dentistry,* 16 (1): 7-19

Featherstone, J. D.B. (2008). Dental Caries: A Dynamic Disease Process. *Australian Dental Journal,* 53 (3): 286–91.

Flatken, M. A. (2022). The Early Stages of Halide Perovskites Thin Film Formation. Ph.D Dissertation, Dissertation, University of Potsdam. https://nbn-resolving.org/urn:nbn:de:kobv:517-opus4-552599 (accessed 2024-06-10)

Fleming, P. S., DiBiase, A. T., Sarri, G., & Lee, R. T. (2009). Pain Experience during Initial Alignment with a Self-Ligating and a Conventional Fixed Orthodontic Appliance System a Randomized Controlled Clinical Trial. *The Angle Orthodontist*, 79 (1): 46–50.

Fowler, B. O., Moreno, E. C., & Brown, W. E. (1966). Infra-red spectra of Hydroxyapatite, Octacalcium Phosphate, and Pyrolysed Octacalcium Phosphate. *Archives of Oral Biology,* 11 (5): 477–92.

Francis Suh, J. K., & Matthew, H. W. (2000). Application of Chitosan-Based Polysaccharide Biomaterials in Cartilage Tissue Engineering: A Review. *Biomaterials,* 21 (24): 2589–98.

Fujibayashi, S., Nakamura, T., Nishiguchi, S., Tamura, J., Uchida, M., Kim, H. M., & Kokubo, T. (2001). Bioactive Titanium: Effect of Sodium Removal on the Bone-Bonding Ability of Bioactive Titanium Prepared by Alkali and Heat Treatment. *Journal of Biomedical Materials Research: An Official Journal of The Society for Biomaterials, The Japanese Society for Biomaterials, and The Australian Society for Biomaterials and the Korean Society for Biomaterials*, *56*(4), 562-570

Gao, S. S., Zhang, S., Mei, M. L., Lo, E. C. M. & Chu, C. H. (2016). Caries Remineralisation and Arresting Effect in Children by Professionally Applied Fluoride Treatment - a Systematic Review. *BMC Oral Health,* 16 (1): 1–9.

García-Godoy, F., & Hicks, M. J. (2008). Maintaining the Integrity of the Enamel Surface: The Role of Dental Biofilm, Saliva and Preventive Agents in Enamel Demineralization and Remineralization. *The Journal of the American Dental Association,* 139 (5 SUPPL.): 25S-34S.

Gbureck, U., Barralet, J. E., Hofmann, M. P., & Thull, R. (2004). Nanocrystalline Tetracalcium Phosphate Cement. *Journal of dental research*, *14* 83 (5): 425–28.

Gebauer, D., Gunawidjaja, P. N., Ko, J. P., Bacsik, Z., Aziz, B., Liu, L., Hu, Y., et al. (2010). Proto-Calcite and Proto-Vaterite in Amorphous Calcium Carbonates. *Angewandte Chemie International Edition,* 49 (47): 8889–8891.

Gebauer, D., Volkel, A., & Colfen, H. (2008). Stable Prenucleation Calcium Carbonate Clusters. *Science,* 322 (5909): 1819–1822.

George, A., & Veis, A. (2008). Phosphorylated Proteins and Control over Apatite Nucleation, Crystal Growth, and Inhibition. *Chemical Reviews,* 108 (11): 4670–4693.

Goldberg, M., Kulkarni, A. B., Young, M., & Boskey, A. (2011). Dentin: Structure, Composition, and Mineralization: The Role of Dentin ECM in Dentin Formation and Mineralization. *Frontiers in Bioscience (Elite Edition),* 3 (2): 711-735.

Goldberg, M., Lacerda-Pinheiro, S., Jegat, N., Six, N., Septier, D., Priam, F., Bonnefoix, M. et al. (2006). The Impact of Bioactive Molecules to Stimulate Tooth Repair and Regeneration as Part of Restorative Dentistry. *Dental Clinics of North America,* 50 (2): 277–98.

Gower, L. B. (2008). Biomimetic Model Systems for Investigating the Amorphous Precursor Pathway and Its Role in Biomineralization. *Chemical Reviews,* 108 (11): 4551–4627.

Gronthos, S., Mankani, M., Brahim, J., Robey, P. G., & Shi, S. (2000). Postnatal Human Dental Pulp Stem Cells (DPSCs) In Vitro and In Vivo. *Proceedings of the National Academy of Sciences of the United States of America,* 97 (25): 13625–30.

Guo, X., Gough, J. E., Xiao, P., Liu, J., & Shen, Z. (2007). Fabrication of Nanostructured Hydroxyapatite and Analysis of Human Osteoblastic Cellular Response. *Journal of Biomedical Materials Research Part A,* 82A (4): 1022–32.

Iafisco, M., Marchetti, M., Gómez Morales, J., Hernández-Hernández, M. A., Garcia Ruiz, J. M., & Roveri, N. (2009). Silica Gel Template for Calcium Phosphates Crystallization. *Crystal Growth and Design,* 9 (11): 4912–21.

Iafisco, M., Morales, J. G., Hernández-Hernández, M. A., García-Ruiz, J. M., & Roveri, N. (2010). Biomimetic Carbonate–Hydroxyapatite Nanocrystals Prepared by Vapor Diffusion. *Advanced Engineering Materials,* 12 (7): B218–23.

Ishikawa, K., Eanes, E. D., & Tung, M. S. (1994). The Effect of Supersaturation on Apatite Crystal Formation in Aqueous Solutions at Physiologic PH and Temperature. *Journal of dental research*, 73 (8): 1462–1469.

Johnsson, M. S. A., & Nancollas, G. H. (1992). The Role of Brushite and Octacalcium Phosphate in Apatite Formation. *Critical Reviews in Oral Biology & Medicine*, 3 (1): 61–82.

Kalikmanov, V. I. (2013). Classical Nucleation Theory, *In Nucleation theory*, 1st ed.; Springer Dordrecht; pp 17-41. DOI: 10.1007/978-90-481-3643-8

Kashchiev, D. (2000). Kinetics of Nucleation. In *Nucleation*, 1st ed.; Butterworth-Heinemann; pp 113- 285.

Kassebaum, N. J., Bernabé, E., Dahiya, M., Bhandari, B., Murray, C. J. L., & Marcenes, W. (2015). Global Burden of Untreated Caries: A Systematic Review and Metaregression. *Journal of Dental Research,* 94 (5): 650–58.

Kellermeier, M., Cölfen, H., & Gebauer, D. (2013). Investigating the Early Stages of Mineral Precipitation by Potentiometric Titration and Analytical Ultracentrifugation. *Methods in Enzymology,* 532 (January):45–69.

Khurshid, Z., Zafar, M., Qasim, S., Shahab, S., Naseem, M., & AbuReqaiba, A. (2015). Advances in Nanotechnology for Restorative Dentistry. *Materials,* 8 (2): 717–31.

Kim, H. M., Kishimoto, K., Miyaji, F., Kokubo, T., Yao, T., Suetsugu, Y., Tanaka, J., & Nakamura, T. (2000). Composition and Structure of Apatite Formed on Organic Polymer in Simulated Body Fluid with a High Content of Carbonate Ion. *Journal of Materials Science: Materials in Medicine,* 11 (7): 421–26.

Kim, J. W., Simmer, J. P., Lin, B. P. L., Seymen, F., Bartlett, J. D., & Hu, J. C. C. (2006). Mutational Analysis of Candidate Genes in 24 Amelogenesis Imperfecta Families. *European Journal of Oral Sciences,* 114 (SUPPL. 1): 3–12.

Kinney, J. H., Marshall, S. J., & Marshall, G. W. (2003). The Mechanical Properties of Human Dentin: A Critical Review and Re-Evaluation of the Dental Literature. *Critical Reviews in Oral Biology and Medicine,* 14 (1): 13–29.

Kleinberg, I. (2002). A Mixed-Bacteria Ecological Approach to Understanding the Role of the Oral Bacteria in Dental Caries Causation: An Alternative to Streptococcus Mutants and the Specific-Plaque Hypothesis. *Critical Reviews in Oral Biology & Medicine*, 13 (2): 108–25.

Kodaka, T., Kobori, M., Hirayama, A., & Abe, M. (1999). Abrasion of Human Enamel by Brushing with a Commercial Dentifrice Containing Hydroxyapatite Crystals in Vitro. *Journal of Electron Microscopy,* 48 (2): 167–72.

Kokubo, T., Kim, H. M., Kawashita, M., & Nakamura, T. (2001). Process of Calcification on Artificial Materials. *Zeitschrift Fur Kardiologie,* 90 (SUPPL. 3): 86–91.

Kokubo, T., Kushitani, H., Sakka, S., Kitsugi, T., & Yamamuro, T. (1990). Solutions Able to Reproduce in Vivo Surface-Structure Changes in Bioactive Glass-Ceramic A-W3. *Journal of Biomedical Materials Research,* 24 (6): 721–34.

Larsen, M. J., & Nyvad, B. (1999). Enamel Erosion by Some Soft Drinks and Orange Juices Relative to Their PH, Buffering Effect and Contents of Calcium Phosphate. *Caries Research,* 33 (1): 81–87.

Layrolle, P., Van der Valk, C., Dalmeijer, R., van Blitterswijk, C. A., & De Groot, K. (2001). Biomimetic Calcium Phosphate Coatings and Their Biological Performances. *Key Engineering Materials,* 192(195):391–94.

Layrolle, P., & Lebugle, A. (1996). Characterization and Reactivity of Nanosized Calcium Phosphates Prepared in Anhydrous Ethanol. *Chem. Mater, 6*(11): 1996-2004.

León, B. & Jansen, J.A. (2009). Pulsed Laser Deposition of Thin Calcium Phosphate Coatings. In *Thin Calcium Phosphate Coatings for Medical Implants*, 1st ed.; Springer New York, NY; pp 101-174. DOI: 10.1007/978-0-387-77718-4

Li, D., Nielsen, M. H., Lee, J. R., Frandsen, C., Banfield, J. F., & De Yoreo, J. J. (2012). Direction-Specific Interactions Control Crystal Growth by Oriented Attachment. *Science,* 336 (6084): 1014–1018.

Li, X., Chang, W. C., Chao, Y. J., Wang, R., & Chang, M. (2004). Nanoscale Structural and Mechanical Characterization of a Natural Nanocomposite Material: The Shell of Red Abalone. *Nano Letters,* 4 (4): 613–17.

Limeback, H., Enax, J., & Meyer, F. (2021). Biomimetic Hydroxyapatite and Caries Prevention: A Systematic Review and Meta-Analysis. *Canadian Journal of Dental Hygiene,* 55 (3): 148-159.

Liu, J., Li, K., Wang, H., Zhu, M., Xu, H., & Yan, H. (2004). Self-Assembly of Hydroxyapatite Nanostructures by Microwave Irradiation. *Nanotechnology,* 16 (1): 82-87.

Loke, C., Lee, J., Sander, S., Mei, L., & Farella, M. (2016). Factors Affecting Intra-Oral PH – a Review. *Journal of Oral Rehabilitation,* 43 (10): 778–85.

MacDougall, M. J., & Javed, A. (2010). *Dentin and Bone: Similar Collagenous Mineralized Tissues*, 6th ed.; Springer, London. DOI: 10.1007/978-1-84882-822-3_11

Mann S. (2001). General Principles of Biomineralization. In *Biomineralization: Principles and Concepts in Bioinorganic Materials Chemistry*, 5th ed.; Oxford Chemistry Masters, Oxford University Press; pp 24-37

Mao, Y., Park, T. J., Zhang, F., Zhou, H., & Wong, S. S. (2007). Environmentally Friendly Methodologies of Nanostructure Synthesis. *Small,* 3 (7): 1122–1139.

Mathur, V. P., & Dhillon, J. K. (2018). Dental Caries: A Disease Which Needs Attention. *Indian Journal of Pediatrics,* 85 (3): 202–206.

McKee, M. D., Addison, W. N., & Kaartinen, M. T. (2006). Hierarchies of Extracellular Matrix and Mineral Organization in Bone of the Craniofacial Complex and Skeleton. *Cells Tissues Organs,* 181 (3–4): 176–188.

McPherson, A. (1995). Increasing the Size of Microcrystals by Fine Sampling of pH Limits. *Journal of Applied Crystallography,* 28 (3): 362–365.

McPherson, A., & Cudney, B. (2014). Optimization of Crystallization Conditions for Biological Macromolecules. *Acta Crystallographic a Section F: Structural Biology Communications*, 70 (11): 1445–67.

Mekmene, O., Quillard, S., Rouillon, T., Bouler, J. M., Piot, M., & Gaucheron, F. (2009). Effects of PH and Ca/P Molar Ratio on the Quantity and Crystalline Structure of Calcium Phosphates Obtained from Aqueous Solutions. *Dairy Science and Technology,* 89 (3–4): 301–316.

Melo, M. A., Guedes, S. F., Xu, H. H., & Rodrigues, L. K. (2013). Nanotechnology-Based Restorative Materials for Dental Caries Management. *Trends in Biotechnology,* 31 (8): 459–67.

Meyer, F., Amaechi, B. T., Fabritius, H. O., & Enax, J. (2018). Overview of Calcium Phosphates Used in Biomimetic Oral Care. *The Open Dentistry Journal,* 12 (1): 406-423.

Mira, A., Simon-Soro, A., & Curtis, M. A. (2017). Role of Microbial Communities in the Pathogenesis of Periodontal Diseases and Caries. *Journal of Clinical Periodontology,* 44 (March): S23–38.

Mirabello, G., Ianiro, A., Bomans, P. H., Yoda, T., Arakaki, A., Friedrich, H., With, G., & Sommerdijk, N. A. (2019). Crystallization by Particle Attachment Is a Colloidal Assembly Process. *Nature Materials,* 19 (4): 391–96.

Miyazaki, T., Kim, H. M., Kokubo, T., Miyaji, F., Kato, H., & Nakamura, T. (2001). Effect of Thermal Treatment on Apatite-Forming Ability of NaOH-Treated Tantalum Metal. *Journal of Materials Science: Materials in Medicine,* 12 (8): 683–87.

Nancollas, G. H. (1984). The Nucleation and Growth of Phosphate Minerals. *In Phosphate Minerals*, 1st ed.; Springer Berlin, Heidelberg; pp 137-154. DOI: 10.1007/978-3-642-61736-2

Navrotsky, A. (2003). Energetics of Nanoparticle Oxides: Interplay between Surface Energy and Polymorphism†. *Geochemical Transactions,* 4 (1): 34-37.

Oxtoby, D. W. (1998). Homogeneous Nucleation: Theory and Experiment. *Journal of Physics: Condensed Matter*, *10*(4), 897-897.

Oyane, A., Kim, H. M., Furuya, T., Kokubo, T., Miyazaki, T., & Nakamura, T. (2003). Preparation and Assessment of Revised Simulated Body Fluids. *Journal of Biomedical Materials Research Part A: An Official Journal of The Society for Biomaterials, The Japanese Society for Biomaterials, and The Australian Society for Biomaterials and the Korean Society for Biomaterials,* 65 (2): 188–195.

Paris, S., & Meyer-Lueckel, H. (2009). Masking of Labial Enamel White Spot Lesions by Resin Infiltration--A Clinical Report. *Quintessence international*, 40(9): 713-718.

Parmley, S. F., & Smith, G. P. (1988). Antibody-Selectable Filamentous Fd Phage Vectors: Affinity Purification of Target Genes. *Gene,* 73 (2): 305–318.

Phillips, M. J., Darr, J. A., Luklinska, Z. B., & Rehman, I. (2003). Synthesis and Characterization of Nano-Biomaterials with Potential Osteological Applications. *Journal of Materials Science: Materials in Medicine,* 14 (10): 875–882.

Rao, A., Berg, J. K., Kellermeier, M., & Gebauer, D. (2014). Sweet on Biomineralization: Effects of Carbohydrates on the Early Stages of Calcium Carbonate Crystallization. *Article in European Journal of Mineralogy*, *26*(4), 537-552

Rapaport, H., Kuzmenko, I., Berfeld, M., Kjaer, K., Als-Nielsen, J., Popovitz-Biro, R., Weissbuch, I., Lahav, M., & Leiserowitz, L. (2000). From Nucleation to Engineering of Crystalline Architectures at Air-Liquid Interfaces. *Journal of Physical Chemistry B,* 104 (7): 1399–1428.

Raynaud, S., Champion, E., Bernache-Assollant, D., & Thomas, P. (2002). Calcium Phosphate Apatites with Variable Ca/P Atomic Ratio I. Synthesis, Characterisation and Thermal Stability of Powders. *Biomaterials,* 23 (4): 1065–1072.

Rehman, I., & Bonfield, W. J. J. (1997). Characterization of Hydroxyapatite and Carbonated Apatite by Photo Acoustic FTIR Spectroscopy. *Journal of Materials Science: Materials in Medicine,* 8 (1): 1–4.

Reynolds, E. C. (1998). Anticarcinogenic Complexes of Amorphous Calcium Phosphate Stabilized by Casein Phosphopeptides: A Review. *Special Care in Dentistry,* 18 (1): 8–16.

Robinson, C., Kirkham, J., & Shore, R. C. (2017). Structure of Developing Enamel, *In Dental Enamel Formation to Destruction,* 1st ed.; CRC Press Revivals; pp

Roveri, N., & Iafisco, M. (2010). Evolving Application of Biomimetic Nanostructured Hydroxyapatite. *Nanotechnology, Science and Applications,* 3 (1): 107–125.

Santos, C. L. Z. B., Luklinska, Z. B., Clarke, R. L., & Davy, K. W. M. (2001). Hydroxyapatite as a Filler for Dental Composite Materials: Mechanical Properties and in Vitro Bioactivity of Composites. *Journal of Materials Science: Materials in Medicine,* 12 (7): 565–573.

Sato, K., Kogure, T., Kumagai, Y., & Tanaka, J. (2001). Crystal Orientation of Hydroxyapatite Induced by Ordered Carboxyl Groups. *Journal of Colloid and Interface Science,* 240 (1): 133–138.

Schmidt, H. K. (2000). Nanoparticles for Ceramic and Nanocomposite Processing. *Molecular Crystals and Liquid Crystals Science and Technology. Section A. Molecular Crystals and Liquid Crystals,* 353 (1): 165–179.

Scott, J. K., & Smith, G. P. (1990). Searching for Peptide Ligands with an Epitope Library. *Science,* 249 (4967): 386–390.

Sharma, V., Srinivasan, A., Nikolajeff, F., & Kumar, S. (2021). Biomineralization Process in Hard Tissues: The Interaction Complexity within Protein and Inorganic Counterparts. *Acta Biomaterialia,* 120 (January):20–37.

Sharma, V., Srinivasan, A., Roychoudhury, A., Rani, K., Tyagi, M., Dev, K., Nikolajeff, F., & Kumar, S. (2019). Characterization of Protein Extracts from Different Types of Human Teeth and Insight in Biomineralization. *Scientific Reports,* 9(1): 1–9.

Shlaferman, J., Paige, A., Meserve, K., Miech, J. A., & Gerdon, A. E. (2019). Selected DNA Aptamers Influence Kinetics and Morphology in Calcium Phosphate Mineralization. *ACS Biomaterials Science and Engineering,* 5 (7): 3228–3236.

Sidhu, S. S. (2000). Phage Display in Pharmaceutical Biotechnology. *Current Opinion in Biotechnology,* 11 (6): 610–616.

Simmer, J. P., & Fincham, A. G. (1995). Molecular Mechanisms of Dental Enamel Formation. *Critical Reviews in Oral Biology & Medicine*, 6(2): 84–108.

Sloan, A. J. (2015). Biology of the Dentin-Pulp Complex. *Stem Cell Biology and Tissue Engineering in Dental Sciences*, (January): 371–78.

Slots, J., & Slots, H. (2011). Bacterial and Viral Pathogens in Saliva: Disease Relationship and Infectious Risk. *Periodontology 2000,* 55 (1): 48-69.

Smith, A. J. (2003). Vitality of the Dentin-Pulp Complex in Health and Disease: Growth Factors as Key Mediators. *Journal of Dental Education,* 67 (6): 678–89.

Smith, W. R., Hudson, P. W., Ponce, B. A., & Rajaram Manoharan, S. R. (2018). Nanotechnology in Orthopedics: A Clinically Oriented Review. *BMC Musculoskeletal Disorders,* 19 (1): 1–10.

Söderling, E. M. (2009). Xylitol, Mutans Streptococci, and Dental Plaque. *Advances in Dental Research,* 21(1): 74–78.

Söhnel, O., & Mullin, J. W. (1988). Interpretation of Crystallization Induction Periods. *Journal of Colloid and Interface Science,* 123 (1): 43–50.

Spanos, N., Misirlis, D. Y., Kanellopoulou, D. G., & Koutsoukos, P. G. (2006). Seeded Growth of Hydroxyapatite in Simulated Body Fluid. *Journal of Materials Science,* 41 (6): 1805–1812.

Studart, A. R., Erb, R. M., & Libanori, R. (2015). Bioinspired Hierarchical Composites. *Hybrid and Hierarchical Composite Materials*, January, 287–318.

Sun, W., Chu, C., Wang, J., & Zhao, H. (2007). Comparison of Periodontal Ligament Cells Responses to Dense and Nanophase Hydroxyapatite. *Journal of Materials Science: Materials in Medicine,* 18(5): 677–683.

Tamerler, C., & Sarikaya, M. (2008). Molecular Biomimetics: Genetic Synthesis, Assembly, and Formation of Materials Using Peptides. *MRS Bulletin,* 33(5): 504–512.

Tas, A. C., & Bhaduri, S. B. (2004). Chemical Processing of CaHPO4·2H2O: *Journal of the American Ceramic Society,* 87(12): 2195–2200.

Tas, A. C. (2000). Synthesis of Biomimetic Ca-Hydroxyapatite Powders at 37°C in Synthetic Body Fluids. *Biomaterials,* 21 (14): 1429–1438.

Thunsiri, K., Pitjamit, S., Pothacharoen, P., Pruksakorn, D., Nakkiew, W., & Wattanutchariya, W. (2020). The 3D-Printed Bilayer's Bioactive-Biomaterials Scaffold for Full-Thickness Articular Cartilage Defects Treatment. *Materials,* 13 (15): 3417.

Unosson, J. (2014). Physical Properties of Acidic Calcium Phosphate Cements. Ph.D Dissertation, Digital Comprehensive Summaries of Uppsala Dissertations from the Faculty of Science and Technology 1195. https://www.diva-portal.org/smash/record.jsf?pid=diva2:756900 (accessed 2024-06-11)

Vehkamäki, H. (2006). Nucleation Kinetics, In *Classical Nucleation Theory in Multicomponent Systems*, 1st ed.; Springer Science & Business Media; pp 85-110.

Vekilov, P. G. (2010). The Two-Step Mechanism of Nucleation of Crystals in Solution. *Nanoscale,* 2(11): 2346–357.

Vollenweider, M., Brunner, T. J., Knecht, S., Grass, R. N., Zehnder, M., Imfeld, T., & Stark, W. J. (2007). Remineralization of Human Dentin Using Ultrafine Bioactive Glass Particles. *Acta Biomaterialia,* 3(6): 936–43.

Wallace, A. F., Hedges, L. O., Fernandez-Martinez, A., Raiteri, P., Gale, J. D., Waychunas, G. A., ... & De Yoreo, J. J. (2013). Microscopic Evidence for Liquid-Liquid Separation in Supersaturated CaCO3 Solutions. *Science,* 341(6148): 885–889.

Walsh, L. J. (2009). Contemporary Technologies for Remineralization Therapies: A Review. *International Dentistry SA,* 11(6): 6–16.

Wang, J., & Shaw, L. L. (2007). Morphology-Enhanced Low-Temperature Sintering of Nanocrystalline Hydroxyapatite. *Advanced Materials,* 19(17): 2364–2369.

Wang, L., & Nancollas, G. H. (2008). Calcium Orthophosphates: Crystallization and Dissolution. *Chemical Reviews,* 108(11): 4628–4669.

Wang, Y., Li, L., Liang, H., Xing, Y., Yan, L., Dai, P., Gu, X., Zhao, G., & Zhao, X. (2019). Superstructure of a Metal-Organic Framework Derived from Microdroplet Flow Reaction: An Intermediate State of Crystallization by Particle Attachment. *ACS Nano,* 13(3): 2901–2912.

Weiner, S., & Bar-Yosef, O. (1990). States of Preservation of Bones from Prehistoric Sites in the Near East: A Survey. *Journal of Archaeological Science,* 17(2): 187–96.

Weiner, S., & Lowenstam, H. A. (1986). Organization of Extracellularly Mineralized Tissues: A Comparative Study of Biological Crystal Growth. *Critical Reviews in Biochemistry and Molecular Biology,* 20(4): 365–408.

Wright, J. T. (2006). The Molecular Etiologies and Associated Phenotypes of Amelogenesis Imperfecta. *American Journal of Medical Genetics Part A,* 140(23): 2547–2555.

Wu, D. T. (1996). Nucleation Theory. *In Solid State Physics - Advances in Research and Applications,* 50(C): 37–187.

Xu, J., Butler, I. S., & Gilson, D. F. (1999). FT-Raman and High-Pressure Infrared Spectroscopic Studies of Dicalcium Phosphate Dihydrate (CaHPO4·2H2O) and Anhydrous Dicalcium Phosphate (CaHPO4). *Spectrochimica Acta Part A: Molecular and Biomolecular Spectroscopy,* 55(14): 2801–2809.

Yeong, K. C. B., Wang, J., & Ng, S. C. (2001). Mechanochemical Synthesis of Nanocrystalline Hydroxyapatite from CaO and CaHPO4. *Biomaterials,* 22(20): 2705–12.

Young A. M., Neel A. A. E, & Chrzanowski W. (2014). Interfaces in Composite Materials. In *Biointerfaces: Where Material Meets Biology,* 1st ed.; Royal Society of Chemistry; pp 153-173. DOI: 10.1039/9781782628453-00151

Zhang, Y., & Lu, J. (2007). A Simple Method to Tailor Spherical Nanocrystal Hydroxyapatite at Low Temperature. *Journal of Nanoparticle Research,* 9(4): 589–94.

Zhu, J., Shu, J., Yue, X., & Su, Y. (2020). Hollow and Porous Octacalcium Phosphate Superstructures Mediated by the Polyelectrolyte PSS: A Superior Removal Capacity for Heavy Metal and Antibiotics. *Journal of Materials Science,* 55(17): 7502–7517.

APPENDIX A

KINETIC MEASUREMENT

The first set of results were obtained from mineralization kinetics experiments. Ca^{2+} and PO_4^{3-} solutions prepared in HEPES buffers with pH values of 6.6, 6.8, 7.0, 7.2, 7.4, 7.6, and 7.8 at 25°C were treated with each other in the ratio of 4.8/2.88 mM. Figure A.1 shows the absorbance values of these samples after 1 hour of mineralization kinetics. According to this result, it was concluded that Ca^{2+}/ PO_4^{3-} precipitates were formed in solutions with pH values of 7.2, 7.4, 7.6, and 7.8, but Ca^{2+}/ PO_4^{3-} precipitates were not formed in solutions with pH values of 6.6, 6.8, and 7.0.

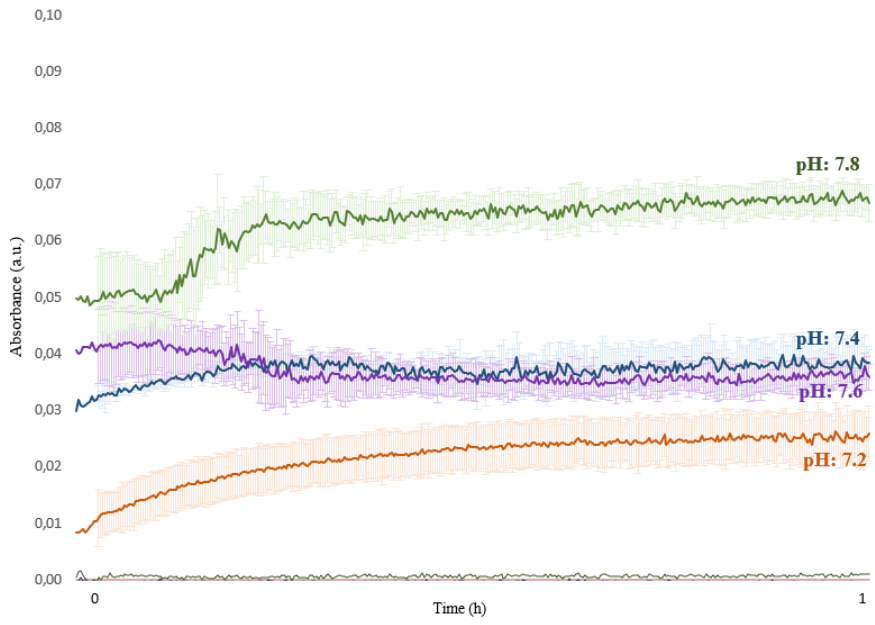

Figure A.1. Ca^{2+}/ $P0_4^{3-}$ nucleation kinetics spectra at different pH values and in HEPES buffer at 25 °C when Ca^{2+}/ $P0_4^{3-}$: 4.8/2.88 mM

These solutions were heated to 37°C and the pH values in all these solutions decreased by 0.13(+_ 0.01) on average. Figure A.2 shows the absorbance values of these samples

heated to 37°C after 1 hour of mineralization kinetics. According to this result, it was concluded that Ca^{2+}/PO_4^{3-}precipitates were formed in solutions with pH values of 7.2, 7.4, 7.6, and 7.8, but Ca^{2+}/PO_4^{3-} precipitates were not formed in solutions with pH values of 6.6, 6.8, and 7.0.

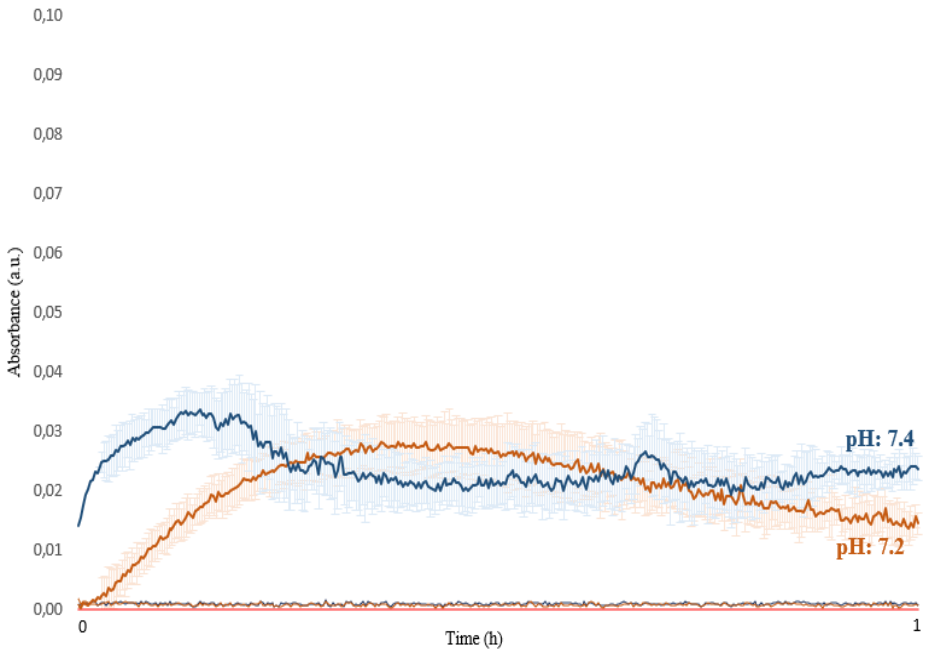

Figure A.2. $Ca^{2+}/ P0_4^{3-}$ nucleation kinetics spectra at different pH values and in HEPES buffer at 37 °C when $Ca^{2+}/ P0_4^{3-}$: 4.8/2.88 Mm

These solutions were heated to 37°C. Figure A.6 shows the absorbance values of these samples heated to 37°C as a result of 1-hour mineralization kinetics. Figure A.2 shows the absorbance values of these samples after 1 hour of mineralization kinetics. According to this result, it was concluded that Ca^{2+}/ PO_4^{3-} precipitates were not formed at any pH value.

When Figure A.1. and Figure A.2. are analyzed within themselves, it is observed that the absorbance values of Ca^{2+}/ PO_4^{3-} precipitates increase continuously as the pH values increase. This leads to the conclusion that pH increase has a positive effect on Ca^{2+}/ PO_4^{3-} mineralization.

These test sets were also tested in tris buffers, Ca^{2+} and $P0_4^{3-}$ solutions prepared in tris buffers with pH values of 6.6, 6.8, 7.0, 7.2, 7.4, 7.6, and 7.8 at 25°C were treated with each other at a ratio of 4.8/2.88 Mm. Figure A.3. shows the absorbance values of these samples after 1 hour of mineralization kinetics. According to this result, it was concluded that Ca^{2+}/ $P0_4^{3-}$ precipitates were formed in solutions with pH values of 7.2, 7.4, 7.6, and 7.8, but Ca^{2+}/ $P0_4^{3-}$ precipitates were not formed in solutions with Ph values of 6.6, 6.8, and 7.0.

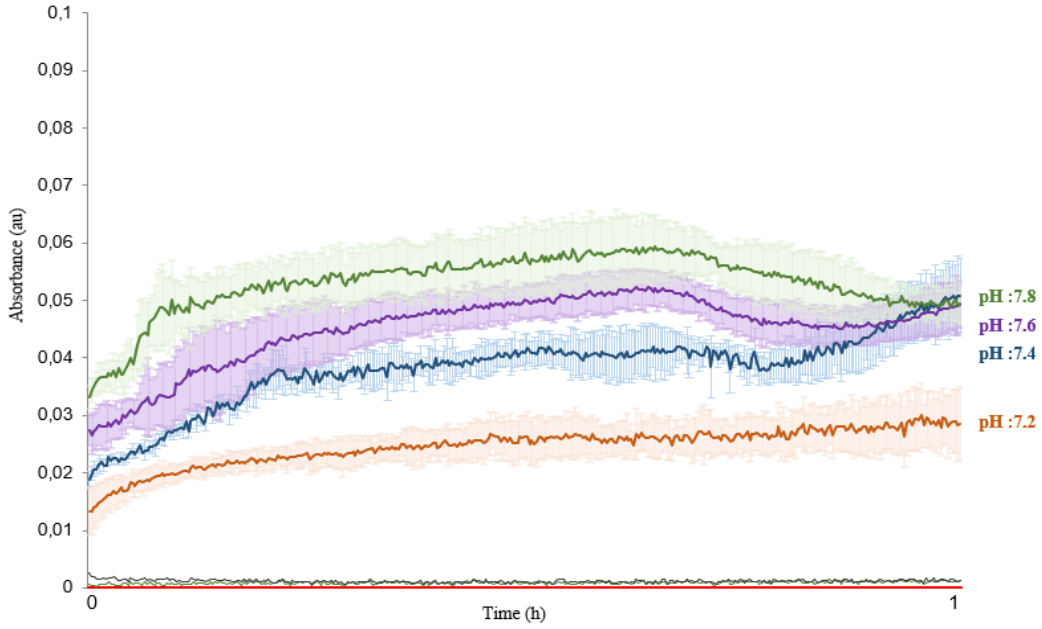

Figure A.3. Ca^{2+}/ $P0_4^{3-}$ nucleation kinetics spectra at different pH values and in Tris buffer at 25°C when Ca^{2+}/ $P0_4^{3-}$: 4.8/2.88 mM

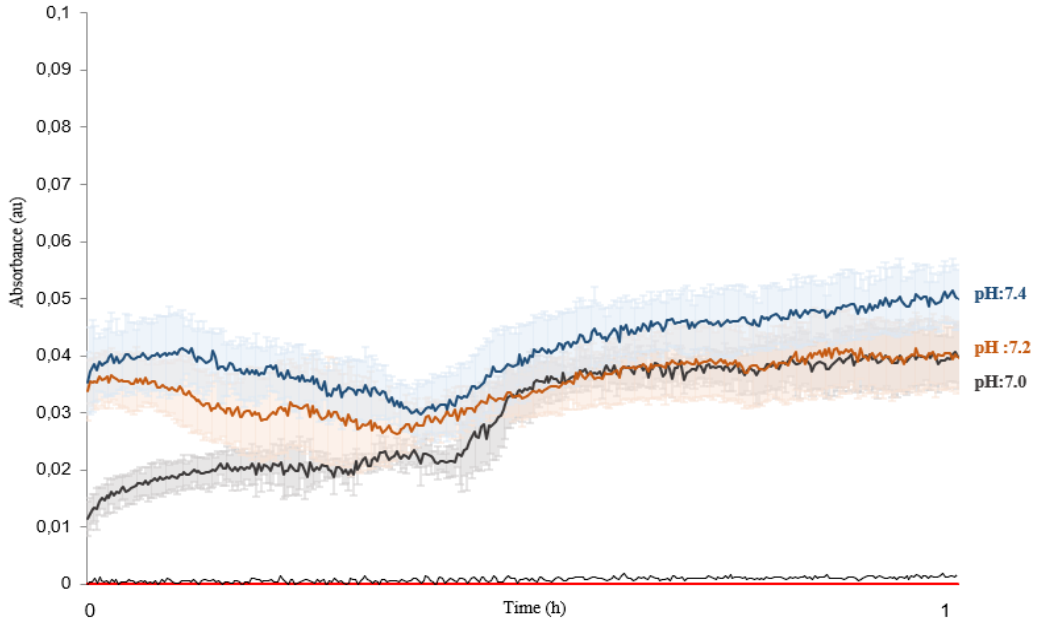

Figure A.4. Ca^{2+}/ $P0_4^{3-}$ nucleation kinetics spectra at different pH values and in Tris buffer at 37°C when Ca^{2+}/ $P0_4^{3-}$: 4.8/2.88 Mm

These solutions were heated to 37°C and the pH values in all these solutions decreased by 0.32(+_ 0.01) on average. Since this value is quite high in terms of pH change, these solutions were prepared again at 37°C with pH adjustments and these solutions were used for the experiments to be performed at 37°C. Figure A.4 shows the absorbance values of these samples prepared at 37°C as a result of 1-hour mineralization kinetics. According to this result, it was concluded that Ca^{2+}/ $P0_4^{3-}$ precipitates were formed in solutions with pH values of 7.0, 7.2, and 7.4, but Ca^{2+}/ $P0_4^{3-}$ precipitates were not formed in solutions with pH values of 6.6, and 6.8.